8-2019

Microfluidic particle separation via elasto-inertial focusing in straight rectangular microchannels

Di Li
Clemson University, owllight9226@gmail.com

Recommended Citation
Li, Di, "Microfluidic particle separation via elasto-inertial focusing in straight rectangular microchannels" (2019). *All Dissertations*. 2427.
https://tigerprints.clemson.edu/all_dissertations/2427

MICROFLUIDIC PARTICLE SEPARATION VIA ELASTO-INERTIAL FOCUSING IN STRAIGHT RECTANGULAR MICROCHANNELS

A Dissertation
Presented to
the Graduate School of
Clemson University

In Partial Fulfillment
of the Requirements for the Degree
Doctor of Philosophy
Mechanical Engineering

---

by
Di Li
August 2019

Accepted by:
Dr. Xiangchun Xuan, Committee Chair
Dr. Chenning Tong
Dr. Richard Miller
Dr. Phanindra Tallapragada

ABSTRACT

Label-free separation of target particles or cells in a continuous flow is a crucial process in many commercial and industrial applications. Among the various particle and cell separation techniques, microfluidic separator based on elasto-inertial forces in the flow of non-Newtonian fluids has received increasing attention in the past decade. However, current studies have been mainly focused upon the use of viscoelastic forces to manipulate particles and cells. Little work has been done to obtain a fundamental understanding on how the fluid rheological properties, such as viscoelasticity and shear thinning, affect the motion of particles. This dissertation is aimed to address this question through a systematic experimental study.

We first designed a series of experiments to study both the individual and combined effects of fluid rheology and inertia on the migration of rigid spherical particles in a (nearly) square microchannel. The sole effects of fluid inertia, elasticity and shear thinning were investigated by re-suspending the same particles into Newtonian (water), purely elastic (polyvinylpyrrolidone, PVP) and inelastic shear thinning (xanthan gum, XG) fluids, respectively. The combined effects of fluid elasticity and inertia or fluid shear thinning and inertia were investigated in the flow of PVP and XG solutions over a wide range of flow rates. The combined effects of fluid elasticity, shear thinning, and inertia were investigated in two types of elastic fluids with varying shear-thinning properties (polyethylene oxide, PEO and polyacrylamide, PAA). We found that fluid elasticity directs particles toward the channel centerline while fluid shear thinning causes particles to migrate towards both the centerline and corners.

In the second part of this dissertation, we performed a comprehensive study of the separation of particles and cells in the flow of PEO solutions through straight rectangular microchannels. We investigated the effects of flow rate, solvent viscosity, PEO concentration, and channel height on the elasto-inertial separation of spherical polystyrene particles. We proposed to explain the observed elasto-inertial particle focusing using a competition of center- (because of fluid elasticity) and wall- (because of fluid shear thinning) directed viscoelastic forces. We also applied this sheath-free separation technique in the flow of biocompatible PEO solutions to sort drug-treated *Cryptococcus neoformans* by morphology. Three metrics were used to evaluate the parametric effects on the cell separation performance: efficiency, purity, and enrichment ratio.

In the last part of this dissertation, we performed another systematic experimental study of the motion of rigid spherical particles in the flow of inelastic shear-thinning XG solutions through straight rectangular microchannels. We found that the number and location of equilibrium particles position are both a strong function of channel dimension, particle size, and XG concentration. Inspired by this study, we demonstrated for the first time a continuous sheath-free separation of polystyrene particles in XG solutions through a straight high width/depth-ratio microchannel. This separation was found to remain effective over a much wider range of flow rates than those reported in the flow of viscoelastic fluids. We attempted to explain the particle migrations in XG solutions using the competition of a strong wall-directed (because of the strong shear thinning effect) and a weak center-directed (because of the weak elasticity effect) lateral force induced by normal stresses in a Poiseuille flow.

DEDICATION

To my loving mother Aizhen Huang.

ACKNOWLEDGMENTS

First, I would like to thank my advisor Dr. Xiangchun Xuan for investing in my professional growth and providing me with incredible teaching and research opportunities throughout my time at Clemson. I would like to express my sincere gratitude to him for his broad foresight, patient guidance, and unwavering support on my research which paved the way for my academic career.

I would also like to thank my committee members, Dr. Chenning Tong, Dr. Richard Miller, and Dr. Phanindra Tallapragada for giving up their precious time to be a part of my committee. I am gracious for the constant support and constructive advice I have received on their behalf during my graduate studies.

I would like to thank my colleagues Xinyu Lu, Yilong Zhou, Akshay Kale, Zhijian Liu, Qi Chen, Le Song, Amirreza Malekan Fard and Purva Jagdale for being supportive during the past years. I would like to thank my friends in Clemson for creating a cheerful atmosphere which made my years at the graduate school enjoyable. I would like to thank my father and mother for their love and support throughout my entire life. I am forever indebted to them and much of this work reflects the values they installed in me.

TABLE OF CONTENTS

Page

CHAPTER

Page

Table of Contents (Continued)

Page

LIST OF TABLES

Table Page

List of Tables (Continued)

LIST OF FIGURES

List of Figures (Continued)

Figure Page

List of Figures (Continued)

Figure Page

Figure Page

List of Figures (Continued)

Figure Page

Figure Page

List of Figures (Continued)

Figure Page

Figure Page

Figure Page

CHAPTER ONE

INTRODUCTION

1.1 Aim and motivation

Separating target particles or cells from a heterogeneous mixture based on extrinsic (e.g., fluorescent or magnetic labeling) or intrinsic (e.g., size or shape) properties in a continuous flow is crucial for many biological, chemical and environmental applications. Circulating tumor cells (CTCs), for instance, exist with low numbers (typically < 500 per 7.5 mL of blood) in blood samples taken from cancer patients. Once the rare CTCs are separated from the original sample, they can be individually used as a marker for both early-stage diagnosis of cancers and prediction of disease progression.[1] Continuous particle separation has been successfully implemented using a variety of approaches in microfluidic devices. Compared with the macroscopic counterparts, microfluidic devices offer higher efficiency, accuracy, and portability with less amount of samples and usually simpler operation.

In general, microfluidic particle and cell separator can be classified as two types: active and passive. The active separation method uses an externally imposed force field (e.g., acoustic, electric, magnetic or optical) to manipulate particles with high specificity.[2] However, this type of methods usually requires complicated peripheral equipment and has limited throughput. In contrast, the passive separation method makes use of the inherent flow-induced hydrodynamic forces for automatic particle manipulations. It has been demonstrated as a very promising technique in the past decade or so because of its simplicity and high throughput. In this direction, the inertial lift generated in the flow of Newtonian fluid has been widely studied to focus, separate and concentrate particles and cells at high Reynolds numbers (~1 < Re < ~100). However, inertial microfluidics has limitations in the control of small particles and/or at low flow rate (or more specifically, when the particle Reynolds number is much smaller than 1).[3] Recent studies have demonstrated the use of elastic lift to manipulate very small particles (down to the order of 100 nanometers) in the flow of non-Newtonian fluid over a wide range of Re.[30] While multiple fluids with varying rheological properties have been involved in these studies, an accurate and comprehensive understanding of the sole and combined effects of fluid rheology on particle migration is still lacking. The first aim of this dissertation is to tackle this question by the use of a systematic experimental study of the elasto-inertial particle migration in the flow of specially chosen non-Newtonian fluids through straight rectangular microchannels. The second aim of this dissertation is to conduct a comprehensive parametric study of the elasto-inertial focusing of particles in two non-Newtonian fluids that we think are promising for particle separation applications.

1.2 Background

There will be two forces acting on a rigid particle as it flowing through a straight rectangular microchannel: inertial and elastic force. The basic concepts about these two forces will be introduced in this section. We will also give a brief review about the most often used non-Newtonian fluids in microfluidic devices.

1.2.1 Flow-induced forces

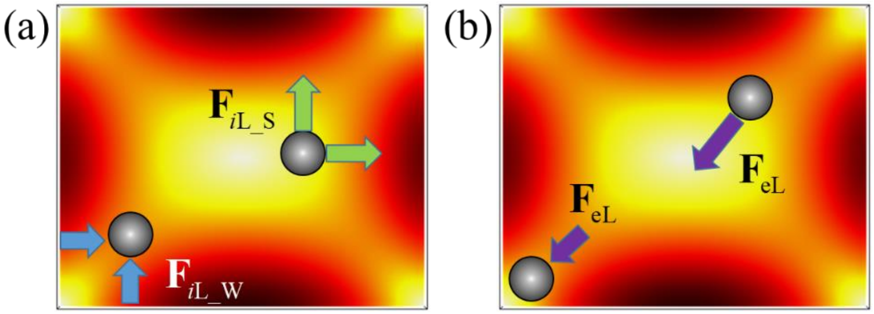

Fig. 1.1. Schematic illustration of (a) inertial force ($\mathbf{F}_{\text{iL}}$) and (b) elastic force ($\mathbf{F}_{\text{eL}}$) acting on the particle in a straight rectangular channel. The background is the shear rate distribution (the darker the larger magnitude).

The particle radial migration in the Newtonian fluid within a macroscopic tube (diameter 11.6 mm) had been observed first by Segre and Silberberg [4] over 50 years ago. Since the whole experiments implemented in the laminar flow region, people realized that fluid inertia could induce a force to control particle in the radial direction. Due to the small scale of the microchannel, most of the time flow in microfluidic device falls in the laminar flow region. So inertial lift can use as a powerful tool to manipulate particle in microfluidic separator applying passive separation strategy. Previous studies [5] showed that the inertial lift ($\mathbf{F}_{\text{iL}}$) acting on a rigid particle could decompose into two components: the wall-induced lift ($\mathbf{F}_{\text{iL\_W}}$), and the shear gradient-induced lift ($\mathbf{F}_{\text{iL\_S}}$). Fig. 1.1. (a) demonstrates the direction of the two lift forces on a spherical particle in the rectangular cross-section of a straight channel. The wall-induced lift generates from the unbalanced pressure between the particle and adjacent wall and will push particles towards the channel center. The shear gradient-induced lift generates from the inhomogeneous velocity profile and will always push particle towards the channel wall due to the parabolic velocity profile in the rectangular channel.[6] The total inertial force scale as:

$$\mathbf{F}_{\mathrm{iL}} = \mathbf{F}_{\mathrm{iL\_W}} + \mathbf{F}_{\mathrm{iL\_S}} \sim \rho a^4 \dot{\gamma}^2 / D_h^2 \tag{1-1}$$

where ρ is the fluid density, $\dot{\gamma}$ is the shear rate, a is the particle radius and D_h is the hydraulic diameter of the microchannel. Typically, we use channel Reynolds number to judge the strength of the inertial lift within the channel:

$$\mathrm{Re} = \frac{\rho U D_h}{\mu(\bar{\dot{\gamma}})} \tag{1-2}$$

where U is the average velocity within the channel and $\mu(\bar{\dot{\gamma}})$ is the shear-dependent viscosity calculated at average shear rate $\bar{\dot{\gamma}}$.

Due to the elasticity existed in non-Newtonian fluid, the particle also experiences elastic lift ($\mathbf{F}_{\mathrm{eL}}$). This force generates from the non-uniform normal stress difference within the viscoelastic fluid. In a straight channel, τ_{11} is normal stress in translational direction while τ_{22} and τ_{33} are normal stress in the orthogonal directions with respect to τ_{11}. The first and second normal stress difference are then defined as $N_1 = \tau_{11} - \tau_{22}$ and $N_2 = \tau_{22} - \tau_{33}$. In general, the magnitude of N_1 is much larger than N_2 for most non-Newtonian fluids.[7] From the first normal stress measurement of polymer and polymer melt, N_1 demonstrates a power-law behavior over a range of shear rates, and N_1 can be expressed as:

$$N_1 = A\dot{\gamma}^m \tag{1-3}$$

in which A and m are fluid-dependent constants, with m in the range of $1 < m \le 2$.[8] Then the elastic lift can scale as:

$$\mathbf{F}_{\mathrm{eL}} \sim a^3 \nabla N_1 = a^3 A \nabla \dot{\gamma}^m \tag{1-4}$$

Hence, as depicted in Fig. 1.1. (b), the elastic lift directs particles towards low shear rate region, i.e., the center and four corners of a rectangular channel. The viscoelastic effect of fluid on particle motion can characterize by the Weissenberg number (Wi),

$$\mathrm{Wi} = \lambda \bar{\dot{\gamma}} \tag{1-5}$$

with λ being the relaxation time of the fluid.

From Eq. (1-1) and (1-4), it is evident that both inertial and elastic lift are proportional to the particle radius with different power index, the particle with dissimilar size will move to size-dependent equilibrium position and realize size based particle separation.

In a straight channel, fluid also introduces viscous drag force on the particle when it has relative speed with the surrounding fluid. Since the particle Reynolds number $\mathrm{Re}_p = \rho U_r a/\mu$ (U_r is the relative velocity of the fluid to particle) in all the cases discussed in this dissertation should be smaller than 1, the Stokes drag can be applied on both mainstream and lateral migration directions.[3]

1.2.2 Particle lateral motion in the non-Newtonian fluid

Due to the consideration of biocompatibility, chemical stability, storage condition, economy, etc., a very limited number of non-Newtonian fluid has been used in the microfluidic system for particle manipulation. Among them, the most often used one should be polyethylene oxide (PEO) solution. Dilute PEO solution (typically concentration lower than 1 wt.%) exhibits medium elasticity and very weak shear thinning. Early works mainly studied the ability of PEO to focus micro (~ 10 μm) and sub-micro (~1 μm) particles towards the center of the straight square[9-10] and cylindrical channel[15]. By introducing a high concentration of PEO solution, which will demonstrate shear-dependent viscosity, some groups investigated the shear thinning effect on the particle focusing.[13,16,23] If the cross-section of straight channel changes to rectangular, multiple particle focusing streams will form in the channel.[17,24,32] Apart from the straight channel, the curved channel which can generate Dean drag on the particle has also been used to focus particle in PEO solution. Few works made use of spiral[12,25-26], serpentine[36], straight channel with triangular sidewalls[17], and periodic wavy channel[37] to realize particle focusing.

Within the straight channel, PEO-aided particle separation is mostly implemented by pre-focusing particle mixture to the channel wall using sheath flow, and then the larger particle will displace further away from the adjacent wall due to the stronger elastic and/or inertial force. Since both the particle flow and sheath flow can be either PEO or Newtonian fluid, three cases can exist. Firstly, when both sample and sheath flow are PEO solution, the particle can migrate to size or shape dependent equilibrium positions.[11,14,19-20,30] Secondly, if the sheath flow is switching to Newtonian fluid, only the large particle can cross the interface while small particles remain in PEO solution.[34] Finally, the particle mixture suspends in a Newtonian fluid, and sheath flow becomes PEO.[28,31-32] This strategy is especially useful if the number of small particles is far more than large ones (i.e., CTCs in whole blood) as inertial force is unable to effectively control small particles and hence make sure small particle can stay in the Newtonian fluid. Very few works implement particle separation without the help of sheath flow. In a straight square channel, PEO can be used to focus large particle towards the channel center and leaving small particles dispersed.[9,22] In a straight rectangular channel[17,21], a straight channel with triangular sidewalls[27,33], spiral channel[12,26] and periodic wavy channel[37], as mentioned above, the particle can migrate to size-dependent focusing position within the channel hence realize size and shape based particle separation. Table 1.1 summarizes the particle manipulation in a microchannel using PEO solution.

Table 1.1. Particle manipulation in PEO solution.

Reference	Solvent concentration	manipulation[a]	Channel structure	Channel dimension	Particle size (*d* in μm)	Year
Yang et al.[9]	500 ppm	focusing	straight square	50 × 50 μm^2	PS (5.9)	2011
	250 ppm	separation (N)	straight square	50 × 50 μm^2	PS (5.9/2.4)	
Kim et al.[10]	500 ppm	focusing	straight square	5 × 5 μm^2	PS (0.1/0.2/ 1/0.5/2.4)	2012
Nam et al.[11]	500 ppm	separation (Y)	straight rectangular	50 × 50 μm^2	PS (1/5), Blood	2012
Lee et al.[12]	500 ~ 5000 ppm	focusing	spiral rectangular	100 × 25 μm^2	PS (1.5/5/10)	2013
	500 ~ 5000 ppm	separation (N)	spiral rectangular	100 × 25 μm^2	PS (1.5/10)	
Seo et al.[13]	1 wt%	focusing	straight square	300 × 300 μm^2	PS (30/50)	2014
Lim et al.[14]	500 ppm	separation (Y)	straight rectangular	100 × 50 μm^2	PS (1/10)	2014
Santo et al.[15]	3000 ppm	focusing	straight cylindrical	Φ = 5 μm	PS (0.2)	2014
Del Giudice et al.[16]	0.1/0.8/ 1.6 wt%	focusing	straight square	100 × 100 μm^2	PS (10)	2015
Liu et al.[17]	2000 ppm	focusing	straight rectangular	200 × 50 μm^2 100 × 50 μm^2 50 × 50 μm^2	PS (5/15)	2015

	2000 ppm	separation (N)	straight rectangular	100 × 50 μm^2	PS (5/15) RCB/ MCF-7	
Yuan et al.[18]	500 ppm	focusing	triangular side wall	100 × 40 μm^2	PS (3.2/4.8/13)	2015
Lu et al.[19]	500 ~ 2000 ppm	separation (Y)	straight rectangular	50 × 25 μm^2 50 × 40 μm^2 50 × 100 μm^2	PS (3/10)	2015
Lu et al.[20]	1000 ppm	separation (Y)	straight rectangular	50 × 25 μm^2	PS (4.18, sphere/ peanut)	2015
Lu et al.[21]	1000 ppm	separation (N)	straight rectangular	50 × 25 μm^2	PS (4.18, sphere /peanut)	2015
Ahn et al.[22]	100 ~ 1000 ppm	separation (N)	straight square	50 × 50 μm^2	PS (4.5/2.3)	2015
Song et al.[23]	0.1 ~ 1 wt%	focusing	straight square	50 × 50 μm^2	PS (4.78)	2016
Xiang et al.[24]	500 ppm	focusing	straight rectangular	150 × 50 μm^2 100 × 50 μm^2 50 × 50 μm^2	PS (2/5/10)	2016
Xiang et al.[25]	500 ppm	focusing	spiral rectangular	215 × 50 μm^2 140 × 50 μm^2 90 × 50 μm^2	PS (5/10)	2016
Liu et al.[26]	0.2 ~ 2 % wt	focusing	spiral rectangular	30 × 4 μm^2	PS (0.049~2), λ-DNA	2016
	0.6 wt%	separation (N)	spiral rectangular	30 × 4 μm^2	PS (2/0.1), platelet/ λ-DNA	
Yuan et al.[27]	500 ~ 2000 ppm	separation (N)	triangular side wall	100 × 40 μm^2	PS (3/4.8/10), Blood	2016
Faridi et al.[28]	500 ppm	separation (Y)	straight rectangular	50 × 65 μm^2	PS (2/5), E. coli	2017
Holzner et al.[29]	500 ppm	focusing	straight square	53 × 53 μm^2	B-lymphoid, E. coli	2017
Liu et al.[30]	250 ~ 1500 ppm	separation (Y)	straight rectangular	20 × 50 μm^2	PS (0.1/0.5/1), Exosomes/ Extracellular Vesicles	2017
Tian et al.[31]	50 ~ 1200 ppm	separation (Y)	straight rectangular	20 × 50 μm^2	PS (1/2), platelets/ aureus	2017
Yang et al.[32]	500 - 4000 ppm	focusing	straight rectangular	100 × 25 μm^2 50 × 25 μm^2 25 × 25 μm^2	PS (6.42/10/15)	2017
Yuan et al.[33]	1000 ppm	separation (N)	triangular side wall	50 × 30 μm^2	PS (5/13), Jurkat/Yeast	2017

Yuan et al.[34]	1000 ppm	separation (Y)	straight rectangular	30 × 50 μm^2	PS (0.8~10), Jurkat	2017
Tian et al.[35]	50/150/500 ppm	separation (Y)	straight rectangular	100 × 50 μm^2	PS (5/10/15), CTCs	2018
Yuan et al.[36]	1000 ppm	focusing	serpentine rectangular	100 × 42 μm^2	PS (13), Jurkat	2019
Zhou et al.[37]	800 ~ 1600 ppm	focusing	wavy rectangular	40 × 10 μm^2	PS (0.1/0.3/0.5/1)	2019
	1600 ppm	separation (Y)	wavy rectangular	40 × 10 μm^2	PS (0.1/0.3), Exosomes/ Extracellular Vesicles	

[a]Note: separation (Y/N) denotes separating particle with or without sheath flow.

Polyvinylpyrrolidone (PVP) solution is also widely used for particle manipulation in the microchannel. PVP solution can keep a constant viscosity under a wide range of shear rate for polymer concentration as high as 8 wt.%. Its large viscosity suppresses the fluid inertia and hence exhibits a strong elasticity within the microchannel. As in the slit rectangular[38,44,47] and straight cylindrical channel[39,41,51], the corner effect can be neglected, the dominant elastic force in the PVP solution can push particles towards the channel mid-plane or channel center. In the straight square channel, PVP solution cannot focus particle into a single train as four channel corners are also low shear rate region.[9,42-43] Only one paper concerns PVP focusing in a straight rectangular channel.[24] But the formation of single particle stream should contribute to the large particle blockage ratio in their experiment. By adding square side wells[45] or using a spiral channel[49], extra drag can generate from the curved streamlines hence realize single train particle focusing. Very limited works make use of PVP to separate particles. With the help of sheath flow, particles with different size can be separated in PVP solution using a deterministic lateral displacement (DLD) device.[48] Without sheath flow, a bifurcating channel can be used as a microfluidic separator. The particle mixture will first align to the center of the cylindrical[46] or high aspect ratio rectangular[50] main-branch within the PVP solution. Then they can migrate away from the sidewall of the rectangular side-branch towards size sensitive equilibrium positions. In the simple straight rectangular channel, since the deformability of red blood cells (RBC) can introduce extra wall lift and push soft RBC away from the channel corner, making enrichment of rigid RBC or white blood cells (WBC) at the channel corner possible.[40] The summarized information about particle manipulation in the PVP solution is demonstrated in Table 1.2.

Table 1.2. Particle manipulation in PVP solution.

Reference	Solvent concentration	manipulation[a]	Channel structure	Channel dimension	Particle size (*d* in μm)	Year
Leshansky et al.[38]	8 wt.%	focusing	straight slit	1000 × 45 μm^2	PS (5/8)	2007
Yang et al.[9]	8 wt.%	focusing	straight square	50 × 50 μm^2	PS (5.9)	2011
D'Avino et al.[39]	8 wt.%	focusing	straight cylindrical	Φ = 300 μm	PS (4)	2012
Yang et al.[40]	6.8 wt.%	separation (N)	straight square	75 × 75 μm^2	PS (6), RBC, WBC	2012
Romeo et al.[41]	8 wt.%	focusing	straight cylindrical	Φ = 50 μm	PS (2.4/5.9)	2013
Del Giudice et al.[42]	8 wt.%	focusing	straight square	50 × 50 μm^2 100 × 100 μm^2	PS (5.8/10)	2013
Seo et al.[43]	8 wt.%	focusing	straight square	300 × 300 μm^2	PS (30/50)	2014
Seo et al.[44]	3 wt.% / 8 wt.%	focusing	straight slit	500 × 50 μm^2 300 × 30 μm^2	PS (7.22), RBC	2014
Cha et al.[45]	6.8 wt.%	focusing	square side wells	50 × 50 μm^2	PS (6)	2014
Nam et al.[46]	8 wt.%	separation (N)	straight cylindrical	Φ = 43 um 40 × 45 μm^2	PS (5/10)	2015

			+ Y shape rectangular			
Xiang et al.[24]	8 wt.%	focusing	straight rectangular	150 × 50 μm^2	PS (10)	2016
Go et al.[47]	3 wt.%	focusing	straight slit	500 × 50 μm^2	RBC	2017
Li et al.[48]	3000/8000 ppm	separation (Y)	straight rectangular with DLD	2000 × 40 μm^2	PS (7.1 ~ 18.9)	2018
Xiang et al.[49]	2.0/2.6/5.2/ 8.0 wt.%	focusing	spiral rectangular	140 × 50 μm^2	PS (10)	2018
Nam et al.[50]	6.8 wt.%	separation (N)	straight rectangular + Y shape rectangular	25 × 150 μm^2 50 × 150 um2	RBC/WBC	2019
Xiang et al.[51]	0.05/8.0 wt.%	focusing	straight cylindrical	Φ = 79/100/ 152 μm	PS (5/10)	2019

[a]Note: separation (Y/N) denotes separating particle with or without sheath flow.

Most biological fluids exhibit non-Newtonian property and a few of them has been used to manipulate particle within microfluidic devices. Hyaluronic acid (HA), which function as the synovial fluid within animal joints, has strong elasticity as well as shear thinning. In a bifurcating channel, it can replace PVP solution that can focus particle mixture in the main-branch (either cylindrical[53] or high aspect ratio rectangular[54]) and displace particle away from the sidewall in side-branch with a size-dependent rate. HA solution has also proven to be a powerful tool to focus particle into a single train in both straight square[52] and rectangular channel[55]. By utilizing 3D printing, channels with unconventional cross-section such as triangle and semi-elliptic have been manufactured and HA-based particle focusing position within those channels has also investigated.[57] Very recently, HA solution was found to be able to focus particle towards size-based equilibrium position within a straight rectangular channel, and a sheathless continuous separator had developed to separate candida cells from white blood cells.[56] There are also few works using dilute DNA solution to manipulate particles. The dilute DNA solution (typically lower than 100 ppm) contains very strong elasticity due to its extremely long relaxation time. Particle focusing in DNA solution has been implemented in both straight cylindrical[58] and rectangular channel[59]. Only sheath flow aided particle separation can be seen in the published works, in which the shear flow can be either DNA solution itself[58] or a Newtonian fluid[60]. The aqueous solution of xanthan gum (XG), an extracellular polysaccharide, has found to possess very weak elasticity and strong shear thinning. Through varying the strength of shear thinning (i.e., changing the XG concentration), it can dynamically control the critical separation size for a DLD array with fixed geometry.[48] Another extracellular polymeric substance (EPSs) secrets by *Chlorella vulgaris*, which are mainly composed of polysaccharide, proteins, and DNA. It was found to have mild elasticity as well as shear-thinning effect and was used to focus particle in both straight rectangular and spiral channel.[61] As mentioned in the previous section, the whole blood can be treated as a non-Newtonian fluid. So by pinching a particle-free saline core flow into the whole blood and particle (or large cells) mixture, the particle can migrate across the interface and separate from the blood.[62] Table 1.3. summarizes the particle manipulation in biological fluids.

Table 1.3. Particle manipulation in biological fluids.

Reference	Solvent concentration	manipulation[a]	Channel structure	Channel dimension	Particle size (*d* in μm)	Year
Hyaluronic acid (HA)						
Lim et al.[52]	0.1 wt.%	focusing	straight square	$80 \times 80\ \mu m^2$	PS (1-8)	2013

Nam et al.[53]	0.1 wt.%	separation (N)	straight cylindrical + Y shape rectangular	Φ = 50 µm 70 × 200 µm^2	MCF-7 /WBC	2015
Nam et al.[54]	0.1 wt.%	separation (N)	straight rectangular + Y shape rectangular	25 × 250 µm^2 70 × 250 µm^2	PS (2/10), Malaria parasites /WBC	2016
Nam et al.[55]	0.1 wt.%	focusing	straight rectangular	50 × 120 µm^2	PS (10), WBC	2019
Nam et al.[56]	0.1 wt.%	separation (N)	straight rectangular	50 × 25 µm^2	PS (1~13), Candida/ WBC	2019
Tang et al.[57]	0.3 wt.%	focusing	unconventional cross-section	100 × 100 µm^2	PS (15)	2019
DNA						
Kang et al.[58]	5 ppm	focusing	straight cylindrical	Φ = 50 µm	PS (5.8/10.5)	2013
	5 ppm	separation (Y)	straight square	52 × 52 µm^2	PS (1/2.3/ 4.5/10.5)	
Kim et al.[59]	2.5 ~ 50 ppm	focusing	straight square	50 × 50 µm^2	PS (6/10/15), RBC	2016
Ha et al.[60]	100 ppm	separation (Y)	straight rectangular	30 × 54 µm^2	PS (2/9.9)	2016
Xanthan gum (XG)						
Li et al.[48]	700 ~ 1500 ppm	separation (Y)	straight rectangular with DLD	2000 × 40 µm^2	PS (7.1~18.9)	2018
Extracellular polymeric substances (EPSs)						
Kim et al.[61]	N/A	focusing	straight square	50 × 50 µm^2	PS (3/6.27 /10.2)	2018
		focusing	spiral rectangular	100 × 25 µm^2		
Blood						
Zhou et al.[62]	1× ~ 200× dilution	separation (Y)	straight rectangular	100 × 50 µm^2	PS (18.7) Hep G2 cells blood	2018

[a]Note: separation (Y/N) denotes separating particle with or without sheath flow.

Even though most non-Newtonian fluids contain a positive first normal stress difference and negligible second normal stress difference, there are certain fluids that have unconventional normal stress difference properties. Polyacrylamide (PAA), for instance, has reported having a large second normal stress difference. If the particle-PAA mixture is focused towards channel sidewall by particle-free PAA sheath flow, the small particle will not remain in the pinched flow as its behavior in other non-Newtonian fluids but will disperse across the whole channel due to the secondary flow generated by the non-zero second normal stress difference.[14] Recently, a polymer with negative first normal stress difference, namely hydroxypropyl cellulose (HPC), had been investigated to manipulate particles.[63] In an AR = 2 (aspect ratio, AR = width/height) straight rectangular channel, the particles were found to focus towards two off-center size-based streams and naturally produced a sheathless separator.

1.3 Overview of the dissertation

This dissertation consists of seven chapters. Chapter 1 gives an introduction as well as a brief review about the various non-Newtonian fluids that are often used in the microchannel to manipulate particles. In Chapter 2, we use five types of fluids: DI water, PVP, XG, PEO and PAA to study both the sole and combined fluid rheological and inertial effects on particle motion in a straight rectangular microchannel. In Chapter 3, we demonstrate the use of viscoelastic PEO solution for an efficient sheath-free separation of polystyrene particles by size. We also propose a theoretical understanding of the elastic lift force on particle migration. In Chapter 4, we demonstrate the use of the sheathless particle separation approach in a PEO solution to sort drug-treated *C. neoformans* by morphology. In Chapter 5, we perform a systematic study of the various parameters on the migration of polystyrene particles in the flow of shear-thinning XG solutions through straight rectangular microchannels. In Chapter 6, we demonstrate the use of XG solutions to separate polystyrene particles by size in a continuous sheath-free manner. In Chapter 7, we summarize the contributions of this dissertation and also propose some future work that is based upon our work.

As the results presented in Chapter 2 to 5 have all been published, the content of the corresponding journal articles will be directly used in this dissertation with a modified format if needed. The article that presents the results in Chapter 6 is currently under revision.

References

[1] Plaks, V., Koopman, C.D. and Werb, Z., 2013. Circulating tumor cells. *Science*, **341**(6151), pp.1186-1188.

[2] Lu, X., Liu, C., Hu, G. and Xuan, X., 2017. Particle manipulations in non-Newtonian microfluidics: A review. *Journal of colloid and interface science*, **500**, pp.182-201.

[3] Zhang, J., Yan, S., Yuan, D., Alici, G., Nguyen, N.T., Warkiani, M.E. and Li, W., 2016. Fundamentals and applications of inertial microfluidics: A review. *Lab on a Chip*, **16**(1), pp.10-34.

[4] Segre, G. and Silberberg, A., 1961. Radial particle displacements in Poiseuille flow of suspensions. *Nature*, **189**(4760), p.209.

[5] Di Carlo, D., 2009. Inertial microfluidics. *Lab on a Chip*, 9(21), pp.3038-3046.

[6] Amini, H., Lee, W. and Di Carlo, D., 2014. Inertial microfluidic physics. *Lab on a Chip*, **14**(15), pp.2739-2761.

[7] Bird, R.B., Armstrong, R.C. and Hassager, O., 1987. Dynamics of polymeric liquids. Vol. 1: Fluid mechanics. John Wiley and Sons.

[8] Barnes, H.A., Hutton, J.F. and Walters, K., 1989. An introduction to rheology. Elsevier.

[9] Yang, S., Kim, J.Y., Lee, S.J., Lee, S.S. and Kim, J.M., 2011. Sheathless elasto-inertial particle focusing and continuous separation in a straight rectangular microchannel. *Lab on a Chip*, **11**(2), pp.266-273.

[10] Kim, J.Y., Ahn, S.W., Lee, S.S. and Kim, J.M., 2012. Lateral migration and focusing of colloidal particles and DNA molecules under viscoelastic flow. *Lab on a Chip*, **12**(16), pp.2807-2814.

[11] Nam, J., Lim, H., Kim, D., Jung, H. and Shin, S., 2012. Continuous separation of microparticles in a microfluidic channel via the elasto-inertial effect of non-Newtonian fluid. *Lab on a Chip*, **12**(7), pp.1347-1354.

[12] Lee, D.J., Brenner, H., Youn, J.R. and Song, Y.S., 2013. Multiplex particle focusing via hydrodynamic force in viscoelastic fluids. *Scientific reports*, **3**, p.3258.

[13] Seo, K.W., Kang, Y.J. and Lee, S.J., 2014. Lateral migration and focusing of microspheres in a microchannel flow of viscoelastic fluids. *Physics of Fluids*, **26**(6), p.063301.

[14] Lim, H., Nam, J. and Shin, S., 2014. Lateral migration of particles suspended in viscoelastic fluids in a microchannel flow. *Microfluidics and Nanofluidics*, **17**(4), pp.683-692.

[15] De Santo, I., D’Avino, G., Romeo, G., Greco, F., Netti, P.A. and Maffettone, P.L., 2014. Microfluidic lagrangian trap for brownian particles: Three-dimensional focusing down to the nanoscale. *Physical Review Applied*, **2**(6), p.064001.

[16] Del Giudice, F., D’Avino, G., Greco, F., Netti, P.A. and Maffettone, P.L., 2015. Effect of fluid rheology on particle migration in a square-shaped microchannel. *Microfluidics and Nanofluidics*, **19**(1), pp.95-104.

[17] Liu, C., Xue, C., Chen, X., Shan, L., Tian, Y. and Hu, G., 2015. Size-based separation of particles and cells utilizing viscoelastic effects in straight microchannels. *Analytical Chemistry*, **87**(12), pp.6041-6048.

[18] Yuan, D., Zhang, J., Yan, S., Pan, C., Alici, G., Nguyen, N.T. and Li, W.H., 2015. Dean-flow-coupled elasto-inertial three-dimensional particle focusing under viscoelastic flow in a straight channel with asymmetrical expansion–contraction cavity arrays. *Biomicrofluidics*, **9**(4), p.044108.

[19] Lu, X. and Xuan, X., 2015. Continuous microfluidic particle separation via elasto-inertial pinched flow fractionation. *Analytical Chemistry*, **87**(12), pp.6389-6396.

[20] Lu, X. and Xuan, X., 2015. Elasto-inertial pinched flow fractionation for continuous shape-based particle separation. *Analytical Chemistry*, **87**(22), pp.11523-11530.

[21] Lu, X., Zhu, L., Hua, R.M. and Xuan, X., 2015. Continuous sheath-free separation of particles by shape in viscoelastic fluids. *Applied Physics Letters*, **107**(26), p.264102.

[22] Ahn, S.W., Lee, S.S., Lee, S.J. and Kim, J.M., 2015. Microfluidic particle separator utilizing sheathless elasto-inertial focusing. *Chemical Engineering Science*, **126**, pp.237-243.

[23] Song, H.Y., Lee, S.H., Salehiyan, R. and Hyun, K., 2016. Relationship between particle focusing and dimensionless numbers in elasto-inertial focusing. *Rheologica Acta*, **55**(11-12), pp.889-900.

[24] Xiang, N., Dai, Q. and Ni, Z., 2016. Multi-train elasto-inertial particle focusing in straight microfluidic channels. *Applied Physics Letters*, **109**(13), p.134101.

[25] Xiang, N., Zhang, X., Dai, Q., Cheng, J., Chen, K. and Ni, Z., 2016. Fundamentals of elasto-inertial particle focusing in curved microfluidic channels. *Lab on a Chip*, **16**(14), pp.2626-2635.

[26] Liu, C., Ding, B., Xue, C., Tian, Y., Hu, G. and Sun, J., 2016. Sheathless focusing and separation of diverse nanoparticles in viscoelastic solutions with minimized shear thinning. *Analytical Chemistry*, **88**(24), pp.12547-12553.

[27] Yuan, D., Zhang, J., Sluyter, R., Zhao, Q., Yan, S., Alici, G. and Li, W., 2016. Continuous plasma extraction under viscoelastic fluid in a straight channel with asymmetrical expansion–contraction cavity arrays. *Lab on a Chip*, **16**(20), pp.3919-3928.

[28] Faridi, M.A., Ramachandraiah, H., Banerjee, I., Ardabili, S., Zelenin, S. and Russom, A., 2017. Elasto-inertial microfluidics for bacteria separation from whole blood for sepsis diagnostics. *Journal of Nanobiotechnology*, **15**(1), p.3.

[29] Holzner, G., Stavrakis, S. and DeMello, A., 2017. Elasto-inertial focusing of mammalian cells and bacteria using low molecular, low viscosity PEO solutions. *Analytical Chemistry*, **89**(21), pp.11653-11663.

[30] Liu, C., Guo, J., Tian, F., Yang, N., Yan, F., Ding, Y., Wei, J., Hu, G., Nie, G. and Sun, J., 2017. Field-free isolation of exosomes from extracellular vesicles by microfluidic viscoelastic flows. *ACS nano*, **11**(7), pp.6968-6976.

[31] Tian, F., Zhang, W., Cai, L., Li, S., Hu, G., Cong, Y., Liu, C., Li, T. and Sun, J., 2017. Microfluidic co-flow of Newtonian and viscoelastic fluids for high-resolution separation of microparticles. *Lab on a Chip,* **17**(18), pp.3078-3085.

[32] Yang, S.H., Lee, D.J., Youn, J.R. and Song, Y.S., 2017. Multiple-line particle focusing under viscoelastic flow in a microfluidic device. *Analytical Chemistry,* **89**(6), pp.3639-3647.

[33] Yuan, D., Tan, S.H., Zhao, Q., Yan, S., Sluyter, R., Nguyen, N.T., Zhang, J. and Li, W., 2017. Sheathless Dean-flow-coupled elasto-inertial particle focusing and separation in viscoelastic fluid. *RSC Advances,* **7**(6), pp.3461-3469.

[34] Yuan, D., Tan, S.H., Sluyter, R., Zhao, Q., Yan, S., Nguyen, N.T., Guo, J., Zhang, J. and Li, W., 2017. On-chip microparticle and cell washing using coflow of viscoelastic fluid and newtonian fluid. *Analytical Chemistry,* **89**(17), pp.9574-9582.

[35] Tian, F., Cai, L., Chang, J., Li, S., Liu, C., Li, T. and Sun, J., 2018. Label-free isolation of rare tumor cells from untreated whole blood by interfacial viscoelastic microfluidics. *Lab on a Chip,* **18**(22), pp.3436-3445.

[36] Yuan, D., Sluyter, R., Zhao, Q., Tang, S., Yan, S., Yun, G., Li, M., Zhang, J. and Li, W., 2019. Dean-flow-coupled elasto-inertial particle and cell focusing in symmetric serpentine microchannels. *Microfluidics and Nanofluidics*, **23**(3), p.41.

[37] Zhou, Y., Ma, Z., Tayebi, M. and Ai, Y., 2019. Submicron particle focusing and exosome sorting by wavy microchannel structures within viscoelastic fluids. *Analytical Chemistry,* **91**(7), pp.4577-4584.

[38] Leshansky, A.M., Bransky, A., Korin, N. and Dinnar, U., 2007. Tunable nonlinear viscoelastic "focusing" in a microfluidic device. *Physical Review Letters*, **98**(23), p.234501.

[39] D'Avino, G., Romeo, G., Villone, M.M., Greco, F., Netti, P.A. and Maffettone, P.L., 2012. Single line particle focusing induced by viscoelasticity of the suspending liquid: theory, experiments and simulations to design a micropipe flow-focuser. *Lab on a Chip,* **12**(9), pp.1638-1645.

[40] Yang, S., Lee, S.S., Ahn, S.W., Kang, K., Shim, W., Lee, G., Hyun, K. and Kim, J.M., 2012. Deformability-selective particle entrainment and separation in a rectangular microchannel using medium viscoelasticity. *Soft Matter,* **8**(18), pp.5011-5019.

[41] Romeo, G., D'Avino, G., Greco, F., Netti, P.A. and Maffettone, P.L., 2013. Viscoelastic flow-focusing in microchannels: scaling properties of the particle radial distributions. *Lab on a Chip,* **13**(14), pp.2802-2807.

[42] Del Giudice, F., Romeo, G., D'Avino, G., Greco, F., Netti, P.A. and Maffettone, P.L., 2013. Particle alignment in a viscoelastic liquid flowing in a square-shaped microchannel. *Lab on a Chip*, **13**(21), pp.4263-4271.

[43] Seo, K.W., Kang, Y.J. and Lee, S.J., 2014. Lateral migration and focusing of microspheres in a microchannel flow of viscoelastic fluids. *Physics of Fluids*, **26**(6), p.063301.

[44] Won Seo, K., Ran Ha, Y. and Joon Lee, S., 2014. Vertical focusing and cell ordering in a microchannel via viscoelasticity: Applications for cell monitoring using a digital holographic microscopy. *Applied Physics Letters*, **104**(21), p.213702.

[45] Cha, S., Kang, K., You, J.B., Im, S.G., Kim, Y. and Kim, J.M., 2014. Hoop stress-assisted three-dimensional particle focusing under viscoelastic flow. *Rheologica Acta*, **53**(12), pp.927-933.

[46] Nam, J., Namgung, B., Lim, C.T., Bae, J.E., Leo, H.L., Cho, K.S. and Kim, S., 2015. Microfluidic device for sheathless particle focusing and separation using a viscoelastic fluid. *Journal of Chromatography A*, **1406**, pp.244-250.

[47] Go, T., Byeon, H. and Lee, S.J., 2017. Focusing and alignment of erythrocytes in a viscoelastic medium. *Scientific reports*, **7**, p.41162.

[48] Li, Y., Zhang, H., Li, Y., Li, X., Wu, J., Qian, S. and Li, F., 2018. Dynamic control of particle separation in deterministic lateral displacement separator with viscoelastic fluids. *Scientific reports*, **8**(1), p.3618.

[49] Xiang, N., Ni, Z. and Yi, H., 2018. Concentration-controlled particle focusing in spiral elasto-inertial microfluidic devices. *Electrophoresis*, **39**(2), pp.417-424.

[50] Nam, J., Yoon, J., Kim, J., Jang, W.S. and Lim, C.S., 2019. Continuous erythrocyte removal and leukocyte separation from whole blood based on viscoelastic cell focusing and the margination phenomenon. *Journal of Chromatography A*, **1595**, pp.230-239.

[51] Xiang, N., Dai, Q., Han, Y. and Ni, Z., 2019. Circular-channel particle focuser utilizing viscoelastic focusing. *Microfluidics and Nanofluidics*, **23**(2), p.16.

[52] Lim, E.J., Ober, T.J., Edd, J.F., Desai, S.P., Neal, D., Bong, K.W., Doyle, P.S., McKinley, G.H. and Toner, M., 2014. Inertio-elastic focusing of bioparticles in microchannels at high throughput. *Nature Communications*, **5**, p.4120.

[53] Nam, J., Tan, J.K.S., Khoo, B.L., Namgung, B., Leo, H.L., Lim, C.T. and Kim, S., 2015. Hybrid capillary-inserted microfluidic device for sheathless particle focusing and separation in viscoelastic flow. *Biomicrofluidics*, **9**(6), p.064117.

[54] Nam, J., Shin, Y., Tan, J.K.S., Lim, Y.B., Lim, C.T. and Kim, S., 2016. High-throughput malaria parasite separation using a viscoelastic fluid for ultrasensitive PCR detection. *Lab on a Chip*, **16**(11), pp.2086-2092.

[55] Nam, J., Jang, W.S. and Lim, C.S., 2019. Non-electrical powered continuous cell concentration for enumeration of residual white blood cells in WBC-depleted blood using a viscoelastic fluid. *Talanta*, **197**, pp.12-19.

[56] Nam, J., Jang, W.S. and Lim, C.S., 2019. Viscoelastic Separation and Concentration of Fungi from Blood for Highly Sensitive Molecular Diagnostics. *Scientific Reports*, **9**(1), p.3067.

[57] Tang, W., Fan, N., Yang, J., Li, Z., Zhu, L., Jiang, D., Shi, J. and Xiang, N., 2019. Elasto-inertial particle focusing in 3D-printed microchannels with unconventional cross sections. *Microfluidics and Nanofluidics*, **23**(3), p.42.

[58] Kang, K., Lee, S.S., Hyun, K., Lee, S.J. and Kim, J.M., 2013. DNA-based highly tunable particle focuser. *Nature Communications*, **4**, p.2567.

[59] Kim, B. and Kim, J.M., 2016. Elasto-inertial particle focusing under the viscoelastic flow of DNA solution in a square channel. *Biomicrofluidics*, **10**(2), p.024111.

[60] Ha, B., Park, J., Destgeer, G., Jung, J.H. and Sung, H.J., 2016. Transfer of microparticles across laminar streams from non-Newtonian to Newtonian fluid. *Analytical Chemistry*, **88**(8), pp.4205-4210.

[61] Kim, M.J., Youn, J.R. and Song, Y.S., 2018. Focusing manipulation of microalgae in a microfluidic device using self-produced macromolecules. *Lab on a Chip*, **18**(7), pp.1017-1025.

[62] Zhou, J., Tu, C., Liang, Y., Huang, B., Fang, Y., Liang, X., Papautsky, I. and Ye, X., 2018. Isolation of cells from whole blood using shear-induced diffusion. *Scientific Reports*, **8**(1), p.9411.

[63] Yang, S.H., Lee, D.J., Youn, J.R. and Song, Y.S., 2019. Double-line particle focusing induced by negative normal stress difference in a microfluidic channel. *Microfluidics and Nanofluidics*, **23**(2), p.21.

CHAPTER TWO

FLUID RHEOLOGY EFFECTS ON PARTICLE MIGRATION IN A STRAIGHT RECTANGULAR MICROCHANNEL

2.1 Abstract

There has recently been a significantly increasing interest in the passive manipulation of particles in the flow of non-Newtonian fluids through microchannels. However, an accurate and comprehensive understanding of the various fluid rheological effects on particle migration is still largely missing. We present in this work a systematic experimental study of both the individual and the combined effects of fluid inertia, elasticity and shear thinning on the motion of rigid spherical particles in a straight rectangular microchannel. We first study the sole effect of each of these rheological properties in a Newtonian fluid, purely elastic (i.e., Boger) fluid, and purely shear-thinning (i.e., pseudoplastic) fluid, respectively. We then study the combined effects of two or all of these rheological properties in a pseudoplastic fluid and two types of elastic shear-thinning fluids, respectively. We find that the fluid elasticity effect directs particles towards the centerline of the channel while the fluid shear-thinning effect causes particle migration towards both the centerline and corners. These two effects are combined with the fluid inertial effect to understand the particle migration in inertial pseudoplastic and viscoelastic fluid flows.

2.2 Introduction

Manipulating precisely the motion of particles in microchannels is important for microfluidic devices to achieve focusing[64], trapping[19], concentration[50], washing[60] and separation[54] etc. for various chemical and biological applications. It has been typically implemented by imposing a force field, such as electric[34], magnetic[16], acoustic[48] or optical[27] force, relative to the flow. This type of *active* methods often suffers from a relatively low throughput due to the limited action time of the external force[24]. In contrast, the *passive* control of particle motion by the use of the flow induced lift and/or drag forces has the potential to achieve a high throughput with also the advantages of simplicity and effectiveness[42,65]. It has thus been increasingly studied in the past decade, which can take place in either a Newtonian fluid[2,12] or a non-Newtonian fluid[7,8].

Fluid inertia has been demonstrated to cause a transverse migration of particles in a confined flow of Newtonian fluids[17,31,58], yielding the so-called inertial focusing in microchannels for a variety of lab-on-a-chip applications[47,71]. In non-Newtonian fluids, particle migration can occur even in a flow with negligible inertial effects[25,26], which is attributed to an additional force arising from the gradients of normal stresses in the undisturbed flow[18]. This force is often termed viscoelastic or simply elastic lift in the microfluidics community[42,44,70], as distinguished from the inertial lift[2,47,71]. The sole action of the elastic lift and as well the mutual action of the elastic/inertial lifts on particle migration have been investigated in the flow of various polymer solutions [e.g., polyvinylpyrrolidone (PVP)[53,9,62], polyethylene oxide (PEO)[32,35,40,45,46,63,69] and polyacrylamide (PAA)[33,39]] and biological fluids [e.g., hyaluronic acid (HA) [38,49] and DNA solutions[23,28]] through different microchannels. They are found to be a strong function of fluid rheological properties including elasticity and shear thinning.

The fluid elasticity effect has been long known[30] to direct particles towards the region of the lowest absolute shear rate, which is the centerline for a plane or cylindrical Poiseuille flow[26,33,57] and the centerline/corners for a rectangular Poiseuille flow[56,61,67]. This migration can be significantly influenced by the fluid inertial effect[36,61,66]. The fluid shear thinning effect has been demonstrated to promote the particle migration away from the channel centerline[6,10,11,20,41,55,56,59] in confined viscoelastic flows. It becomes more pronounced as the fluid inertial and elasticity effects increase [36,61]. However, the sole effect of fluid shear thinning has been nearly unexplored except the work from Gauthier et al.[14,15]. In those two studies, rigid particles were observed to migrate in the direction of maximum shear rate in a purely viscous fluid with strong shear-thinning (labelled pseudoplastic) in two-dimensional Couette[14] and Poiseuille[15] flows, respectively. This migration was found opposite to that of particles suspended in a viscoelastic fluid.

The aim of this work is to decompose the effects of fluid rheological properties on particle migration in a straight rectangular microchannel via a systematic experimental investigation. We first study the sole effect of fluid inertia, fluid elasticity and fluid shear thinning on the migration of rigid spherical particles in a Newtonian fluid, purely elastic fluid [i.e., Boger fluid[21]] and pseudoplastic fluid, respectively. We then study the combined effects of two or all of these rheological properties on the migration of the same particles in the inertial flow of pseudoplastic and (two types of) elastic shear-thinning fluids, respectively. We also attempt to understand these combined fluid rheological effects using the sole effect of each property.

2.3 Experiment

Spherical 10 µm-diameter polystyrene particles (Thermo Scientific) were used in all experiments. They were re-suspended in five types of water-based solutions with different rheological properties: (1) Newtonian fluid with a constant viscosity — water; (2) Purely elastic fluid with a negligible shear-thinning effect — 5% PVP solution (molecular weight, $M_w = 0.36 \times 10^6$ Da, Sigma-Aldrich); (3) Pseudoplastic fluid with a strong shear thinning effect — 2000 ppm xanthan (Tokyo Chemical Industry) solution; (4) Viscoelastic fluid with a weak shear-thinning effect — 1000 ppm PEO solution ($M_w = 2 \times 10^6$ Da, Sigma-Aldrich); (5) Viscoelastic fluid with a strong shear-thinning effect — 200 ppm PAA solution ($M_w = 18 \times 10^6$ Da, Polysciences). Each of these solutions was mixed with glycerol (Fisher Scientific) at the volume ratio of 78:22, such that polystyrene particles suspended therein become neutrally buoyant. Due to the lack of measuring equipment in our lab, the approximate rheological properties of these solutions were obtained from the literature (Table 2.1). Note that none of the polymer solutions listed in the table contains glycerol, and so the real values of the fluid viscosity and relaxation time for our prepared polymer solutions should be greater.

Table 2.1. Important rheological properties of the prepared solutions (without glycerol except water, estimated at 20 °C).

Solution	Polymer concentration	Relaxation time, λ (ms)	Power-law index, n	Zero-shear viscosity, η_0 (mPa•s)
Water[5]	0	0	1	1.86
PVP[43]	5%	2.2	~1	28
Xanthan[22]	2000 ppm	~0	0.66	3680
PEO[52]	1000 ppm	1.5	0.977	2.3
PAA[51]	200 ppm	95	0.623	22

Fig. 2.1. (a) shows a picture of the rectangular microchannel, which was fabricated with polydimethylsiloxane (PDMS) using a custom-modified soft lithography technique as described elsewhere[37]. The channel is 2 cm long with a measured width of 66 µm and a measured height of 54 µm. It has an expansion region at each end with an array of posts patterned therein for filtering any debris. A right-angle prism (NT 32-526, Edmund Optics Inc.) was used to visualize the particle motion in the vertical plane of the microchannel. It was embedded into the PDMS slab and placed right before the outlet expansion with a 400 µm distance from the microchannel edge. The prepared particle suspension was driven through the microchannel by a syringe pump (KD Scientific). Particle motion was recorded from both the top and side views with an inverted fluorescent microscope (Nikon Eclipse TE2000U, Nikon Instrument) with a CCD camera (Nikon DS-Qi1Mc). The recorded digital images were processed using the Nikon imaging software (NIS-Elements). Superimposed images were obtained by stacking a sequence of snapshot images with the maximum intensity projection.

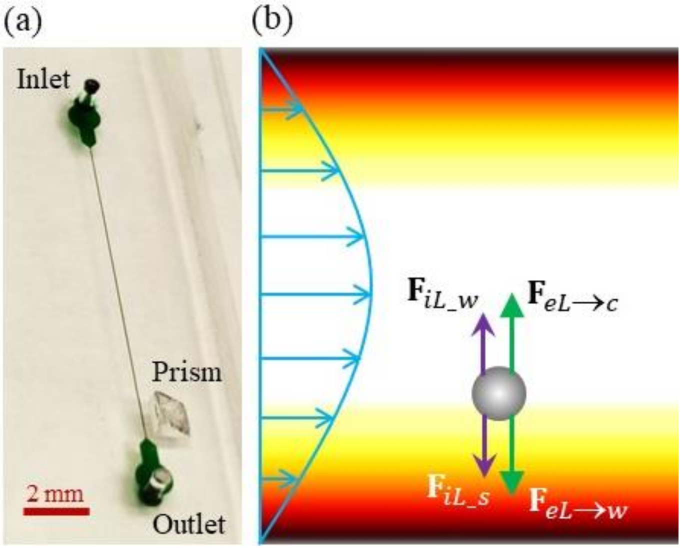

Fig. 2.1. (a) Picture of the straight rectangular microchannel (filled with green food dye for clarity) used in the experiment, where the right-angle prism was embedded into the PDMS slab with a 400 µm distance from the channel edge for the side-viewing of particle motion. (b) Analysis of the inertial and/or elastic lift force components on a neutrally buoyant spherical particle in the flow (see the parallel arrows for the parabolic velocity profile) of Newtonian and viscoelastic fluids through a straight rectangular microchannel (see the text in **section 3** for the definitions of the highlighted symbols). The background color shows the contour of fluid shear rate squared, $\dot{\gamma}^2$ (the darker the larger magnitude), in the horizontal plane of the microchannel.

2.4 Theory

Fig. 2.1. (b) shows the analysis of the inertial and/or elastic lift forces on particles in the flow of Newtonian and viscoelastic fluids through a straight rectangular microchannel. The inertial lift, $\mathbf{F}_{iL}$, results from the inertia of the fluid, and can be broken down into two components for a neutrally buoyant spherical particle, where the wall-induced lift, $\mathbf{F}_{iL\_w}$, pushes the particle away from any channel walls, and the shear gradient-induced lift, $\mathbf{F}_{iL\_s}$, directs the particle away from the channel centerline towards the high

shear-rate region (see the background color in Fig. 2.1. (b))[12]. The following scaling formula has been often used to evaluate the inertial lift[1],

$$\mathbf{F}_{iL} = \mathbf{F}_{iL\_w} + \mathbf{F}_{iL\_s} \sim \rho d^4 \dot{\gamma}^2 \tag{2-1}$$

where ρ is the fluid density, d is the particle diameter, and $\dot{\gamma}$ is the fluid shear rate. This force is a strong function of the Reynolds number, Re,

$$Re = \frac{\rho V D_h}{\eta(\dot{\gamma})} = \frac{2\rho Q}{\eta(\dot{\gamma})(w+h)} \tag{2-2}$$

where V is the average fluid velocity, D_h is the hydraulic diameter of a rectangular microchannel, $\eta(\dot{\gamma})$ is the fluid viscosity, Q is the volumetric flow rate, w is the channel width, and h is the channel height. Another dimensionless number to characterize the inertial lift is the particle Reynolds number,

$$Re_p = Re \left(\frac{d}{D_h}\right)^2 \tag{2-3}$$

which has been demonstrated to be on the order of 1 (or at least $Re_p > 0.1$) for effective inertial focusing of particles. For shear thinning fluids, $\eta(\dot{\gamma})$ in Eq. (2-2) was estimated using the Carreau-Yasuda model[68] at the average shear rate across the channel width, $\bar{\dot{\gamma}} = 2V/w$,

$$\eta = \eta_\infty + \frac{\eta_0 - \eta_\infty}{\left[1 + \left(\lambda_{CY} \bar{\dot{\gamma}}\right)^a\right]^{n/a}} \tag{2-4}$$

where η_∞ is the infinite-shear-rate viscosity, η_0 is the zero-shear-rate viscosity, λ_{CY} is a time constant, n is the power-law index, and a is a fitting parameter introduced by Yasuda et al.[68]. The values of the parameters in Eq. (2-4) (except for η_0 and n that are given in Table 2.1) for our prepared xanthan and PAA solutions (without glycerol) are given in

Table 2.2. For non- and weakly shear thinning fluids (i.e., water, PVP and PEO solutions), $\eta(\dot{\gamma})$ was set to be η_0 in Table 2.1.

Table 2.2. Parameters involved in the Carreau-Yasuda model for estimating the viscosity of the prepared xanthan and PAA solutions (without glycerol, estimated at 20 °C).

Solution	Time constant, λ_{CY}	Fitting parameter, a	Infinite shear viscosity, η_∞
Xanthan[22]	21.5 s	0.81	2.24 mPa•s
PAA[51]	0.551 s	0.623	2.62 mPa•s

The elastic lift, $\mathbf{F}_{eL}$, results from the non-uniform normal stress difference in the flow of viscoelastic fluids[18]. Similar to the inertial lift, we have recently proposed to break down $\mathbf{F}_{eL}$ into two opposing components as well[35]: $\mathbf{F}_{eL\to c}$ directs a particle towards the channel center, where the fluid shear rate is the lowest (see the contour in Fig. 2.1 (b)), due to the effect of fluid elasticity; $\mathbf{F}_{eL\to w}$ directs the particle towards the channel walls (or more accurately, the corners) due to the effects of fluid elasticity and/or shear thinning. Considering that the first normal stress difference often plays a dominant role in polymer solutions[3], the elastic lift may be expressed in the following scale[4],

$$\mathbf{F}_{eL} = \mathbf{F}_{eL\to c} + \mathbf{F}_{eL\to w} \sim d^3 \nabla(\Psi_1 \dot{\gamma}^2) \tag{2-5}$$

where Ψ_1 is the first normal stress difference coefficient as a function of fluid rheological properties and shear rate. It can be characterized by the Weissenberg number, Wi, in terms of the average fluid shear rate across the channel width, $\bar{\dot{\gamma}}$,

$$Wi = \lambda \bar{\dot{\gamma}} = \lambda \frac{2V}{w} = \frac{2\lambda Q}{w^2 h} \tag{2-6}$$

where λ is the fluid relaxation time. The relative contribution between $\mathbf{F}_{eL}$ and $\mathbf{F}_{iL}$ is dependent on the ratio of the Weissenberg number to Reynolds number, i.e., the elasticity number, El,

$$El = \frac{Wi}{Re} = \frac{\lambda\eta(\dot{\gamma})(w+h)}{\rho w^2 h} \tag{2-7}$$

As the two lift forces are both functions of fluid rheological properties, where the most important ones are the elasticity, shear-thinning and inertial effects [in terms of λ and $\eta(\dot{\gamma})$, respectively, in Eq. (2-6)], particle migration is expected to vary in different types of non-Newtonian fluids.

2.5 Results and discussion

2.5.1 Sole effect of fluid inertia

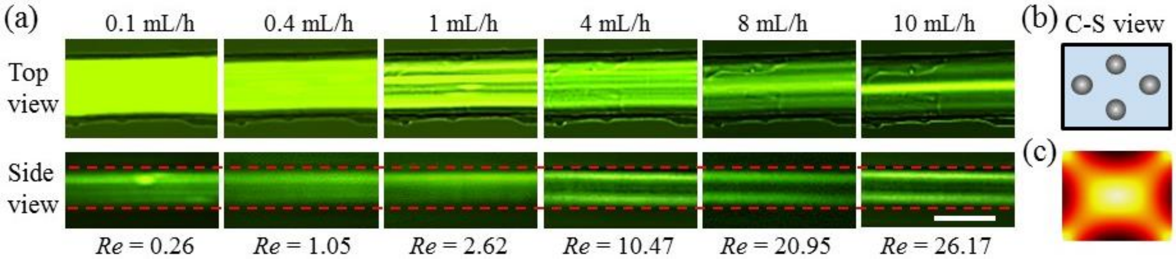

Fig. 2.2. Particle migration in the flow of a Newtonian water/glycerol solution through the straight rectangular microchannel: (a) top- (upper row) and side- (lower row) view images of 10 µm-diameter particles at the channel outlet in a range of flow rates; (b) schematic of the equilibrium particle positions in the cross-sectional (C-S) view; (c) contour of the fluid shear rate, $\dot{\gamma}$, over the channel cross-section (the darker the larger magnitude). The scale bar in (a) represents 50 µm.

Fig. 2.2. (a) shows the migration of 10 µm particles in a Newtonian water/glycerol flow through a straight rectangular microchannel under the influence of fluid inertia alone.

For a flow rate of up to 1 mL/h, particles are (almost) evenly distributed in both the width (see the top-view images) and depth (see the side-view images) directions of the channel due to the weak inertial lift at a very small particle Reynolds number, $Re_p \leq 0.073$. As the flow rate increases to 4 mL/h, particles are observed to migrate towards two primary equilibrium positions in the channel depth direction. However, their migrations in the width direction are still not visible until the flow rate is increased to 8 mL/h due to the insufficient length of the channel. Further increasing the flow rate to 10 mL/h yields an apparent particle migration towards the channel centerline in the width direction. There exist two other focused particle streams near the walls that are not clearly seen from the top-view image because they are located at different levels from the particle stream(s) along the centerline. Fig. 2.2. (b) schematically illustrates these four equilibrium particle positions that are each at the center of one side (primarily two in the shorter sides of the channel) in a nearly-square microchannel. Such an inertial focusing of particles in Newtonian fluid flows, as a result of the nearly symmetric distribution of shear rate in the width and depth directions (see Fig. 2.2. (c)), is consistent with previous studies[12,40].

2.5.2 Sole effect of fluid elasticity

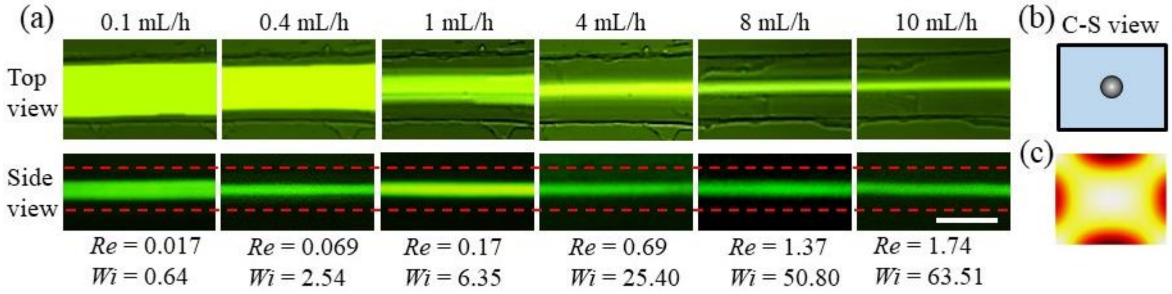

Fig. 2.3. Particle migration in the flow of 5% PVP solution (viscoelastic fluid with a negligible shear-thinning effect) through the straight rectangular microchannel: (a) top- (upper row) and side- (lower row) view images of 10 µm-diameter particles at the channel outlet in a range of flow rates; (b) schematic of the equilibrium particle positions in the cross-sectional (C-S) view; (c) contour of the fluid shear rate squared, $\dot{\gamma}^2$, over the channel cross-section (the darker the larger magnitude). The scale bar in (a) represents 50 µm.

Fig. 2.3. (a) shows the migration of 10 µm particles in 5% PVP solution with the flow rate ranging from 0.1 mL/h to 10 mL/h. As the largest particle Reynolds number (at 10 mL/h) is $Re_p = 0.048 \ll 1$, the influence of fluid inertia can be neglected and hence the particle migration is solely the result of fluid elasticity (the elasticity number is fixed at $El = 36.5$ due to its independence of fluid kinematics). At the flow rate of 0.1 mL/h, particles are found to stay slightly away from the channel sidewalls in the top-view image of Fig. 2.3. (a). They, however, already exhibit an apparent migration towards the channel center in the depth direction due to the larger gradient of shear rate squared therein (Fig. 2.3. (c)). With the increase of flow rate, such an elastic particle focusing effect becomes stronger due to the enhanced elastic lift in terms of the Weissenberg number, especially significant in the channel width direction (Fig. 2.3. (a)). Its equilibrium position is right at the central axis of the rectangular microchannel as schematically illustrated in Fig. 2.3. (b). This observation is consistent with earlier studies[9,53,62]. It is, however, inconsistent with the observation of Yang et al.[66,67], where near-corner motions of rigid particles were reported in an exactly square microchannel. The reason behind this discrepancy is currently unknown, which may be partially because the low shear-rate region near every corner of the channel cross-section (Fig. 2.3. (c)) is too small to confine 10 µm particles in our experiment due to the steric effects.

2.5.3 Sole effect of fluid shear-thinning

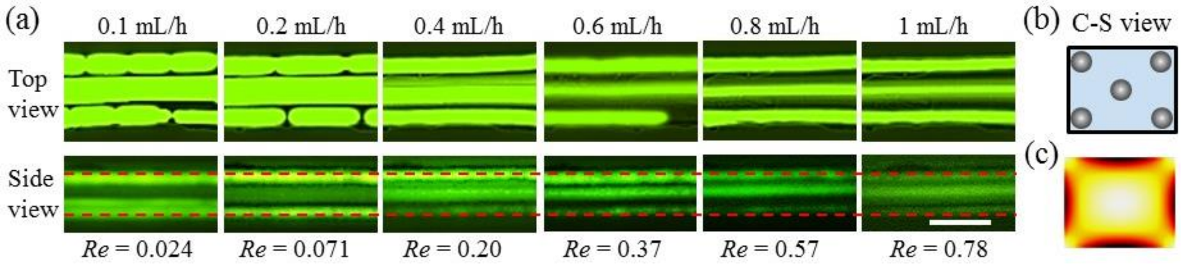

Fig. 2.4. Particle migration in an inertialess flow of 2000 ppm xanthan solution (pseudoplastic fluid with a strong shear-thinning effect) through the straight rectangular microchannel: (a) top- (upper row) and side- (lower row) view images of 10 µm-diameter particles at the channel outlet in a range of flow rates from 0.1 mL/h to 1 mL/h; (b) schematic of the equilibrium particle positions in the cross-sectional (C-S) view; (c) contour of the fluid shear rate, $\dot{\gamma}$, over the channel cross-section (the darker the larger magnitude). The scale bar in (a) represents 50 µm.

Fig. 2.4. (a) shows the migration of 10 µm particles in the flow of pseudoplastic 2000 ppm xanthan solution through the straight rectangular microchannel. To isolate the fluid shear thinning effect from the inertial effect, the flow rate is kept no more than 1 mL/h so that the Reynolds number is at most 0.78 (at which $Re_p = 0.022 \ll 1$). Different from those in water (Fig. 2.2. (a)) and PVP solution (Fig. 2.3. (a)), particles in xanthan solution (Fig. 2.4. (a)) migrate towards the walls (more specifically, the corners) and centerline of the channel in both the width (top view) and depth (side view) directions in an inertialess flow. Moreover, this bidirectional particle migration is observed to increase at higher flow rates in Fig. 2.4. (a). The equilibrium positions of such a fluid shear-thinning induced particle focusing are schematically illustrated in Fig. 2.3. (b), which should be correlated with the significantly expanded low shear-rate region over the channel cross-section in a shear-thinning fluid (Fig. 2.3. (c)). They seem to be qualitatively consistent with a couple

of recent numerical studies that predict the fluid shear-thinning promoted particle migration in a viscoelastic fluid towards both the corners and the centerline of a square microchannel[36,61]. They are also partially consistent with several other experimental and numerical studies, where the fluid shear thinning effect has been demonstrated to weaken the elastic focusing of particles along the channel centerline in viscoelastic fluids[6,7,10,11,20,41,55,56,59]. More studies on particle migration in pseudoplastic fluids are needed.

2.5.4 Combined effect of fluid shear-thinning and inertia

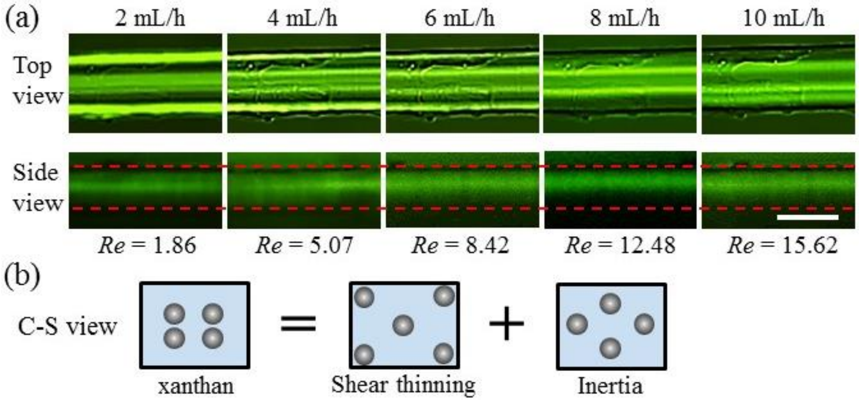

Fig. 2.5. Particle migration in an inertial flow of 2000 ppm xanthan solution (pseudoplastic fluid with a strong shear-thinning effect) through the straight rectangular microchannel: (a) top- (upper row) and side- (lower row) view images of 10 µm-diameter particles at the channel outlet in a range of flow rates from 2 mL/h to 10 mL/h; (b) schematic explanation of the equilibrium particle positions in the cross-sectional (C-S) view due to the combined effects of fluid shear thinning and inertia. The scale bar in (a) represents 50 µm.

Fig. 2.5. (a) shows the migration of 10 µm particles in 2000 ppm xanthan solution when the flow rate goes beyond 1 mL/h. At 2 mL/h, the Reynolds number is 1.86 and the particle Reynolds number, $Re_p = 0.052$, gets closer to 0.1. Therefore, the fluid inertia starts playing a role and, though still weak, pushing some of the particles away from the

corners of channel as seen from the side-view image. This inertial effect quickly grows at 4 mL/h due to the fluid shear thinning effect, where the Reynolds number increases to 5.07 and the particle Reynolds number, $Re_p = 0.14$, becomes greater than 0.1. As a consequence, fewer particles stay near the walls in the top-view image as compared to 2 mL/h. Moreover, the particle stream along the center of the channel in the width direction begins to split into two, which becomes more obvious at 6 mL/h. When the flow rate increases to 8 mL/h and above, we observe only two off-center particle streams in the width direction and one wide stream along the centerline in the depth direction. The equilibrium particle positions in the xanthan solution are schematically illustrated in Fig. 2.5. (b) as a result of the combined action of the fluid shear thinning-induced focusing (Fig. 2.4. (b)) and the fluid inertia-induced focusing (Fig. 2.2. (b)). Note that we use two nearly touching particles in the channel depth direction of the schematic in Fig. 2.5. (b) to reflect the wider particle stream in the xanthan solution than that in the PVP solution (Fig. 2.3. (b)).

2.5.5 Combined effect of fluid elasticity, weak-shear-thinning and inertia

Fig. 2.6. (a) shows the migration of 10 μm particles in the flow of 1000 ppm PEO solution through the straight rectangular microchannel. As the PEO solution has a weak shear thinning effect (with a power-law index of 0.977, see Table 2.1), the elasticity number in the range of flow rates under test remains approximately at $El = 9.29$. This value is only a quarter of that of 5% PVP solution ($El = 36.5$) (Fig. 2.3. (a)), indicating a moderate elasticity in the PEO solution. It is, however, still much larger than 1, so the elastic lift should dominate the inertial lift in all flow rates[7,8]. As a consequence, particles

already achieve an effective elastic focusing along the central axis of the channel at 0.1 mL/h ($Re = 0.21$), which is apparently better than that in the more elastic PVP solution (Fig. 2.3. (a)). This is because the Weissenberg number in the PEO solution, $Wi = 1.96$, is two times greater than in the PVP solution ($Wi = 0.64$) due to the significantly lower viscosity of the former (Table 2.1). The effect of the weak shear thinning of the PEO solution is clearly observed at an even lower flow rate of 0.05 mL/h, where particles migrate towards both the center and corners of the channel like that in the inertialess xanthan solution (Fig. 2.4. (a)).

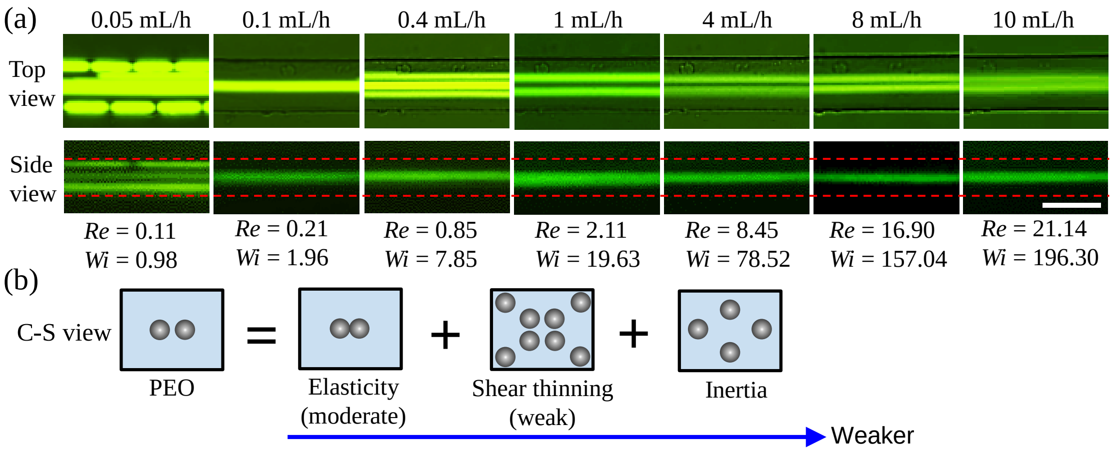

Fig. 2.6. Particle migration in the flow of 1000 ppm PEO solution (viscoelastic fluid with a weak shear thinning effect) through the straight rectangular microchannel: (a) top- (upper row) and side- (lower row) view images of 10 μm-diameter particles at the channel outlet in a range of flow rates; (b) schematic explanation of the equilibrium particle positions in the cross-sectional (C-S) view due to the combined effects of fluid elasticity, shear thinning and inertia in the decreasing order of role (highlighted by the long arrow). The scale bar in (a) represents 50 μm.

Increasing the flow rate to 0.4 mL/h ($Re = 0.85$) causes the migration of part of the particles from the center to two symmetric off-center positions in the channel width direction due to perhaps the increased shear-thinning and inertial effects. Such a triple-stream particle focusing pattern has also been reported in previous studies[35,40,45,63]. It quickly converts to a dual-stream pattern with the central one disappearing at 0.6 mL/h (data not shown), which then holds with the further increase of flow rate. However, the distance between the two streams seems to slowly decrease at higher flow rates, which is consistent with earlier studies[35,40,45,63] and may be a consequence of the weak fluid shear-thinning effect that increases the role of the elastic lift due to the slightly increasing elasticity number. The equilibrium particle positions in the PEO solution are schematically illustrated in Fig. 2.6. (b) as a result of the combined effect of fluid elasticity (mild) (Fig. 2.3. (b)), shear-thinning (weak) (Fig. 2.4. (b)) and inertia (Fig. 2.2. (b)) in the decreasing order of role.

2.5.6 Combined effect of fluid elasticity, strong-shear-thinning and inertia

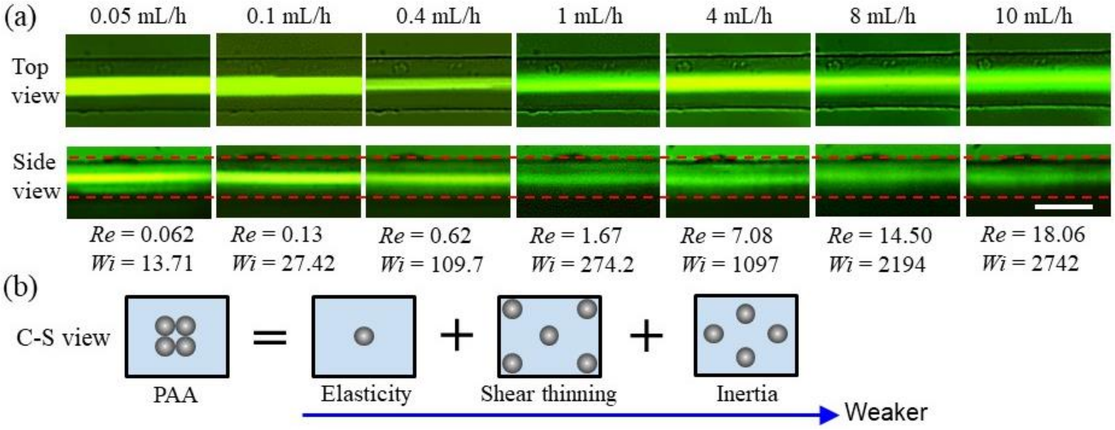

Fig. 2.7. Particle migration in the flow of 200 ppm PAA solution (strongly viscoelastic fluid with a strong shear-thinning effect) through the straight rectangular microchannel: (a) top- (upper row) and side- (lower row) view images of 10 µm-diameter particles at the channel outlet in a range of flow rates; (b) schematic explanation of the equilibrium particle positions in the cross-sectional (C-S) view due to the combined effects of fluid elasticity, shear thinning and inertia in the decreasing order of role (highlighted by the long arrow). The scale bar in (a) represents 50 µm.

Fig. 2.7. (a) shows the migration of 10 µm particles in 200 ppm PAA solution through the straight rectangular microchannel. The calculated elasticity number of this solution is, $El = 221.1$, at 0.05 mL/h, which decreases to 151.8 at 10 mL/h due to the fluid's strong shear thinning effect (causing a quick increase in the Reynolds number). As the lowest value of El is still significantly higher that of PVP solution ($El = 36.5$), the PAA solution should be of very strong elasticity. Therefore, particles migrate towards the centerline of the channel in both the width and depth directions even at the flow rate of 0.05 mL/h ($Re = 0.062$). No near-wall particles are observed because the fluid elasticity plays a stronger role than the fluid shear thinning. Such a single-stream particle focusing holds true in the whole range of flow rates under test. However, the particle stream width in the channel width direction seems to go through a first-decrease-then-increase trend with the increase of flow rate due to the increasing influence of fluid shear thinning and inertia. We believe it is mainly the fluid shear-thinning effect that defocuses the particles at high flow rates like that observed in the xanthan solution (Fig. 2.5. (a)). The equilibrium particle positions in the PAA solution are schematically illustrated in Fig. 2.7. (b) as a result of the combined effect of the strong fluid elasticity (Fig. 2.3. (b)), strong fluid shear-thinning (Fig. 2.4. (b)), and moderate fluid inertia (Fig. 2.2. (b)).

2.6 Conclusions

We have conducted a systematic experimental study of the migration of 10 μm polystyrene particles in the flow of five different fluids with varying rheological properties through a straight rectangular microchannel with a width/height ratio of 1.22. We find that particles migrate to four equilibrium positions in a Newtonian fluid that are each at the center of one side of the channel due to the flow induced inertial effect. In contrast, they migrate towards the channel centerline in an elastic Boger fluid due to the fluid elasticity effect alone, and towards both the centerline and corners in a pseudoplastic fluid due to the fluid shear thinning effect alone. We have also used these individual fluid rheological effects to understand the particle motion in the inertial flow of both pseudoplastic and viscoelastic fluids. We find that particles migrate to two off-center equilibrium positions in the central plane parallel to the longer side of the channel in the pseudoplastic fluid due to the combined shear thing and inertial effects. The addition of the fluid elasticity effect further alters the particle equilibrium position in viscoelastic fluid flows, which depends strongly on the relative significance of the three rheological effects. These developed fundamental knowledge of particle motion in the flow of various fluids will provide systematic experimental data for calibrating theoretical and numerical models, and more importantly, establish the experimental foundation for efficient *passive* manipulations (e.g., focusing and separation) of various bioparticles in non-Newtonian microfluidic devices with immediate applications to point-of-care technologies.

Acknowledgments This work was supported in part by NSF under grant CBET-1150670 and by Clemson University through a SEED grant.

References

[1] Asmolov, E.S., 1999. The inertial lift on a spherical particle in a plane Poiseuille flow at large channel Reynolds number. *Journal of Fluid Mechanics*, **381**, pp.63-87.

[2] Amini, H., Lee, W. and Di Carlo, D., 2014. Inertial microfluidic physics. *Lab on a Chip*, **14**(15), pp.2739-2761.

[3] Barnes, H.A., Hutton, J.F. and Walters, K., 1989. An introduction to rheology. Elsevier.

[4] Bird, R.B., Armstrong, R.C. and Hassager, O., 1987. Dynamics of polymeric liquids. Vol. 1: Fluid mechanics. John Wiley and Sons.

[5] Cheng, N.S., 2008. Formula for the viscosity of a glycerol− water mixture. *Industrial & engineering chemistry research*, **47**(9), pp.3285-3288.

[6] D'Avino, G., Romeo, G., Villone, M.M., Greco, F., Netti, P.A. and Maffettone, P.L., 2012. Single line particle focusing induced by viscoelasticity of the suspending liquid: theory, experiments and simulations to design a micropipe flow-focuser. *Lab on a Chip*, **12**(9), pp.1638-1645.

[7] D’Avino, G. and Maffettone, P.L., 2015. Particle dynamics in viscoelastic liquids. *Journal of Non-Newtonian Fluid Mechanics*, **215**, pp.80-104.

[8] D'Avino, G., Greco, F. and Maffettone, P.L., 2017. Particle migration due to viscoelasticity of the suspending liquid and its relevance in microfluidic devices. *Annual Review of Fluid Mechanics*, **49**, pp.341-360.

[9] Del Giudice, F., Romeo, G., D'Avino, G., Greco, F., Netti, P.A. and Maffettone, P.L., 2013. Particle alignment in a viscoelastic liquid flowing in a square-shaped microchannel. *Lab on a Chip*, **13**(21), pp.4263-4271.

[10] Del Giudice, F., D’Avino, G., Greco, F., Netti, P.A. and Maffettone, P.L., 2015. Effect of fluid rheology on particle migration in a square-shaped microchannel. *Microfluidics and Nanofluidics*, **19**(1), pp.95-104.

[11] Del Giudice, F., Sathish, S., D'Avino, G. and Shen, A.Q., 2017. "From the edge to the center": viscoelastic migration of particles and cells in a strongly shear-thinning liquid flowing in a microchannel. *Analytical Chemistry*, **89**(24), pp.13146-13159.

[12] Di Carlo, D., 2009. Inertial microfluidics. *Lab on a Chip*, **9**(21), pp.3038-3046.

[13] Di Carlo, D., Edd, J.F., Humphry, K.J., Stone, H.A. and Toner, M., 2009. Particle segregation and dynamics in confined flows. *Physical Review Letters*, **102**(9), p.094503.

[14] Gauthier, F., Goldsmith, H.L. and Mason, S.G., 1971. Particle motions in non-Newtonian media. *Rheologica Acta*, **10**(3), pp.344-364.

[15] Gauthier, F., Goldsmith, H.L. and Mason, S.G., 1971. Particle motions in non-Newtonian media. II. Poiseuille flow. *Transactions of the Society of Rheology*, **15**(2), pp.297-330.

[16] Hejazian, M., Li, W. and Nguyen, N.T., 2015. Lab on a chip for continuous-flow magnetic cell separation. *Lab on a Chip*, **15**(4), pp.959-970.

[17] Ho, B.P. and Leal, L.G., 1974. Inertial migration of rigid spheres in two-dimensional unidirectional flows. *Journal of Fluid Mechanics*, **65**(2), pp.365-400.

[18] Ho, B.P. and Leal, L.G., 1976. Migration of rigid spheres in a two-dimensional unidirectional shear flow of a second-order fluid. *Journal of Fluid Mechanics*, **76**(4), pp.783-799.

[19] Huang, L., Bian, S., Cheng, Y., Shi, G., Liu, P., Ye, X. and Wang, W., 2017. Microfluidics cell sample preparation for analysis: Advances in efficient cell enrichment and precise single cell capture. *Biomicrofluidics*, **11**(1), p.011501.

[20] Huang, P.Y. and Joseph, D.D., 2000. Effects of shear thinning on migration of neutrally buoyant particles in pressure driven flow of Newtonian and viscoelastic fluids. *Journal of Non-Newtonian Fluid Mechanics*, **90**(2-3), pp.159-185.

[21] James, D.F., 2009. Boger fluids. *Annual Review of Fluid Mechanics*, **41**, pp.129-142.

[22] Japper-Jaafar, A., Escudier, M.P. and Poole, R.J., 2010. Laminar, transitional and turbulent annular flow of drag-reducing polymer solutions. *Journal of Non-Newtonian Fluid Mechanics*, **165**(19-20), pp.1357-1372.

[23] Kang, K., Lee, S.S., Hyun, K., Lee, S.J. and Kim, J.M., 2013. DNA-based highly tunable particle focuser. *Nature Communications*, **4**, p.2567.

[24] Karimi, A., Yazdi, S. and Ardekani, A.M., 2013. Hydrodynamic mechanisms of cell and particle trapping in microfluidics. *Biomicrofluidics*, 7(2), p.021501.

[25] Karnis, A., Goldsmith, H.L. and Mason, S.G., 1963. Axial migration of particles in Poiseuille flow. *Nature*, **200**(4902), p.159.

[26] Karnis, A. and Mason, S.G., 1966. Particle motions in sheared suspensions. XIX. Viscoelastic media. *Transactions of the Society of Rheology*, **10**(2), pp.571-592.

[27] Kayani, A.A., Khoshmanesh, K., Ward, S.A., Mitchell, A. and Kalantar-zadeh, K., 2012. Optofluidics incorporating actively controlled micro-and nano-particles. *Biomicrofluidics*, **6**(3), p.031501.

[28] Kim, B. and Kim, J.M., 2016. Elasto-inertial particle focusing under the viscoelastic flow of DNA solution in a square channel. *Biomicrofluidics*, **10**(2), p.024111.

[29] Laurell, T., Petersson, F. and Nilsson, A., 2007. Chip integrated strategies for acoustic separation and manipulation of cells and particles. *Chemical Society Reviews*, **36**(3), pp.492-506.

[30] Leal, L.G., 1979. The motion of small particles in non-Newtonian fluids. *Journal of Non-Newtonian Fluid Mechanics*, **5**, pp.33-78.

[31] Leal, L.G., 1980. Particle motions in a viscous fluid. *Annual Review of Fluid Mechanics*, **12**(1), pp.435-476.

[32] Lee, D.J., Brenner, H., Youn, J.R. and Song, Y.S., 2013. Multiplex particle focusing via hydrodynamic force in viscoelastic fluids. *Scientific Reports*, **3**, p.3258.

[33] Leshansky, A.M., Bransky, A., Korin, N. and Dinnar, U., 2007. Tunable nonlinear viscoelastic “focusing” in a microfluidic device. *Physical Review Letters*, **98**(23), p.234501.

[34] Li, M., Li, W.H., Zhang, J., Alici, G. and Wen, W., 2014. A review of microfabrication techniques and dielectrophoretic microdevices for particle manipulation and separation. *Journal of Physics D: Applied Physics*, **47**(6), p.063001.

[35] Li, D., Lu, X. and Xuan, X., 2016. Viscoelastic separation of particles by size in straight rectangular microchannels: a parametric study for a refined understanding. *Analytical Chemistry*, **88**(24), pp.12303-12309.

[36] Li, G., McKinley, G.H. and Ardekani, A.M., 2015. Dynamics of particle migration in channel flow of viscoelastic fluids. *Journal of Fluid Mechanics*, **785**, pp.486-505.

[37] Liang, L., Zhu, J. and Xuan, X., 2011. Three-dimensional diamagnetic particle deflection in ferrofluid microchannel flows. *Biomicrofluidics*, **5**(3), p.034110.

[38] Lim, E.J., Ober, T.J., Edd, J.F., Desai, S.P., Neal, D., Bong, K.W., Doyle, P.S., McKinley, G.H. and Toner, M., 2014. Inertio-elastic focusing of bioparticles in microchannels at high throughput. *Nature Communications*, **5**, p.4120.

[39] Lim, H., Nam, J. and Shin, S., 2014. Lateral migration of particles suspended in viscoelastic fluids in a microchannel flow. *Microfluidics and Nanofluidics*, **17**(4), pp.683-692.

[40] Liu, C., Xue, C., Chen, X., Shan, L., Tian, Y. and Hu, G., 2015. Size-based separation of particles and cells utilizing viscoelastic effects in straight microchannels. *Analytical Chemistry*, **87**(12), pp.6041-6048.

[41] Liu, C., Ding, B., Xue, C., Tian, Y., Hu, G. and Sun, J., 2016. Sheathless focusing and separation of diverse nanoparticles in viscoelastic solutions with minimized shear thinning. *Analytical Chemistry,* **88**(24), pp.12547-12553.

[42] Liu, C. and Hu, G., 2017. High-throughput particle manipulation based on hydrodynamic effects in microchannels. *Micromachines,* **8**(3), p.73.

[43] Liu, C., Hu, G., Jiang, X. and Sun, J., 2015. Inertial focusing of spherical particles in rectangular microchannels over a wide range of Reynolds numbers. *Lab on a Chip*, **15**(4), pp.1168-1177.

[44] Lu, X., Liu, C., Hu, G. and Xuan, X., 2017. Particle manipulations in non-Newtonian microfluidics: A review. *Journal of Colloid and Interface Science,* **500**, pp.182-201.

[45] Lu, X. and Xuan, X., 2015. Continuous microfluidic particle separation via elasto-inertial pinched flow fractionation. *Analytical Chemistry*, **87**(12), pp.6389-6396.

[46] Lu, X., Zhu, L., Hua, R.M. and Xuan, X., 2015. Continuous sheath-free separation of particles by shape in viscoelastic fluids. *Applied Physics Letters,* **107**(26), p.264102.

[47] Martel, J.M. and Toner, M., 2014. Inertial focusing in microfluidics. *Annual Review of Biomedical Engineering*, **16**, pp.371-396.

[48] Nam, J., Lee, Y. and Shin, S., 2011. Size-dependent microparticles separation through standing surface acoustic waves. *Microfluidics and Nanofluidics*, **11**(3), pp.317-326.

[49] Nam, J., Tan, J.K.S., Khoo, B.L., Namgung, B., Leo, H.L., Lim, C.T. and Kim, S., 2015. Hybrid capillary-inserted microfluidic device for sheathless particle focusing and separation in viscoelastic flow. *Biomicrofluidics*, **9**(6), p.064117.

[50] Nilsson, J., Evander, M., Hammarström, B. and Laurell, T., 2009. Review of cell and particle trapping in microfluidic systems. *Analytica Chimica Acta*, **649**(2), pp.141-157.

[51] Poole, R.J. and Escudier, M.P., 2004. Turbulent flow of viscoelastic liquids through an axisymmetric sudden expansion. *Journal of Non-Newtonian Fluid Mechanics*, **117**(1), pp.25-46.

[52] Rodd, L.E., Scott, T.P., Boger, D.V., Cooper-White, J.J. and McKinley, G.H., 2005. The inertio-elastic planar entry flow of low-viscosity elastic fluids in micro-fabricated geometries. *Journal of Non-Newtonian Fluid Mechanics*, **129**(1), pp.1-22.

[53] Romeo, G., D'Avino, G., Greco, F., Netti, P.A. and Maffettone, P.L., 2013. Viscoelastic flow-focusing in microchannels: scaling properties of the particle radial distributions. *Lab on a Chip*, **13**(14), pp.2802-2807.

[54] Sajeesh, P. and Sen, A.K., 2014. Particle separation and sorting in microfluidic devices: a review. *Microfluidics and Nanofluidics*, **17**(1), pp.1-52.

[55] Seo, K.W., Byeon, H.J., Huh, H.K. and Lee, S.J., 2014. Particle migration and single-line particle focusing in microscale pipe flow of viscoelastic fluids. *RSC Advances*, **4**(7), pp.3512-3520.

[56] Seo, K.W., Kang, Y.J. and Lee, S.J., 2014. Lateral migration and focusing of microspheres in a microchannel flow of viscoelastic fluids. *Physics of Fluids*, **26**(6), p.063301.

[57] Won Seo, K., Ran Ha, Y. and Joon Lee, S., 2014. Vertical focusing and cell ordering in a microchannel via viscoelasticity: Applications for cell monitoring using a digital holographic microscopy. *Applied Physics Letters*, **104**(21), p.213702.

[58] Segre, G. and Silberberg, A., 1961. Radial particle displacements in Poiseuille flow of suspensions. *Nature*, **189**(4760), p.209.

[59] Song, H.Y., Lee, S.H., Salehiyan, R. and Hyun, K., 2016. Relationship between particle focusing and dimensionless numbers in elasto-inertial focusing. *Rheologica Acta*, **55**(11-12), pp.889-900.

[60] Tarn, M.D., Lopez-Martinez, M.J. and Pamme, N., 2014. On-chip processing of particles and cells via multilaminar flow streams. *Analytical and Bioanalytical Chemistry*, **406**(1), pp.139-161.

[61] Villone, M.M., D’avino, G., Hulsen, M.A., Greco, F. and Maffettone, P.L., 2013. Particle motion in square channel flow of a viscoelastic liquid: Migration vs. secondary flows. *Journal of Non-Newtonian Fluid Mechanics*, **195**, pp.1-8.

[62] Xiang, N., Dai, Q. and Ni, Z., 2016. Multi-train elasto-inertial particle focusing in straight microfluidic channels. *Applied Physics Letters*, **109**(13), p.134101.

[63] Xiang, N., Zhang, X., Dai, Q., Cheng, J., Chen, K. and Ni, Z., 2016. Fundamentals of elasto-inertial particle focusing in curved microfluidic channels. *Lab on a Chip*, **16**(14), pp.2626-2635.

[64] Xuan, X., Zhu, J. and Church, C., 2010. Particle focusing in microfluidic devices. *Microfluidics and Nanofluidics*, **9**(1), pp.1-16.

[65] Yan, S., Zhang, J., Yuan, D. and Li, W., 2017. Hybrid microfluidics combined with active and passive approaches for continuous cell separation. *Electrophoresis*, **38**(2), pp.238-249.

[66] Yang, S., Kim, J.Y., Lee, S.J., Lee, S.S. and Kim, J.M., 2011. Sheathless elasto-inertial particle focusing and continuous separation in a straight rectangular microchannel. *Lab on a Chip*, **11**(2), pp.266-273.

[67] Yang, S., Lee, S.S., Ahn, S.W., Kang, K., Shim, W., Lee, G., Hyun, K. and Kim, J.M., 2012. Deformability-selective particle entrainment and separation in a rectangular microchannel using medium viscoelasticity. *Soft Matter*, **8**(18), pp.5011-5019.

[68] Yasuda, K.Y., Armstrong, R.C. and Cohen, R.E., 1981. Shear flow properties of concentrated solutions of linear and star branched polystyrenes. *Rheologica Acta*, **20**(2), pp.163-178.

[69] Yuan, D., Zhang, J., Yan, S., Pan, C., Alici, G., Nguyen, N.T. and Li, W.H., 2015. Dean-flow-coupled elasto-inertial three-dimensional particle focusing under viscoelastic flow in a straight channel with asymmetrical expansion–contraction cavity arrays. *Biomicrofluidics*, **9**(4), p.044108.

[70] Yuan, D., Zhao, Q., Yan, S., Tang, S.Y., Alici, G., Zhang, J. and Li, W., 2018. Recent progress of particle migration in viscoelastic fluids. *Lab on a Chip*, **18**(4), pp.551-567.

[71] Zhang, J., Yan, S., Yuan, D., Alici, G., Nguyen, N.T., Warkiani, M.E. and Li, W., 2016. Fundamentals and applications of inertial microfluidics: A review. *Lab on a Chip*, **16**(1), pp.10-34.

CHAPTER THREE

VISCOELASTIC PARTICLE SEPARATION BY SIZE IN STRAIGHT RECTANGULAR MICROCHANNELS: A PARAMETRIC STUDY FOR A REFINED UNDERSTANDING

3.1 Abstract

Microfluidic separation of particles has been implemented using a variety of force fields. We demonstrate in this work a continuous sheath-free separation of both a binary and a ternary particle mixture in viscoelastic polymer solutions through straight rectangular microchannels. This label-free separation arises from the flow-induced lift force that directs particles towards size-sensitive focusing positions. It is found to be a strong function of multiple experimental parameters, which is systematically investigated in terms of dimensionless numbers. We propose to explain the observed shifting of particle focusing positions and transition from single to dual and triple equilibrium positions as a result of the competed center- (due to elasticity effects) and wall- (due to shear thinning effects) directed elastic lift forces. The inertial lift force comes into effect only at relatively high flow rates, which appears to reduce the separation efficiency and purity in our experiments.

3.2 Introduction

Separating targeted particles (either biological or synthetic) from a mixture in a continuous flow is important to many biological, chemical, and environmental applications. It has been implemented in microfluidic devices[1-5] by the use of a variety of force fields including acoustic,[6,7] electric,[8,9] hydrodynamic,[10,11] magnetic[12,13] and optical[14,15] etc. Among these forces, the flow-induced inertial lift in Newtonian fluids[16,17] has recently been extensively studied for high-throughput particle separations.[18,19] More recently, the hydrodynamic lift induced in non-Newtonian fluid flows has been demonstrated with the capability of manipulating particles with a much smaller size[20,21] and at a much higher throughput[22] than in Newtonian fluids. This force is often termed elasto-inertial lift due to its origin from both the fluid elasticity effects (as well as shear thinning effects if applicable) and the fluid inertial effects.[23-25] It has been exploited by several research groups to achieve the focusing of various types of particles in viscoelastic fluids through straight cylindrical[26-28] or rectangular[29-32] microchannels. It has also been combined with the Dean flow to realize the single-line focusing of particles in curved microchannels.[33-36] Such two- or three-dimensional focusing effects have been utilized to align cells in planar microchannels for enhanced detection and analysis.[37-39]

Continuous-flow particle separation in viscoelastic fluids has been implemented in conjunction with a sheath flow focusing, where the particle-free sheath fluid can be either Newtonian or non-Newtonian. In the former case, larger particles migrate across the interface of the non-Newtonian particle solution and the Newtonian sheath fluid, leaving smaller particles restrained in the non-Newtonian solution[40] due to the particle-size dependent elastic lift.[41] For the case with a non-Newtonian sheath fluid, particles have been observed to migrate towards both size[42-45] and shape[46] dependent lateral positions, which makes it possible to separate a mixture of two or more types of particles.[47] Sheath-free particle separation has also been demonstrated in viscoelastic fluid flows through both bifurcating and straight microchannels. In a bifurcating channel, particles are elasto-inertially focused to the center of the cylindrical[48,49] or slit-like[50] main-branch, and then displaced away from the sidewall of each rectangular side-branch at a particle-size dependent rate. In a simple straight square microchannel, large particles can be selectively enriched and filtered from a binary particle mixture[51] due to the single-line elasto-inertial particle focusing effect.[52] In a similar-shaped microchannel, fresh deformable red blood cells are found to be directed towards the centerline by the fluid elasticity-induced lift while more rigid white blood cells and fixed red blood cells are both entrained at the corners under a negligible fluid inertia.[53]

Very recently particles have been observed to migrate towards both size[54] and shape[55] dependent equilibrium positions in viscoelastic fluids through straight rectangular microchannels with a high width/height ratio. Each of these differential focusing phenomena can yield a continuous particle separation with a high efficiency and a high purity. However, a comprehensive understanding of the important factors that affect the size-based sheathless particle separation in viscoelastic fluids is still lacking. Moreover, this size-based separation has been demonstrated for only a binary mixture of particles with a size ratio of 3 and higher.[54] We present in this work a systematic experimental study of multiple parametric effects on the binary separation for a refined understanding of the underlying particle migration and focusing mechanism. Moreover, we demonstrate a sheathless viscoelastic separation of a ternary mixture of particle with close sizes, which can potentially be further extended to a heterogeneous particle mixture.

3.3 Experiment

Three sizes of spherical polystyrene particles with diameters of 3 µm, 5 µm and 10 µm (Sigma-Aldrich), respectively, were used for the binary and ternary separation experiments. They were mixed and re-suspended in water or aqueous polymer solutions to a final concentration of 106-107 particles per milliliter each. Tween 20 (Fisher Scientific) was added to all suspensions at 0.5% (v/v) to suppress particle aggregations and adhesions to channel walls. Three types of polymers, polyethylene oxide (PEO, molecular weight Mw = 2×10^6 Da, Sigma-Aldrich), polyacrylamide (PAA, Mw = 18×10^6 Da, Polysciences) and Polyvinylpyrrolidone (PVP, Mw = 0.36×10^6 Da, Sigma-Aldrich), were each dissolved in water (Fisher Scientific) to make polymer solutions of different concentrations. Specifically, PEO solutions were prepared at three different concentrations, 500 ppm, 1000 ppm and 2000 ppm. The 1000 ppm PEO solution was also mixed with glycerol at two different weight percentages, 15 % and 45%, to vary the solvent viscosity. The PVP solution was prepared at 8% (weight percentage) and the PAA solution was at 50 ppm. The rheology properties of these polymer solutions are summarized in Table 3.1. They were either obtained from experimental measurements that were reported in previous papers or calculated from empirical formulae. The details are provided in the Appendix A.

Table 3.1. Rheology properties of the prepared polymer solutions at 20 °C

Properties	PEO concentration (c, ppm)			PEO/glycerol (wt. %)		PVP (wt. %)	PAA (ppm)
	500	1000	2000	15	45	8	50
Density ρ (g/cm^3)	1.0	1.0	1.0	1.03	1.10	1.05	1.0
Zero-shear viscosity η_0 (mPa·s)	1.8	2.3	4.1	2.96	9.03	140	1.8
Effective relaxation time λ_e (ms)	4.3	6.8	10.6	11.0	24.0	2.3	10

Straight rectangular microchannels were fabricated with polydimethylsiloxane (PDMS) using the standard soft lithography technique described elsewhere.[56] They are each 20 mm long, 50 µm wide and have three different heights: 15 µm, 25 µm and 40 µm. The outlet of each microchannel is connected with a 900 µm wide, 2 mm long expansion for enhanced particle separation and visualization. Particle solution was infused in a 100 µL glass syringe (SGE Analytical Science) and driven through microchannels by a syringe pump (KD Scientific). Particle motion was visualized through an inverted microscope (Nikon Eclipse TE2000U, Nikon Instruments) with a CCD camera (Nikon DS-Qi1Mc). Videos were recorded at a frame rate of 20 images per second with an exposure time of 1 ms. Superimposed images were produced by stacking the sequential images in a 30 s video at an interval of 10 frames using the Nikon imaging software (NIS-Elements). This treatment was to ensure particles of different sizes can be easily identified. The particle center positions in the channel expansion, which were obtained using the "Analyze Particles" function in ImageJ software (National Institute of Health), were used to plot the probability distribution function (PDF) in Excel (Microsoft).

3.4 Theory

3.4.1 Mechanism of particle separation

As shown schematically in Fig. 3.1, a particle experiences both elastic and inertial lift forces in a viscoelastic fluid flow through a straight rectangular microchannel. The elastic lift, $\mathbf{F}_{eL}$, is generated by the non-uniform normal stress difference.[57-59] There are two normal stress differences, where the first normal stress difference, $\mathbf{N}_1$, creates an extra tension along the streamlines and the second normal stress difference,[60] $\mathbf{N}_2$, produces a secondary flow over the channel cross-section.[61] Considering the magnitude of $\mathbf{N}_2$ is usually much smaller than that of $\mathbf{N}_1$, we assume $\mathbf{F}_{eL}$ is proportional to the variation of $\mathbf{N}_1$ over the size of the particle,[29,55]

$$\mathbf{F}_{eL} \sim a^3 \nabla \mathbf{N}_1 \sim a^3 Wi \dot{\gamma}^2 \sim \lambda_e (a/w)^3 Q^3 \tag{3-1}$$

where a is the (equivalent) spherical diameter of the particle. This transverse elastic force directs the particle towards the low shear rate regions, i.e., the centerline and corners of the microchannel (see the contour of $\dot{\gamma}$ in the right panel of Fig. 3.1, where the darker color indicates a larger shear rate).

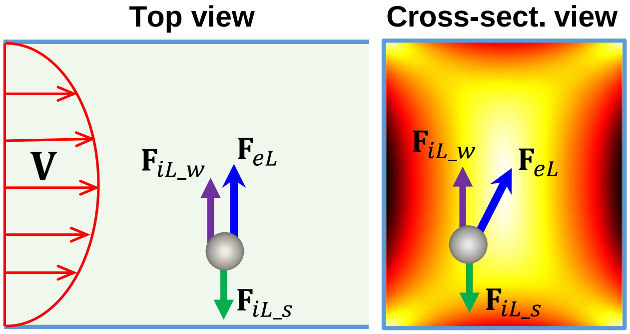

Fig. 3.1. Force analysis on a particle in a viscoelastic fluid flow through a straight rectangular microchannel: the fluid elasticity-induced lift, $\mathbf{F}_{eL}$, directs the particle towards the channel center and four corners where the fluid shear rate is the lowest; the wall-induced inertial lift, $\mathbf{F}_{iL\_w}$, and the shear gradient-induced inertial lift, $\mathbf{F}_{iL\_s}$, direct the particle towards the channel center and wall, respectively. The parabolic profile of fluid velocity, **V**, is illustrated in the top view of the microchannel (left panel). The contour of fluid shear rate is indicated by the color in the cross-sectional view (right panel, the darker the larger).

The inertial lift force is usually broken down into two parts: the wall-induced lift, $\mathbf{F}_{iL\_w}$, is a result of the pressure increase between a particle and its adjacent channel wall, which pushes the particle away from the wall; the shear gradient-induced inertial lift, $\mathbf{F}_{iL\_s}$, is a result of the curvature of the velocity profile in Poiseuille flow, which directs the particle towards the high shear rate regions, i.e., the channel walls (see the contour of $\dot{\gamma}$ in the right panel of Fig. 3.1). The total inertial lift, $\mathbf{F}_{iL}$, exerted on a particle is given by,[17-19,55]

$$\mathbf{F}_{iL} = \mathbf{F}_{iL\_w} + \mathbf{F}_{iL\_s} \sim \rho V^2 a^4/w^2 \sim \rho (a/w)^4 Q^2 \tag{3-2}$$

As the elastic lift, $\mathbf{F}_{eL}$ and the inertial lift, $\mathbf{F}_{iL}$, scale differently with the (equivalent) spherical diameter, particles with dissimilar sizes are focused to distinct equilibrium positions enabling a continuous sheath-free high-efficiency separation.[54,55] Moreover, the relaxation time (which depends on the polymer type/concentration and affects Wi and El), fluid flow rate (which affects Re as well as Wi), and channel dimensions (which affect AR as well as Re and Wi), can each be varied to change $\mathbf{F}_{iL}$ and/or $\mathbf{F}_{eL}$ and hence tune the equilibrium particle positions for an enhanced viscoelastic separation.

3.4.2 Dimensionless numbers

Four dimensionless numbers are used to characterize the fluid and particle dynamics in viscoelastic flows through straight rectangular microchannels. The (channel) Reynolds number, Re, compares the inertial force to viscous force,

$$Re = \frac{\rho V D_h}{\eta_0} = \frac{2\rho Q}{\eta_0 (w+h)} \tag{3-3}$$

where ρ is the fluid density, V is the average fluid velocity, $D_h = 2wh/(w+h)$ is the hydraulic diameter for a rectangular microchannel of width w and height h, η_0 is the zero-shear fluid viscosity, and Q is the volumetric flow rate. The Weissenberg number, Wi, compares the elastic force to viscous force,

$$Wi = \lambda_e \dot{\gamma} = \lambda_e \frac{2V}{w} = \frac{2\lambda_e Q}{w^2 h} \tag{3-4}$$

where λ_e is the effective relaxation time of the fluid (see Table 3.1), and $\dot{\gamma}$ is the average fluid shear rate in the width direction of the microchannel. The elasticity number, El, is the ratio of the Weissenberg number to Reynolds umber,

$$El = \frac{Wi}{Re} = \frac{\lambda_e \eta_0 (w+h)}{\rho w^2 h} \tag{3-5}$$

which compares the elastic force to inertial force and is independent of the flow kinematics. The channel aspect ratio, AR, is defined as the ratio of the channel width to height,

$$AR = w/h \tag{3-6}$$

3.5 Results and discussion

3.5.1 Binary particle separation

Fig. 3.2 demonstrates the viscoelastic separation of 5 μm- and 10 μm-diameter spherical particles in 1000 ppm PEO solution through a straight rectangular microchannel. The channel is 50 μm wide and 25 μm high with an aspect ratio of $AR = 2.0$. The volume flow rate is 250 μl/h, at which $Re = 0.81$ and $Wi = 15.1$. The snapshot image at the channel inlet (Fig. 3.2, left) shows a uniform distribution of the binary particle mixture. The superimposed image at the channel expansion (Fig. 3.2, right) indicates the formation of four distinct tight particle streams that are symmetric with respect to the channel centerline. The two outer streams are 10 μm particles and each about 1/3 of the channel half-width away from the sidewalls. The two inner streams are 5 μm particles and each off the channel center by 1/3 of the channel half-width. Hence, if a trifurcation is designed to follow the channel expansion such that the inner and outer halves of the solution flow into the central and side branches, respectively, the separation efficiency and purity can both achieve 100% for each type of particles.

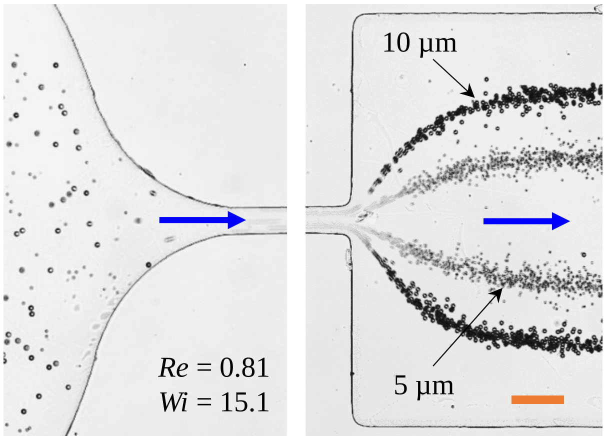

Fig. 3.2. Conitunuous separation of 5 µm- and 10 µm-diameter spherical particles in 1000 ppm PEO solution through a straight 50 µm-wide and 25 µm-high rectangular microchannel at the flow rate of 250 µL/h: (left) snapshot image at the channel inlet and (right) superimposed image at the channel expansion. The block arrows indicate the flow direction.

The observation that the focusing positions of larger particles are further away from the channel center in Fig. 3.2 is consistent with that reported by Liu et al.[54] It is also consistent with our earlier work,[55] where non-spherical particles were observed to migrate further outward than equal-volumed spherical particles in 1000 ppm PEO solution due to the larger dimension of their long axis. Previous studies have indicated that the inertial lift, $\mathbf{F}_{iL}$, focuses particles towards the center-plane of a microchannel with $AR = 2.0$ if the particle Reynolds number, $Re_p = Re(a/D_h)^2$, grows to the order of 1.[16-19] However, as

$Re < 1$ in the current experiment, at which $Re_p < 0.1$ for even 10 µm particles, it should be primarily the elastic lift, $\mathbf{F}_{eL}$, that creates the off-center particle focusing in Fig. 3.2. To explain this phenomenon, we propose that analogous to $\mathbf{F}_{iL}$, $\mathbf{F}_{eL}$ can also be broken down into two components where one points towards the channel center, $\mathbf{F}_{eL\rightarrow c}$ due to, for example, the viscoelastic effects,[29,57-59] and the other towards the wall, $\mathbf{F}_{eL\rightarrow w}$ due to, for example, shear-thinning effects.[28,59,62] Moreover, $\mathbf{F}_{eL\rightarrow w}$ is a stronger function of particle size than $\mathbf{F}_{eL\rightarrow c}$, which drives the off-center shift of the viscoelastic focusing positions of larger particles.

3.5.2 Effect of flow rate in terms of Re and Wi

Fig. 3.3 shows the flow rate effect on the separation of 5 µm and 10 µm particles in 1000 ppm PEO solution through a 25 µm-deep microchannel. The increase of flow rate, Q, raises the values of both Re and Wi (labeled on the cropped superimposed images in Fig. 3.3), leading to larger $\mathbf{F}_{iL}$ and $\mathbf{F}_{eL}$. At $Q = 50$ µl/h where $\mathbf{F}_{iL}$ is negligible with $Re = 0.16$, the majority of 5 µm particles are focused into a single band around the center of the microchannel (better viewed from the PDF plot in Fig. 3.3) due to the dominant impact of $\mathbf{F}_{eL\rightarrow c}$ over $\mathbf{F}_{eL\rightarrow w}$. In contrast, all 10 µm particles are focused into two tight streams that are each half-way of the channel radius (more accurately, channel half-width) due to the stronger dependence of $\mathbf{F}_{eL\rightarrow w}$ on particle size than $\mathbf{F}_{eL\rightarrow c}$ as noted above. With the increase of flow rate until $Q = 250$ µL/h, the single band of 5 µm particles is gradually split into two off-center streams that each shifts towards 1/3 of the channel half-width. Meanwhile, the dual streams of 10 µm particles still stay tight and each slowly shifts outward until 2/3 of the channel half-width. This trend, as viewed from both the particle images and PDF plots in Fig. 3.3, may be explained by the greater scaling of $\mathbf{F}_{eL\rightarrow w}$ with flow rate as compared to $\mathbf{F}_{eL\rightarrow c}$.

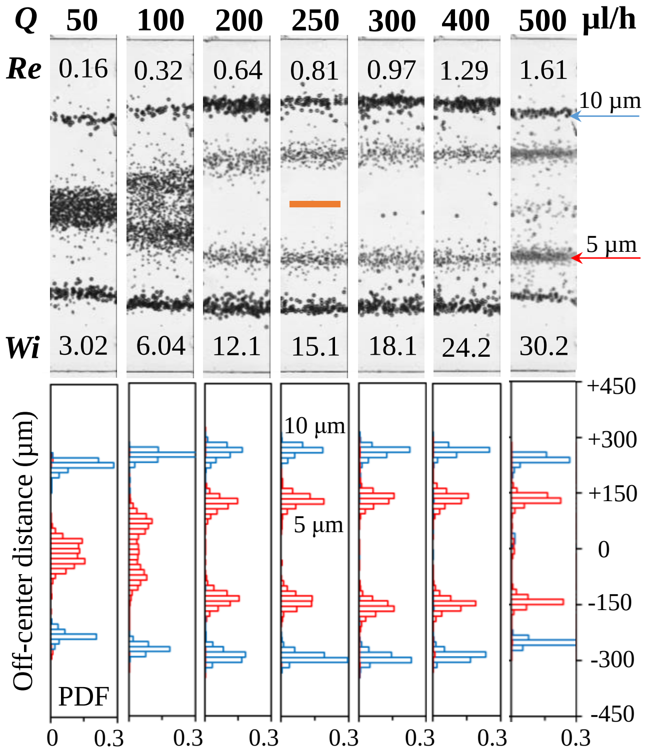

Fig. 3.3. Effects of flow rate (in terms of Re and Wi with values being labeled) on the separation of 5 μm and 10 μm particles in 1000 ppm PEO solution through a straight 50 μm-wide and 25 μm-high rectangular microchannel: (top) superimposed images (cropped) and (bottom) particle PDF plots at the channel expansion. The scale bar represents 100 μm.

At $Q = 300$ μl/h where $Re = 0.97$, the focusing positions of both types of particles remain nearly unvaried though a very small number of 10 μm particles appear to travel along the channel center. This phenomenon may probably be a result of the action of $\mathbf{F}_{iL}$ that is a fourth-order function of particle size. Further increasing the flow rate until $Q =$ 500 μl/h, all the focused particle streams start shifting slowly inward due to the increasing role of $\mathbf{F}_{iL}$. Moreover, 5 µm particles also re-appear in the channel center along with 10 µm particles due to the effect of $\mathbf{F}_{iL}$. This transition from single to dual to triple equilibrium positions for viscoelastic particle focusing is consistent with the observation in our previous study.[55] It is a result of the competition between the two components of elastic lift, $\mathbf{F}_{eL\to c}$ and $\mathbf{F}_{eL\to w}$, at $Q < 300$ µL/h with $Re < 1$, and the competition between the elastic and inertial lifts, $\mathbf{F}_{eL}$ and $\mathbf{F}_{iL}$, at higher flow rate with $Re \geq 1$. The best separation is achieved at around $Q = 250$ µL/h, which, as viewed from the superimposed images and PDF plots in Fig. 3.3, lies in the former regime.

3.5.3 Effect of PEO concentration in terms of El

Fig. 3.4 shows the PEO concentration effect on the viscoelastic separation of 5 µm and 10 µm particles in a 25 µm-deep microchannel under three different flow rates: Q = 50, 250 and 500 µl/h. Both particle images and 3D plots for particle PDF at the channel expansion are used for the demonstration. The particle images at other flow rates are shown in Fig A-1 of Appendix A. In 0 ppm PEO solution (i.e., water) without elasticity, no separation is observed because, as noted above, the two types of particles are both (weakly) focused by $\mathbf{F}_{iL}$ towards the channel centerline in the range of the tested flow rates. Note that further increasing the flow rate (to even $Re_p{\sim}1$) won't make the separation happen because the inertial focusing position is along the centerline of the longer side, which is the width in our tested channel, for both types of particles.[16-19,63,64]

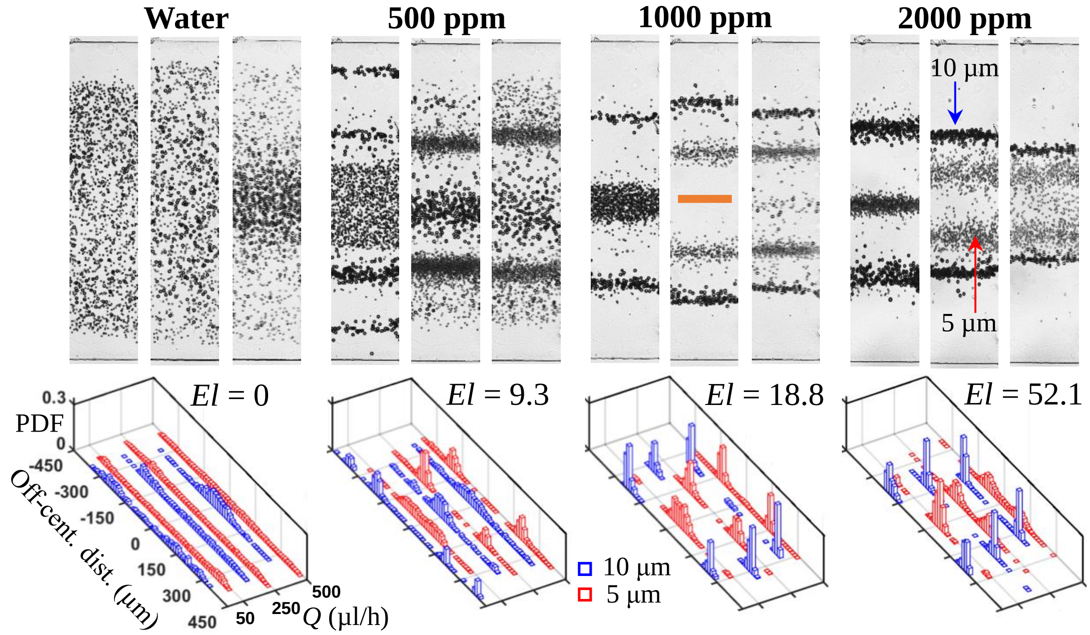

Fig. 3.4. Effects of PEO concentration (in terms of El with values being labeled) on the viscoelastic separation of 5 μm and 10 μm particles through a straight 50 μm-wide and 25 μm-high rectangular microchannel: (top) superimposed images (cropped) at flow rates of 50, 250 and 500 μl/h from left to right and (bottom) 3D plots of particle PDF at the channel expansion. The scale bar represents 100 μm.

Increasing the concentration of PEO raises Wi and reduces Re due to the increased relaxation time and fluid viscosity (see Table 3.1), respectively, leading to a greater El or equivalently an enhanced contribution of $\mathbf{F}_{eL}$. In 500 ppm PEO solution, the viscoelastic focusing is apparently weaker than in 1000 ppm for both 5 μm and 10 μm particles. Interestingly, 10 μm particles seem to have four equilibrium positions at $Q = 50$ μl/h, where two are still half-way to the channel centerline like those in 1000 ppm PEO while the other two are each about 1/6 of the channel half-width away from the sidewall. The mechanism behind this observation is currently unclear. In addition, 10 μm particles start being focused towards the channel center at a lower flow rate than in 1000 ppm PEO (see the particle images at other flows in Figure A-2 of Appendix A). This phenomenon is speculated to result from the stronger dependence of $\mathbf{F}_{eL\rightarrow c}$ on fluid elasticity than of $\mathbf{F}_{eL\rightarrow w}$. It may also be partially due to the weakened contribution of $\mathbf{F}_{eL}$ in 500 ppm PEO such that the effects of $\mathbf{F}_{iL}$ grow. The enhanced fluid elasticity in 2000 ppm PEO solution further shifts the elastic particle focusing positions inward due to the larger role of $\mathbf{F}_{eL\rightarrow c}$ than of $\mathbf{F}_{eL\rightarrow w}$. However, the occurrence of 10 µm particles along the channel center in 2000 ppm PEO is delayed as compared to 1000 ppm PEO solution. This may be due to the reduced role of $\mathbf{F}_{iL}$ in 2000 ppm PEO with a larger El, which is opposite to that in 500 ppm with a smaller El as noted above.

3.5.4 Effect of solvent viscosity in terms of El

Fig. 3.5 shows the solvent viscosity effect on the viscoelastic separation of 5 µm and 10 µm particles in 1000 ppm PEO solution through a 25 µm-deep microchannel under different flow rates. Adding glycerol into the PEO solution increases its viscosity as well as relaxation time, which causes similar variations in Re and Wi to those at a higher PEO concentration. A similar shifting of particle focusing positions towards the channel centerline is thus expected, which is illustrated in Fig. 3.5 when the glycerol content is increased from 15 to 40 wt. %. However, this inward shifting is not obvious when 15 wt. % glycerol is added to the pure PEO solution (refer to the images in Fig. 3.3). In addition, the particle focusing positions in each of these PEO/glycerol solutions undergo a similar trend to those in the pure PEO solution when the flow rate is increased, i.e., first move outward due to the stronger action of $\mathbf{F}_{eL\rightarrow w}$ than $\mathbf{F}_{eL\rightarrow c}$ at low flow rates and then move inward due to probably the increased contribution of $\mathbf{F}_{iL}$ as explained earlier.

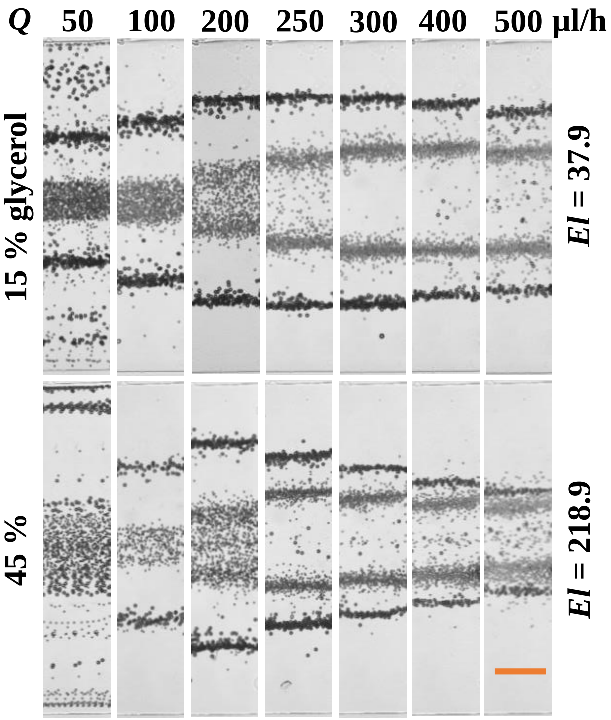

Fig. 3.5. Effects of solvent viscosity (in terms of El with values being labeled), which is varied by adding glycerol (wt. %) into 1000 ppm PEO solution, on the viscoelastic separation of 5 µm and 10 µm particles through a straight 50 µm-wide and 25 µm-high rectangular microchannel under a range of flow rates. The scale bar represents 100 µm.

3.5.5 Effect of polymer type in terms of El

Fig 3.6 compares the separations of 5 µm and 10 µm particles in three commonly used polymer solutions through a 25 µm-deep microchannel at a fixed flow rate of 250 µl/h. In 8 wt. % PVP solution, no separation takes place because both types of particles are focused into a single band around the centerline. This is attributed to the negligible shear thinning effects of this solution,[60] which produces a much weaker $\mathbf{F}_{eL\rightarrow w}$ than $\mathbf{F}_{eL\rightarrow c}$. However, a small number of 5 µm particles are observed to stay near the corners of the microchannel. This “secondary” equilibrium position, which has also been observed in our earlier studies and disappears at higher flow rates,[44,46,55] however, remains in the whole range of flow rates (up to 500 μl/h, more images are shown in Figure A-3 of Appendix A) in our tests. It may be because the corner-directed $\mathbf{F}_{eL}$ is too strong in the PVP solution with a very large value of $El = 368$. The absence of 10 μm particles near the channel corner is surprising if we consider the fact that $\mathbf{F}_{eL}$ increases with particle size and $\mathbf{F}_{iL}$ is negligible at $Re = 0.014$. In the 50 ppm PAA solution, no separation is observed either because both types of particles are still dispersed with very weak focusing effects. This phenomenon is believed to be correlated with the second normal stress difference in the PAA solution that has been demonstrated to generate a cross-stream secondary flow in rectangular microchannels.[45,61,65]

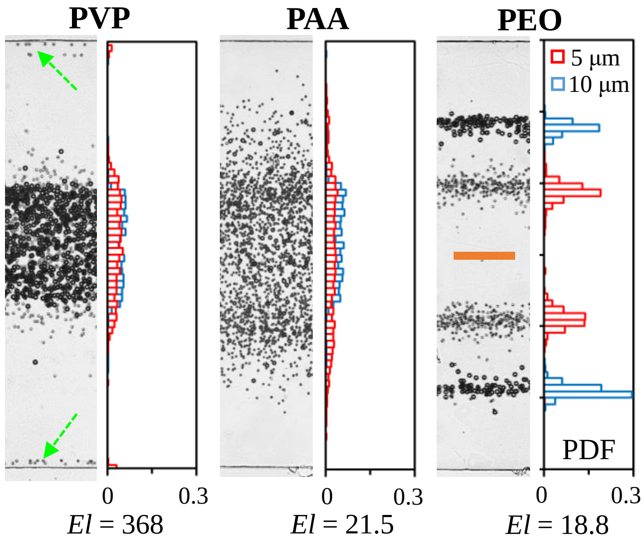

Fig. 3.6. Comparison of the binary separations of 5 μm and 10 μm particles in three commonly used polymer solutions (El values labeled) through a straight 50 μm-wide and 25 μm-high rectangular microchannel under a constant flow rate of 250 μl/h: the left and right halves of each panel show the cropped superimposed image and particle PDF plot at

the channel expansion, respectively. The two dashed-line arrows on the image of PVP solution highlight the equilibrium positions of 5 μm particles near the corner of the channel. The scale bar represents 100 μm.

3.5.6 *Effect of channel aspect ratio (AR)*

Fig. 3.7 shows the channel aspect ratio, AR, effect on the viscoelastic separation of 5 μm and 10 μm particles in 1000 ppm PEO solution at a constant flow rate of 250 μl/h . The experimental images for the other flow rates are shown in Fig. A-4 of Appendix A. The width of the rectangular microchannels is fixed at 50 μm while the height is varied from 15 μm to 25 μm and 40 μm, leading to a drop in both Re and Wi. In the 15 μm deep microchannel with $AR = 3.3$, three focusing positions are available for 10 μm particles, where one is along the channel centerline and the other two are each slightly within 1/3 of the channel half-width from the sidewalls. The number of focusing positions is reduced to two off the centerline in the 25 μm deep channel ($AR = 3.3$) and to one along the centerline in the 40 μm deep channel ($AR = 1.25$). As Re and Wi both decrease in a deeper microchannel, the observed change in viscoelastic focusing positions of 10 μm particles is thought to be related to the increased shear gradients in the channel width direction, which enhances $\mathbf{F}_{eL\to c}$ more than $\mathbf{F}_{eL\to w}$. This hypothesis also explains why the focusing positions of 5 μm particles move inward from two off-center at $AR = 3.3$ and 2.0 to one along the centerline at $AR = 1.25$. The observation of single center-focusing position for both types of particles in a nearly square microchannel is consistent with earlier studies.[44,51,52]

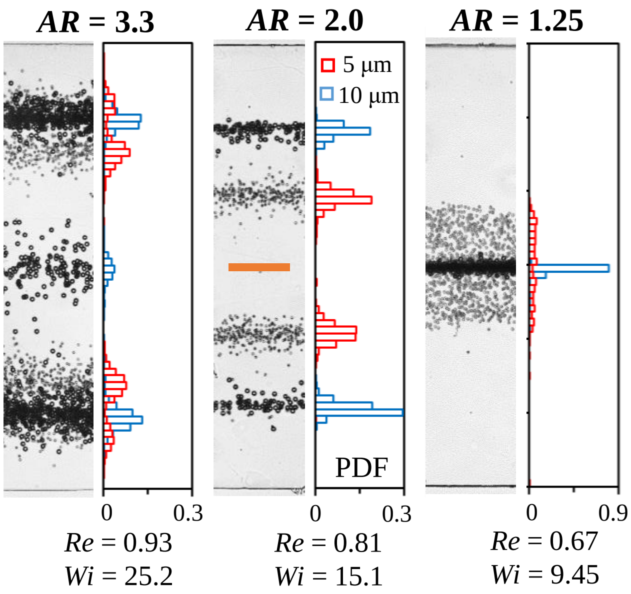

Fig. 3.7. Effects of channel aspect ratio, AR, on the viscoelastic separation of 5 µm and 10 µm particles through straight 50 µm-wide rectangular microchannels at a fixed flow rate of 250 µl/h: the left and right halves of each panel show the cropped superimposed image and particle PDF plot at the channel expansion, respectively. The scale bar represents 100 µm.

3.5.7 Ternary particle separation

Fig. 3.8 demonstrates a ternary separation of 3 µm, 5 µm and 10 µm particles in 1000 ppm PEO solution through a 25 µm deep microchannel at a flow rate of 300 µl/h. The particle images at other flow rates are shown in Fig. A-5 of Appendix A. Consistent with the binary separation in Fig. 3.3, both 5 and 10 µm particles have two off-center focusing positions that still remain at about 1/3 of the channel half-width away from the channel centerline and sidewalls, respectively. As $\mathbf{F}_{eL\rightarrow c}$ is a weaker function of particle size than $\mathbf{F}_{eL\rightarrow w}$, the smallest 3 µm particles in the mixture are mostly focused into a band around the centerline that has a slight overlapping with the 5 µm particle streams at its edges. We divided each channel half-width into three zones: inner zone within 120 µm from the centerline, intermediate zone within 120 to 230 µm from the centerline, and outer zone beyond 230 µm from the centerline. The separation efficiency (defined as the percentage of particle number inside a specific zone) and purity (defined as the ratio of the targeted particle number to the total particle number within a specific zone) of each type of particles in their respective preferred zones were calculated based on the experimental data of particle PDF in Fig. 3.8, and are presented in Table 3.2. The efficiency and purity of each particle type are 90% or better except for the purity of 3 µm particles. This is because the number of 5 µm particles (over 1550 counted) overwhelms the total of 3 µm (over 550 counted) and 10 µm (over 100 counted) particles in the video we analyzed. Consequently, a small percentage of 5 µm particles in the inner zone can significantly bring down the purity of 3 µm particles therein.

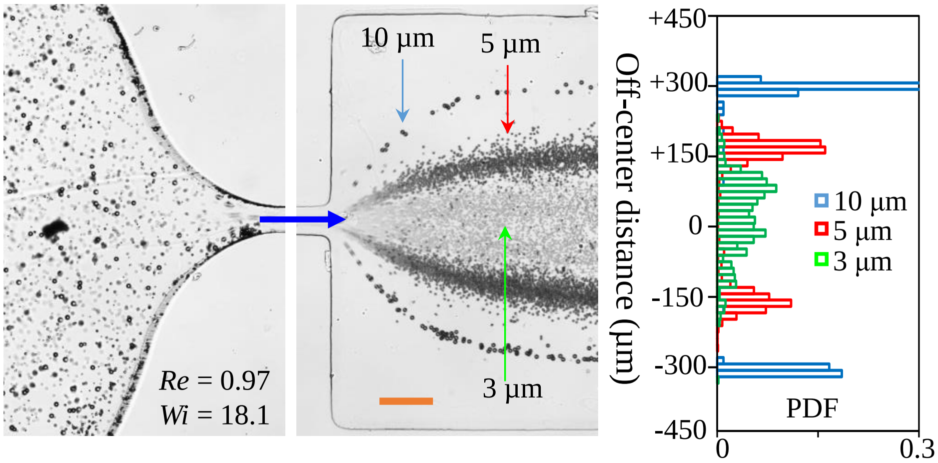

Fig. 3.8. Viscoelastic separation of 3 µm-, 5 µm-, and 10 µm-diameter spherical particles in 1000 ppm PEO solution through a straight 50 µm-wide and 25 µm-high rectangular microchannel at a flow rate of 250 µl/h: (left) snapshot image the channel inlet, (middle) superimposed images at the channel expansion, and (right) particle PDF at the channel expansion. The block arrow indicates the flow direction. The scale bar represents 100 µm.

Table 3.2. Efficiency and purity of the ternary particle separation shown in Fig. 3.8.

Particles	Preferred zone	Efficiency	Purity
10 µm	Outer	96.2%	95.2%
5 µm	Intermediate	92.2%	95.5%
3 µm	Inner	90.4%	82.5%

3.5.8 Summary of parametric effects on the elastic lift

Based on the above experimental results for the parametric effects on viscoelastic particle separation, we summarize in Table 3.3 the dependences of the two proposed components of elastic lift, $\mathbf{F}_{eL\rightarrow w}$ and $\mathbf{F}_{eL\rightarrow c}$, on multiple parameters in straight rectangular microchannels.

Table 3.3. Parametric dependences of the elastic lift in viscoelastic fluid flows through straight rectangular microchannels under a negligible to weak inertia (i.e., $Re < 1$). The last column shows the experimentally observed shifting of particle focusing positions with the increase of the corresponding experimental parameters.

Parameters	$\mathbf{F}_{eL\rightarrow w}$	$\mathbf{F}_{eL\rightarrow c}$	Shift towards
Particle size	stronger		wall
Flow rate	stronger		wall
Fluid elasticity		stronger	center
Channel depth		stronger	center

3.6 Conclusions

We have demonstrated continuous-flow sheath-free separations of both a binary 3 µm/5 µm and a ternary 3 µm/5 µm/10 µm particle mixture in 1000 ppm PEO solution through a straight 2 cm long, 50 µm-wide and 25 µm-high rectangular microchannel. This separation arises from the flow-induced viscoelastic focusing effect that directs particles towards size-sensitive equilibrium positions. We have also conducted a comprehensive experimental study of the effects of flow rate, solvent viscosity, polymer concentration, polymer type and channel aspect ratio on the binary particle separation in terms of four dimensionless numbers. To explain the observed shifting of particle focusing positions in this parametric study, we propose to break down the elastic lift into a center-directed component due to the fluid elasticity effects and a wall-directed component due to the fluid shear thinning effects. These two components of elastic lift scale differently with the experimental parameters, which work with the inertial lift to produce the differential viscoelastic or elasto-inertial particle focusing in straight rectangular microchannels. However, it is found that the inertial lift does not come into effect until the Reynolds number approaches 1. The results of the present study are anticipated to provide a useful guidance for future design and control of the elasto-inertial particle separation technique.

Acknowledgements This work was supported in part by NSF under grant CBET-1150670.

References

[1] Pamme, N., 2007. Continuous flow separations in microfluidic devices. *Lab on a Chip*, **7**(12), pp.1644-1659.

[2] Gossett, D.R., Weaver, W.M., Mach, A.J., Hur, S.C., Tse, H.T.K., Lee, W., Amini, H. and Di Carlo, D., 2010. Label-free cell separation and sorting in microfluidic systems. *Analytical and Bioanalytical Chemistry*, **397**(8), pp.3249-3267.

[3] Karimi, A., Yazdi, S. and Ardekani, A.M., 2013. Hydrodynamic mechanisms of cell and particle trapping in microfluidics. *Biomicrofluidics*, **7**(2), p.021501.

[4] Sajeesh, P. and Sen, A.K., 2014. Particle separation and sorting in microfluidic devices: a review. *Microfluidics and Nanofluidics*, **17**(1), pp.1-52.

[5] Shields IV, C.W., Reyes, C.D. and López, G.P., 2015. Microfluidic cell sorting: a review of the advances in the separation of cells from debulking to rare cell isolation. *Lab on a Chip*, **15**(5), pp.1230-1249.

[6] Laurell, T., Petersson, F. and Nilsson, A., 2007. Chip integrated strategies for acoustic separation and manipulation of cells and particles. *Chemical Society Reviews*, **36**(3), pp.492-506.

[7] Wang, Z. and Zhe, J., 2011. Recent advances in particle and droplet manipulation for lab-on-a-chip devices based on surface acoustic waves. *Lab on a Chip*, **11**(7), pp.1280-1285.

[8] Pethig, R., 2010. Dielectrophoresis: Status of the theory, technology, and applications. *Biomicrofluidics*, **4**(2), p.022811.

[9] Regtmeier, J., Eichhorn, R., Viefhues, M., Bogunovic, L. and Anselmetti, D., 2011. Electrodeless dielectrophoresis for bioanalysis: Theory, devices and applications. *Electrophoresis*, **32**(17), pp.2253-2273.

[10] Tsutsui, H. and Ho, C.M., 2009. Cell separation by non-inertial force fields in microfluidic systems. *Mechanics Research Communications*, **36**(1), pp.92-103.

[11] McGrath, J., Jimenez, M. and Bridle, H., 2014. Deterministic lateral displacement for particle separation: a review. *Lab on a Chip*, **14**(21), pp.4139-4158.

[12] Hejazian, M., Li, W. and Nguyen, N.T., 2015. Lab on a chip for continuous-flow magnetic cell separation. *Lab on a Chip*, **15**(4), pp.959-970.

[13] Zhao, W., Cheng, R., Miller, J.R. and Mao, L., 2016. Label-free microfluidic manipulation of particles and cells in magnetic liquids. *Advanced Functional Materials*, **26**(22), pp.3916-3932.

[14] Kim, S.B., Yoon, S.Y., Sung, H.J. and Kim, S.S., 2008. Cross-type optical particle separation in a microchannel. *Analytical Chemistry*, **80**(7), pp.2628-2630.

[15] Kayani, A.A., Khoshmanesh, K., Ward, S.A., Mitchell, A. and Kalantar-zadeh, K., 2012. Optofluidics incorporating actively controlled micro-and nano-particles. *Biomicrofluidics*, **6**(3), p.031501.

[16] Di Carlo, D., 2009. Inertial microfluidics. *Lab on a Chip*, **9**(21), pp.3038-3046.

[17] Martel, J.M. and Toner, M., 2014. Inertial focusing in microfluidics. *Annual Review of Biomedical Engineering*, **16**, pp.371-396.

[18] Amini, H., Lee, W. and Di Carlo, D., 2014. Inertial microfluidic physics. *Lab on a Chip*, **14**(15), pp.2739-2761.

[19] Zhang, J., Yan, S., Yuan, D., Alici, G., Nguyen, N.T., Warkiani, M.E. and Li, W., 2016. Fundamentals and applications of inertial microfluidics: A review. *Lab on a Chip*, **16**(1), pp.10-34.

[20] Kim, J.Y., Ahn, S.W., Lee, S.S. and Kim, J.M., 2012. Lateral migration and focusing of colloidal particles and DNA molecules under viscoelastic flow. *Lab on a Chip*, **12**(16), pp.2807-2814.

[21] De Santo, I., D'Avino, G., Romeo, G., Greco, F., Netti, P.A. and Maffettone, P.L., 2014. Microfluidic lagrangian trap for brownian particles: Three-dimensional focusing down to the nanoscale. *Physical Review Applied*, **2**(6), p.064001.

[22] Lim, E.J., Ober, T.J., Edd, J.F., Desai, S.P., Neal, D., Bong, K.W., Doyle, P.S., McKinley, G.H. and Toner, M., 2014. Inertio-elastic focusing of bioparticles in microchannels at high throughput. *Nature Communications,* **5**, p.4120.

[23] Trofa, M., Vocciante, M., D'Avino, G., Hulsen, M.A., Greco, F. and Maffettone, P.L., 2015. Numerical simulations of the competition between the effects of inertia and viscoelasticity on particle migration in Poiseuille flow. *Computers & Fluids*, **107**, pp.214-223.

[24] D'Avino, G. and Maffettone, P.L., 2015. Particle dynamics in viscoelastic liquids. *Journal of Non-Newtonian Fluid Mechanics,* **215**, pp.80-104.

[25] Kim, B. and Kim, J.M., 2016. Elasto-inertial particle focusing under the viscoelastic flow of DNA solution in a square channel. *Biomicrofluidics*, **10**(2), p.024111.

[26] D'Avino, G., Romeo, G., Villone, M.M., Greco, F., Netti, P.A. and Maffettone, P.L., 2012. Single line particle focusing induced by viscoelasticity of the suspending liquid: theory, experiments and simulations to design a micropipe flow-focuser. *Lab on a Chip*, **12**(9), pp.1638-1645.

[27] Romeo, G., D'Avino, G., Greco, F., Netti, P.A. and Maffettone, P.L., 2013. Viscoelastic flow-focusing in microchannels: scaling properties of the particle radial distributions. *Lab on a Chip*, **13**(14), pp.2802-2807.

[28] Seo, K.W., Byeon, H.J., Huh, H.K. and Lee, S.J., 2014. Particle migration and single-line particle focusing in microscale pipe flow of viscoelastic fluids. *RSC Advances*, **4**(7), pp.3512-3520.

[29] Leshansky, A.M., Bransky, A., Korin, N. and Dinnar, U., 2007. Tunable nonlinear viscoelastic "focusing" in a microfluidic device. *Physical Review Letters*, **98**(23), p.234501.

[30] Del Giudice, F., Romeo, G., D'Avino, G., Greco, F., Netti, P.A. and Maffettone, P.L., 2013. Particle alignment in a viscoelastic liquid flowing in a square-shaped microchannel. *Lab on a Chip*, **13**(21), pp.4263-4271.

[31] Seo, K.W., Kang, Y.J. and Lee, S.J., 2014. Lateral migration and focusing of microspheres in a microchannel flow of viscoelastic fluids. *Physics of Fluids*, **26**(6), p.063301.

[32] Del Giudice, F., D'Avino, G., Greco, F., Netti, P.A. and Maffettone, P.L., 2015. Effect of fluid rheology on particle migration in a square-shaped microchannel. *Microfluidics and Nanofluidics*, **19**(1), pp.95-104.

[33] Lee, D.J., Brenner, H., Youn, J.R. and Song, Y.S., 2013. Multiplex particle focusing via hydrodynamic force in viscoelastic fluids. *Scientific Reports*, **3**, p.3258.

[34] Cha, S., Kang, K., You, J.B., Im, S.G., Kim, Y. and Kim, J.M., 2014. Hoop stress-assisted three-dimensional particle focusing under viscoelastic flow. *Rheologica Acta*, **53**(12), pp.927-933.

[35] Yuan, D., Zhang, J., Yan, S., Pan, C., Alici, G., Nguyen, N.T. and Li, W.H., 2015. Dean-flow-coupled elasto-inertial three-dimensional particle focusing under viscoelastic flow in a straight channel with asymmetrical expansion–contraction cavity arrays. *Biomicrofluidics*, **9**(4), p.044108.

[36] Xiang, N., Zhang, X., Dai, Q., Cheng, J., Chen, K. and Ni, Z., 2016. Fundamentals of elasto-inertial particle focusing in curved microfluidic channels. *Lab on a Chip*, **16**(14), pp.2626-2635.

[37] Cha, S., Shin, T., Lee, S.S., Shim, W., Lee, G., Lee, S.J., Kim, Y. and Kim, J.M., 2012. Cell stretching measurement utilizing viscoelastic particle focusing. *Analytical Chemistry*, **84**(23), pp.10471-10477.

[38] Won Seo, K., Ran Ha, Y. and Joon Lee, S., 2014. Vertical focusing and cell ordering in a microchannel via viscoelasticity: Applications for cell monitoring using a digital holographic microscopy. *Applied Physics Letters*, **104**(21), p.213702.

[39] Bae, Y.B., Jang, H.K., Shin, T.H., Phukan, G., Tran, T.T., Lee, G., Hwang, W.R. and Kim, J.M., 2016. Microfluidic assessment of mechanical cell damage by extensional stress. *Lab on a Chip*, **16**(1), pp.96-103.

[40] Ha, B., Park, J., Destgeer, G., Jung, J.H. and Sung, H.J., 2016. Transfer of microparticles across laminar streams from non-Newtonian to Newtonian fluid. *Analytical Chemistry*, **88**(8), pp.4205-4210.

[41] Yuan, D., Zhang, J., Sluyter, R., Zhao, Q., Yan, S., Alici, G. and Li, W., 2016. Continuous plasma extraction under viscoelastic fluid in a straight channel with asymmetrical expansion–contraction cavity arrays. *Lab on a Chip*, **16**(20), pp.3919-3928.

[42] Wu, Z., Hjort, K., Wicher, G. and Svenningsen, Å.F., 2008. Microfluidic high viability neural cell separation using viscoelastically tuned hydrodynamic spreading. *Biomedical Microdevices*, **10**(5), pp.631-638.

[43] Nam, J., Lim, H., Kim, D., Jung, H. and Shin, S., 2012. Continuous separation of microparticles in a microfluidic channel via the elasto-inertial effect of non-Newtonian fluid. *Lab on a Chip*, **12**(7), pp.1347-1354.

[44] Lu, X. and Xuan, X., 2015. Continuous microfluidic particle separation via elasto-inertial pinched flow fractionation. *Analytical Chemistry*, **87**(12), pp.6389-6396.

[45] Lim, H., Nam, J. and Shin, S., 2014. Lateral migration of particles suspended in viscoelastic fluids in a microchannel flow. *Microfluidics and Nanofluidics*, **17**(4), pp.683-692.

[46] Lu, X. and Xuan, X., 2015. Elasto-inertial pinched flow fractionation for continuous shape-based particle separation. *Analytical Chemistry*, **87**(22), pp.11523-11530.

[47] Kang, K., Lee, S.S., Hyun, K., Lee, S.J. and Kim, J.M., 2013. DNA-based highly tunable particle focuser. *Nature Communications*, **4**, p.2567.

[48] Nam, J., Namgung, B., Lim, C.T., Bae, J.E., Leo, H.L., Cho, K.S. and Kim, S., 2015. Microfluidic device for sheathless particle focusing and separation using a viscoelastic fluid. *Journal of Chromatography A*, **1406**, pp.244-250.

[49] Nam, J., Tan, J.K.S., Khoo, B.L., Namgung, B., Leo, H.L., Lim, C.T. and Kim, S., 2015. Hybrid capillary-inserted microfluidic device for sheathless particle focusing and separation in viscoelastic flow. *Biomicrofluidics*, **9**(6), p.064117.

[50] Nam, J., Shin, Y., Tan, J.K.S., Lim, Y.B., Lim, C.T. and Kim, S., 2016. High-throughput malaria parasite separation using a viscoelastic fluid for ultrasensitive PCR detection. *Lab on a Chip*, **16**(11), pp.2086-2092.

[51] Yang, S., Kim, J.Y., Lee, S.J., Lee, S.S. and Kim, J.M., 2011. Sheathless elasto-inertial particle focusing and continuous separation in a straight rectangular microchannel. *Lab on a Chip*, **11**(2), pp.266-273.

[52] Ahn, S.W., Lee, S.S., Lee, S.J. and Kim, J.M., 2015. Microfluidic particle separator utilizing sheathless elasto-inertial focusing. *Chemical Engineering Science*, **126**, pp.237-243.

[53] Yang, S., Lee, S.S., Ahn, S.W., Kang, K., Shim, W., Lee, G., Hyun, K. and Kim, J.M., 2012. Deformability-selective particle entrainment and separation in a rectangular microchannel using medium viscoelasticity. *Soft Matter*, **8**(18), pp.5011-5019.

[54] Liu, C., Xue, C., Chen, X., Shan, L., Tian, Y. and Hu, G., 2015. Size-based separation of particles and cells utilizing viscoelastic effects in straight microchannels. *Analytical Chemistry*, **87**(12), pp.6041-6048.

[55] Lu, X., Zhu, L., Hua, R.M. and Xuan, X., 2015. Continuous sheath-free separation of particles by shape in viscoelastic fluids. *Applied Physics Letters*, **107**(26), p.264102.

[56] Li, D., Lu, X., Song, Y., Wang, J., Li, D. and Xuan, X., 2016. Sheathless electrokinetic particle separation in a bifurcating microchannel. *Biomicrofluidics*, **10**(5), p.054104.

[57] Ho, B.P. and Leal, L.G., 1976. Migration of rigid spheres in a two-dimensional unidirectional shear flow of a second-order fluid. *Journal of Fluid Mechanics*, **76**(4), pp.783-799.

[58] Huang, P.Y., Feng, J., Hu, H.H. and Joseph, D.D., 1997. Direct simulation of the motion of solid particles in Couette and Poiseuille flows of viscoelastic fluids. *Journal of Fluid Mechanics*, **343**, pp.73-94.

[59] Li, G., McKinley, G.H. and Ardekani, A.M., 2015. Dynamics of particle migration in channel flow of viscoelastic fluids. *Journal of Fluid Mechanics*, **785**, pp.486-505.

[60] Bird, R.B., Armstrong, R.C. and Hassager, O., 1987. Dynamics of polymeric liquids. Vol. 1: Fluid mechanics. John Wiley and Sons.

[61] Gervang, B. and Larsen, P.S., 1991. Secondary flows in straight ducts of rectangular cross section. *Journal of Non-Newtonian Fluid Mechanics*, **39**(3), pp.217-237.

[62] Huang, P.Y. and Joseph, D.D., 2000. Effects of shear thinning on migration of neutrally buoyant particles in pressure driven flow of Newtonian and viscoelastic fluids. *Journal of Non-Newtonian Fluid Mechanics*, **90**(2-3), pp.159-185.

[63] Lu, X. and Xuan, X., 2015. Inertia-enhanced pinched flow fractionation. *Analytical Chemistry*, **87**(8), pp.4560-4565.

[64] Liu, C., Hu, G., Jiang, X. and Sun, J., 2015. Inertial focusing of spherical particles in rectangular microchannels over a wide range of Reynolds numbers. *Lab on a Chip*, **15**(4), pp.1168-1177.

[65] Villone, M.M., D'avino, G., Hulsen, M.A., Greco, F. and Maffettone, P.L., 2013. Particle motion in square channel flow of a viscoelastic liquid: Migration vs. secondary flows. *Journal of Non-Newtonian Fluid Mechanics*, **195**, pp.1-8.

CHAPTER FOUR

CONTINUOUS SHEATH-FREE SEPARATION OF DRUG-TREATED HUMAN FUNGAL PATHOGEN CRYPTOCOCCUS NEOFORMANS BY MORPHOLOGY IN BIOCOMPATIBLE POLYMER SOLUTIONS

4.1 Abstract

Cryptococcal meningitis caused by *Cryptococcus neoformans* is the most common cause of fungal central nervous system infection. Current antifungal treatments for cryptococcal infections are inadequate partly due to the occurrence of drug resistance. Preliminary data indicate that the treatment of the azole drug fluconazole changes the morphology of *C. neoformans* to form “multimeras” that are enlarged and consist of at least three connected cells. To analyze if these multimeric cells are a prerequisite for *C. neoformans* to acquire drug resistance, a tool capable of separating them from normal cells is critical. We extend our recently demonstrated sheath-free elasto-inertial particle separation technique to fractionate drug-treated *C. neoformans* cells by morphology in biocompatible polymer solutions. The separation performance is evaluated for both multimeric and normal cells in terms of three dimensionless metrics: efficiency, purity and enrichment ratio. The effects of flow rate, polymer concentration and microchannel height on cell separation are studied.

4.2 Introduction

Cryptococcal meningitis caused by *Cryptococcus neoformans* (an encapsulated yeast) is the most common cause of fungal central nervous system infection in the world, primarily producing disease in immune-compromised patients[1.] Despite mounting public health threats, current treatments for cryptococcal infections are still inadequate. This is partly because *C. neoformans* acquires resistance to fluconazole, an azole antifungal drug, via becoming aneuploid with an increased copy number of key resistance genes[2,3]. Preliminary data indicate that the fluconazole treatment changes the morphology of *C. neoformans* from round unbudded cells or cells with a single bud to "multimeras" that are enlarged and consist of at least three cells connected together (Fig 4.1). It is hypothesized that the formation of multimeric cells is a prerequisite for *C. neoformans* to acquire drug resistance. To elucidate the mechanism through which the multimeric cells lead to drug resistant population, it is critical to separate the drug-treated *C. neoformans* cells based on morphology for further analysis.

Microfluidic devices have been extensively used to separate and sort cells due to a number of advantages over their macro-scale counterparts such as enhanced efficiency, improved accuracy and reduced cost etc.[4,5]. Separation based on intrinsic cell properties (e.g., size and density) in a continuous flow has recently become an increasing trend[6,7]. However, the majority of these label-free microfluidic approaches have been restricted to separate cells with dissimilar sizes, which often become inefficient in handling real samples due to the inherent heterogeneity of cells [8]. It is thus desirable to combine two or more intrinsic cell properties to develop a multi-parameter cell separation technique for practical biomedical applications. Morphology can potentially be such a passive biomarker that includes multiple aspects of cells including size, shape and structure etc. It is a fundamental cell property[9] that provides important information in, for example, cell synchronization[10] and disease diagnostic[11] etc. However, only until recently has the morphology (or simply shape) been utilized to separate (synthetic) particles or (biological) cells in microfluidic devices. These continuous-flow separations can be classified into two categories: one needs to use a sheath flow to pre-focus particles or cells prior to separation in the transverse direction (termed *sheath-focusing* separation), and the other uses an externally applied or internally induced force field to direct particles or cells toward morphology-dependent equilibrium positons (termed *sheath-free* separation).

The first *sheath-focusing* separation of particles by morphology was reported by Sugaya et al.[12], who extended their developed hydrodynamic filtration technique[13] to separate pre-aligned spherical and non-spherical polystyrene particles in a network of microchannels. Beech et al.[14] utilized the deterministic lateral displacement[15] to place morphologically altered red blood cells to dissimilar streamlines in a laminar flow around an array of obstacles. Recently, Lu and Xuan[16] demonstrated an efficient separation of equal-volumed spherical and peanut-shaped polystyrene particles in a viscoelastic polyethylene oxide (PEO) solution via elasto-inertial pinched flow fractionation[17]. The biocompatibility of this polymer solution has been demonstrated by several research groups to handle a variety of cell types (e.g., bacteria, blood cells and cancer cells etc.)[18-21]. Zhou and Xuan[22] used the shape-dependent magnetophoretic motion to separate a sheath-focused mixture of spherical and non-spherical particles in a ferrofluid. This magnetic method was later extended by the same group to fractionate a heterogeneous mixture of yeast cells by morphology[23]. More recently, Zhou et al.[24] separated pre-focused magnetic particles of dissimilar shapes under a uniform magnetic field via the shape-dependent magnetic rotation[25].

Among *sheath-free* particle and cell separations by morphology, Valero et al.[26] employed multi-frequency dielectrophoresis[27] to synchronize the yeast cell division. Kose et al.[28] exploited the AC field frequency-dependent magnetic force and torque to separate sickle and healthy red blood cells in a ferrofluid. DuBose et al.[29] demonstrated a low-throughput DC field-driven separation of spherical and non-spherical particles in a spiral microchannel via curvature-induced dielectrophoresis[30]. In contrast, Masaeli et al.[31] achieved a high-throughput inertial sorting of spheroid particles with different aspect ratios as well as yeast cells at different cell cycle stages in a straight rectangular microchannel. A similar method was later demonstrated by the same group to separate microalga *Euglena gracilis*[32]. Recently, Lu et al.[33] demonstrated a sheathless separation of equal-volumed spherical and peanut-shaped polystyrene particles in the flow of a viscoelastic polymer solution. The intermediate flow throughput of this elasto-inertial separation fills the gap between the dielectrophoretic[29] and inertial separations[31] with a higher efficiency and a higher purity.

We extend in this work our recently demonstrated sheath-free elasto-inertial separation of polystyrene particles by shape[33] or size[34] to fractionate fluconazole-treated *C. neoformans* cells by morphology. The simultaneous variations in cell shape and size after the drug treatment fail the majority of existing cell separation methods. This is because the force experienced by a cell in nearly every field decreases for less spherical cells while increases for larger cells. Therefore, the transverse motion of larger irregularshaped yeast cells becomes similar to that of smaller round-shaped ones under the application of a single force field. Our elasto-inertial particle separation technique[33,34] resolves this issue by the use of the combination of flow-induced elastic and inertial lift forces in biocompatible polymer solutions. We will perform a systematic experimental study of the factors that affect the cell separation performance.

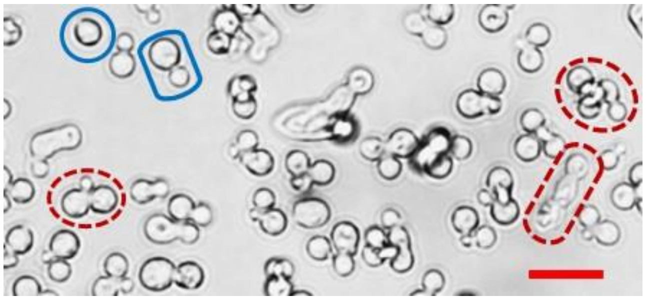

Fig. 4.1. Close-up view of drug-treated *C. neoformans* cells, which are divided into two primary groups based on morphology: one is normal cells with no buds or single buds (highlighted using the solid-line boxes), and the other is multimeric cells with two or more buds (highlighted using the dashed-line boxes). The scale bar represents 10 µm.

4.3 Experiment

4.3.1 Preparation and drug-treatment of yeast cells

C. neoformans strain H99 cells[35] were grown overnight at 24 °C in the yeast extract peptone dextrose (YPD) medium. They were refreshed next day to a density of 10^7 cells/ml before the treatment of forcholorfenuron (FCF) (CAS Number: 61857-60-8, Sigma Aldrich), a synthetic plant cytokinin that has been reported to interrupt cytokinesis in *Saccharomyces cerevisiae*[36]. The culture of *C. neoformans* was incubated in the YPD medium with 0.25 mM FCF overnight at 37 °C. The treated cells were then fixed with 3.7%

formaldehyde for 1 hour and spun down followed by the re-suspension in phosphate buffered saline (PBS) solution for later experiments. Fig. 4.1 shows a zoom-in image of the FCF-treated yeast cells that exhibit aberrant morphology. We divide these cells into two primary groups: one group with regular morphologies is the normal cells that have no buds or single bugs, and the other group with abnormal morphologies is the multimeric cells that have three or more connected cells/buds. The equivalent spherical diameter of each group of yeast cells was determined using the geometry package in COMSOL® via a three-dimensional model with the measured cell dimensions and structure (assuming spherical for each cell or bud). The average equivalent spherical diameter is approximately 5 μm and 7 μm for the normal and multimeric cells, respectively[23].

4.3.2 Manipulation of drug-treated yeast cells in polymer solutions

Prior to experiment, the FCF-treated *C. neoformans* cells were washed three times with the PBS solution using a mini centrifuge (Fisher Scientific). They were then re-suspended in PBS-based PEO solutions at a density of about 10^5 cells/ml. Three concentrations of PEO solutions, i.e., 500 ppm, 1000 ppm and 2000 ppm, were made by dissolving certain amounts of PEO powder (molecular weight, $M_w = 2 \times 10^6$ Da, Sigma-Aldrich) into the PBS solution. The rheology properties of these polymer solutions are listed in Table 4.1[16,34]. The prepared yeast cell suspension was injected into a straight rectangular microchannel using a syringe pump (KD Scientific). Fig. 4.2 (A) shows a top-view picture of the channel, which was fabricated with polydimethylsiloxane (PDMS) using the standard soft lithography method. The main body of this channel is 50 μm wide and 2 cm long, immediately followed by a 900 µm wide and 2 mm long sudden expansion at the outlet for enhanced cell separation and visualization via the local spreading and deceleration of cell streams. Three channel heights, i.e., 15 µm, 25 µm and 40 µm, were used in our experiments. The motion of cells was visualized through an inverted microscope (Nikon Eclipse TE2000U, Nikon Instruments) with a CCD camera (Nikon DS-Qi1Mc) at a rate of around 15 frames per second. A larger magnification was also used in order for the visual identification of individual cell morphology. The obtained digital images were processed using the Nikon imaging software (NIS-Elements), and analyzed using the ImageJ software (National Institute of Health).

Table 4.1. Rheology properties (at 20 °C) of the prepared PBS-based PEO solutions[16,34].

properties	PEO concentration (ppm)		
	500	1000	2000
density (ρ, g/cm^3)	1.0	1.0	1.0
zero-shear viscosity (η_0, mPa·s)	1.8	2.3	4.1
effective relaxation time (λ_e, ms)	4.3	6.8	10.6

4.3.3 Test of yeast cell viability

In order to assess the polymer effects on cell viability, the untreated *C. neoformans* cell suspension was subjected to separation in PBS-based 1000 ppm PEO solution and counted. Approximately 10,000 yeast cells were then plated on a semisolid YPD medium. After one day of growth at room temperature, plates were examined under the microscope to assess the percentage of cells that grew into colonies. It was found that the survival rate of yeast cells in the polymer solution is close to 100%. This observation of biocompatibility is also supported by the reported studies on the viscoelastic manipulation of several types of other cells [18-21].

4.4 Theory

4.4.1 Mechanism of cell separation

Fig. 4.2 (B) shows the inherently induced lift forces on a suspended cell in the flow of viscoelastic fluids through a straight rectangular microchannel. The elastic lift is a result of the normal stress difference[37,38] over the channel cross-section. It has been suggested in our recent study [34] to be viewed as a combination of two opposing force components: one is the center-directed elastic lift component, $\mathbf{F}_{eL\to c}$, due to fluid elasticity, and the other is the wall-directed elastic lift component, $\mathbf{F}_{eL\to w}$, due to fluid elasticity and shear thinning. The total elastic lift, $\mathbf{F}_{eL} = \mathbf{F}_{eL\to c} + \mathbf{F}_{eL\to w}$, is often expressed in the following scale[39],

$$\mathbf{F}_{eL} \sim d^3 \lambda_e \nabla \dot{\gamma}^2 \tag{4-1}$$

where d is the (equivalent) spherical cell diameter, λ_e is the fluid relaxation time, and $\dot{\gamma}$ is the fluid shear rate. It increases with the Weissenberg number, Wi,

$$Wi = \lambda_e \dot{\gamma} = \lambda_e \frac{2U}{w} = \frac{2\lambda_e Q}{w^2 h} \tag{4-2}$$

where U is the average fluid velocity, w is the channel height, D is the typical cross-sectional dimension of the channel (e.g., hydraulic diameter), Q is the volumetric flow rate, and h is the channel height.

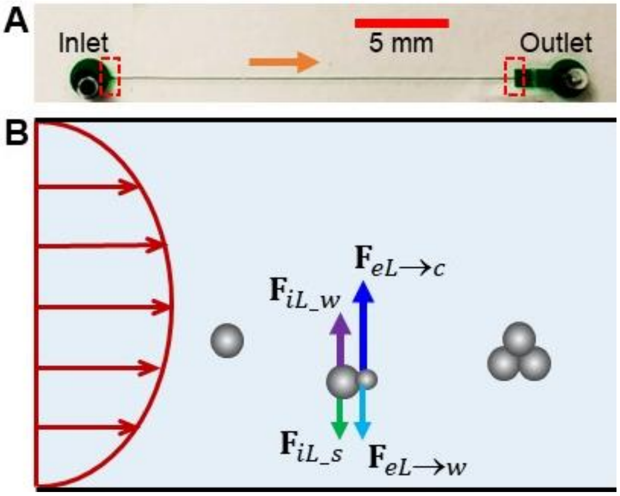

Fig. 4.2. (A) Top-view picture of the straight rectangular microchannel used in experiments, where the block arrow indicates the flow direction and the dashed-line boxes highlight the windows of view at the channel inlet and outlet, respectively. (B) Force analysis on a suspended cell in the flow of viscoelastic polymer solutions through a straight rectangular microchannel. The wall-induced inertial lift component, $\mathbf{F}_{iL\_w}$, and the shear gradient (see the parabolic velocity profile on the schematic)-induced inertial lift component, $\mathbf{F}_{iL\_s}$, direct the cell towards the channel center and wall, respectively. The fluid elasticity-induced elastic lift component, $\mathbf{F}_{eL\to c}$, and the fluid elasticity/shear thinning-induced elastic lift component, $\mathbf{F}_{eL\to w}$, direct the cell towards the channel center and wall, respectively.

The wall-induced inertial lift component, $\mathbf{F}_{iL\_w}$, pushes the cell away from the channel wall. The shear gradient-induced inertial lift component, $\mathbf{F}_{iL\_s}$, directs the cell towards the wall[40]. The balance of these two inertial lift components yields equilibrium cell positions that are a weak function of cell size or shape in straight rectangular microchannels[41]. The total inertial lift, $\mathbf{F}_{iL} = \mathbf{F}_{iL\_w} + \mathbf{F}_{iL\_s}$, on a cell has been theoretically proved to scale as[42],

$$\mathbf{F}_{iL} \sim \rho d^4 \dot{\gamma}^2 \qquad (4\text{-}3)$$

where ρ is the fluid density. This force is a strong function of the Reynolds number[41], Re, which for rectangular microchannels is defined as,

$$Re = \frac{\rho U D}{\eta_0} = \frac{2\rho Q}{\eta_0(w+h)} \tag{4-4}$$

where η_0 is the zero-shear fluid viscosity. It is often deemed effective only when the cell (or more generally particle) Reynolds number, Re_c,

$$Re_c = Re\left(\frac{d}{D}\right)^2 \tag{4-5}$$

is on the order of one (or more specifically ≥ 0.1)[41].

The relative contribution between the elastic lift, $\mathbf{F}_{eL}$ in Eq. (4-1), and the inertial lift, $\mathbf{F}_{iL}$ in Eq. (4-3), can be characterized by the dimensionless elasticity number, El, which is defined as the ratio of the Weissenberg number to Reynolds umber and hence independent of the flow kinematics.

$$El = \frac{Wi}{Re} = \frac{\lambda_e \eta_0 (w+h)}{\rho w^2 h} \tag{4-6}$$

As the two lift forces scale differently with the (equivalent) spherical diameter, cells with dissimilar sizes and/or shapes can be potentially directed to distinct equilibrium positions in viscoelastic fluid flows through simple straight rectangular microchannels. This enables a continuous-flow, sheath-free, and high-efficiency separation, which has been demonstrated in previous studies for size-based separation of (approximately) spherical particles and cells[18,34] as well as shape-based separation of equal-volumed particles[33]. We demonstrate in the following that such an elasto-inertial separation technique also works effectively for cells with simultaneously varying sizes and shapes.

4.4.2 Separation performance metrics

We evaluate the separation performance for both normal and multimeric yeast cells in terms of three dimensionless metrics[8]. The separation *efficiency* is defined as

$$efficiency = \frac{(N_i)_{zone}}{N_i} \tag{4-7}$$

where N_i is the total number of normal ($i = n$) or multimeric ($i = m$) cells at the channel outlet while $(N_i)_{zone}$ denotes the counted number of the same cell type within a specific zone of the channel outlet. The separation *purity* is defined as

$$purity = \frac{(N_i)_{zone}}{(N_n+N_m)_{zone}} \tag{4-8}$$

which measures the number of either target cell type (i.e., normal or multimeric) within a specific zone relative to that of all cells counted within the same zone of the channel outlet. The enrichment ratio, *ER*, is defined as the number ratio of one target cell type to the other within a specific zone at the channel outlet divided by the same ratio at the inlet. For example, the *ER* of normal cells is given by

$$ER = \frac{(N_n/N_m)_{zone}}{(N_n/N_m)_{inlet}} \tag{4-9}$$

4.5 Results and discussion

4.5.1 Demonstration of yeast cell separation

Fig. 4.3 shows the top-view images of the drug-treated yeast cells in the flow of PBS-based 1000 ppm PEO solution at the inlet (A) and the outlet expansion (B) of a 25 μm deep rectangular microchannel. The zoom-in view of the cells at these two locations are displayed as the inset plots I and II of Fig. 4.3, where the morphology of individual cells can be identified. The volumetric flow rate is 150 µL/h, and the calculated Reynolds number and Weissenberg number are $Re = 0.48$ and $Wi = 9.47$, respectively. The corresponding cell Reynolds number is $Re_c = 0.02$ even for the larger multimeric cells with an average equivalent spherical diameter of 7 µm. Therefore, the inertial effect should be weak in this experiment and the elastic lift dominates the force exerted on the cells. At the channel inlet (Fig. 4.3 (A)), the normal and multimeric cells are both uniformed distributed and mixed. At the outlet expansion (Fig. 4.3 (B)), the smaller and more spherical normal cells appear to exit the channel inside a tight zone around the channel centerline, specifically within approximately one-third of the local channel half-width as highlighted in the inset plot II of Fig. 4.3 (B). In contrast, the larger and less spherical multimeric cells are directed further away from the centerline by the combined elastic and inertial lift and found to exit the channel within the zone nearer to the channel sidewall. This observation is consistent with our previous studies where both smaller spherical polystyrene particles[34] and equal-volumed non-spherical polystyrene particles[33] are elasto-inertially focused in 1000 ppm PEO solution toward symmetric equilibrium positions closer to the centerline (or more accurately, the center-plane) of straight rectangular microchannels. The quantitative analysis of the performance metrics for this sheathless elasto-inertial cell separation by morphology is presented in the following section on the study of flow rate effects.

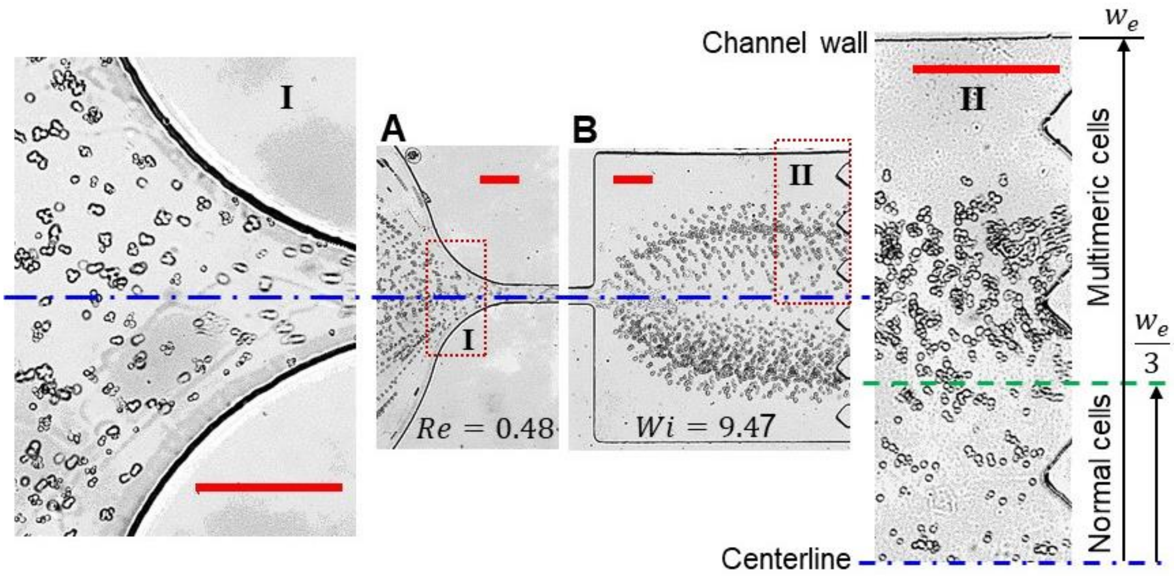

Fig. 4.3. Top-view images of drug-treated *C. neoformans* cells in the flow of PBS-based 1000 ppm PEO solution at the inlet (A) and the outlet expansion (B) of a 25 µm high straight rectangular microchannel. The inset plots I and II are the zoom-in views of the dashed-line highlighted regions at the channel inlet and outlet, respectively. The flow rate is 150 µL/h, and the corresponding values of the Reynolds number, Re, and Weissenberg number, Wi, are labeled on the images. The normal and multimeric cells are observed to exit the channel in the inner and outer zones of the outlet expansion that are divided at one-third of the local half-width, i.e., $w_e/3$, as indicated on inset II. The scale bars on all images represent 100 µm.

4.5.2 Effect of flow rate

Fig. 4.4 shows the influence of flow rate on the yeast cell separation demonstrated in Fig. 4.3 when all other conditions remain unvaried. With the increase of flow rate, the Reynolds and Weissenberg numbers both increase leading to enhanced inertial and elastic effects. The elasticity number, however, remains constant, and so the elastic lift should dominate in the entire range of flow rate under test. At the flow rate of 80 µL/h, all cells travel out of the straight microchannel in a single mixed stream along the centerline as viewed from the image in Fig. 4.4 (A). However, the dispersion of the multimeric cells is apparently greater than that of the normal cells, which is illustrated in Fig. 4.4 (B) by the larger span of the former cells’ exiting positions (symbols with error bars) at the outlet expansion. At 100 μL/h, approximately half of the multimeric cells move away from the stream along the centerline in Fig. 4.4 (A), and migrate toward a new equilibrium position that is about half way of the local half-width (see Fig. 4.4 (B)). In contrast, normal cells still stay near the centerline. When the flow rate is increased to 150 μL/h, the centerline equilibrium position disappears for both types of cells in Figure 4A. All the multimeric cells exit the channel at one-half of the local half-width while the normal cells have an average off-center exiting position of around one-quarter of the local half-width as seen from Fig. 4.4 (B). Further increasing the flow rate shifts outward the equilibrium position of the normal cells and hence reduces the gap from that of the multimeric cells that remains fixed.

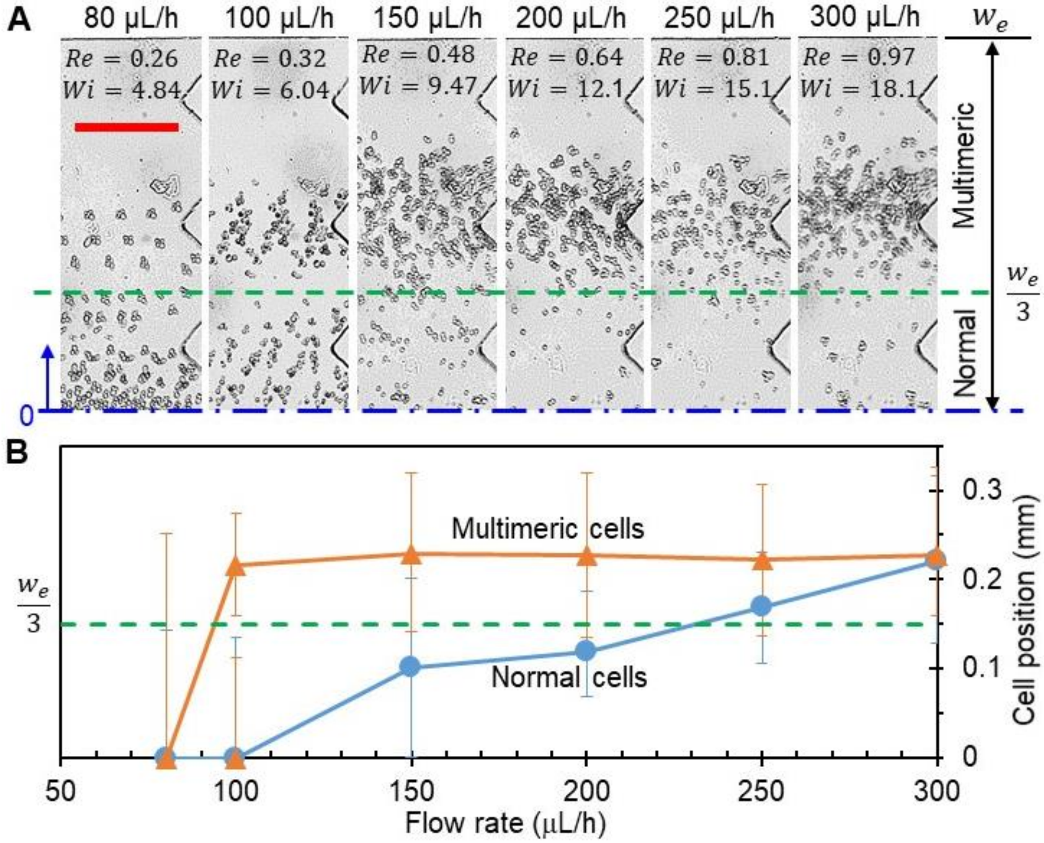

Fig. 4.4. Flow rate effect on the elasto-inertial separation of drug-treated *C. neoformans* cells in the flow of PBS-based 1000 ppm PEO solution through a 25 μm deep rectangular microchannel: (A) the top-view images of cells in the upper-half of the outlet expansion; (B) the average exiting positions (symbols with error bars) of the normal and multimeric cells at the channel outlet that were obtained from the images in (A) with respect to the channel centerline (see the arrow on the left-most image). The dashed line at the off-center position of one-third of the local channel half-width, i.e., $w_e/3$, in (A) and (B) divides the upper-half of the outlet expansion into the inner and outer zones for evaluating the separation performance metrics of normal and multimeric cells, respectively, in Fig 4.5. The calculated values of the Reynolds and Weissenberg numbers are labeled on the images in (A). The scale bar represents 100 μm.

Fig 4.5 plots the three performance metrics for the drug-treated yeast cell separation at different flow rates in Fig 4.4. They were evaluated using the definitions in Eqs. (4-7)-(4-9) for both the multimeric and the normal cells in the near-wall zone and the near-center zone, respectively. These outer and inner zones in the upper-half of the outlet expansion are split at the off-center position of one-third of the local channel half-width, i.e., the dashed line on the cell images in Fig 4.4 (A). The separation efficiency of multimeric cells increases from 30% at 80 µL/h to 93% at 150 µL/h and then stays roughly unchanged at higher flow rates (except 250 µL/h due to the significantly less number of cells counted in this test; see the image in Fig 4.4 (A)). This is because the multimeric cells have all migrated into the outer zone at 150 µL/h and above. The separation purity of multimeric cells achieves the highest value of 94% at 100 µL/h and drops at higher flow rates because normal cells start appearing in the outer zone. In contrast, the separation efficiency and purity of normal cells reach the highest values, both over 90%, at 100 and 150 µL/h, respectively. As a result, the multimeric and normal cells each achieve a greater than 12 enrichment ratio at the flow rates of 100 and 150 µL/h, respectively. The best separation performance for both types of cells should take place in a flow rate in between.

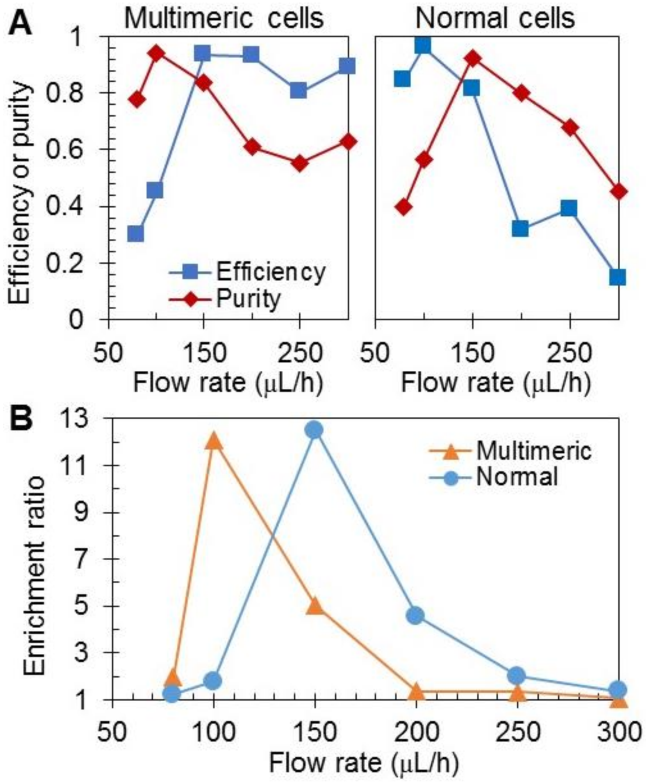

Fig. 4.5. Performance metrics for the elasto-inertial separation of drug-treated *C. neoformans* cells at different flow rates in Fig. 4.4: (A) the efficiency and purity for the multimeric (left plot) and normal (right plot) cells, respectively, and (B) the enrichment ratio of the two types of cells.

4.5.3 Effect of polymer concentration

Fig. 4.6 shows the influence of polymer concentration on the drug-treated yeast cell separation in PBS-based PEO solutions at a fixed flow rate of 150 μL/h. Increasing the PEO concentration increases the Weissenberg number (due to the longer fluid relaxation time) and decreases the Reynolds number (due to the larger fluid viscosity), leading to an increased elasticity number. Therefore, the elastic effect gets more dominant in a higher concentration PEO solution, which has been demonstrated in our previous studies to shift the equilibrium positions of both spherical and non-spherical polystyrene particles[33,34].

This consequence is, however, not obviously viewed from the images of cells at the outlet expansion in Fig. 4.6 (A) due to perhaps the wide range of variations in both the size and shape of the drug-treated yeast cells. Fig. 4.6 (B) compares the average exiting positions of the multimeric and normal cells at the outlet expansion, where the former is further away from the channel centerline in all three PEO concentrations. However, the focusing position of the larger and less spherical multimeric cells first shifts outward and then inward when the PEO concentration is increased from 500 ppm to 1000 ppm and 2000 ppm. In contrast, the focusing position of the smaller and more spherical normal cells slightly shifts inward with the increase of PEO concentration. Similar trends were also observed in our previous studies on spherical and peanut-shaped polystyrene particles[33,34]. The best cell separation is achieved in ~1000 ppm PEO solution

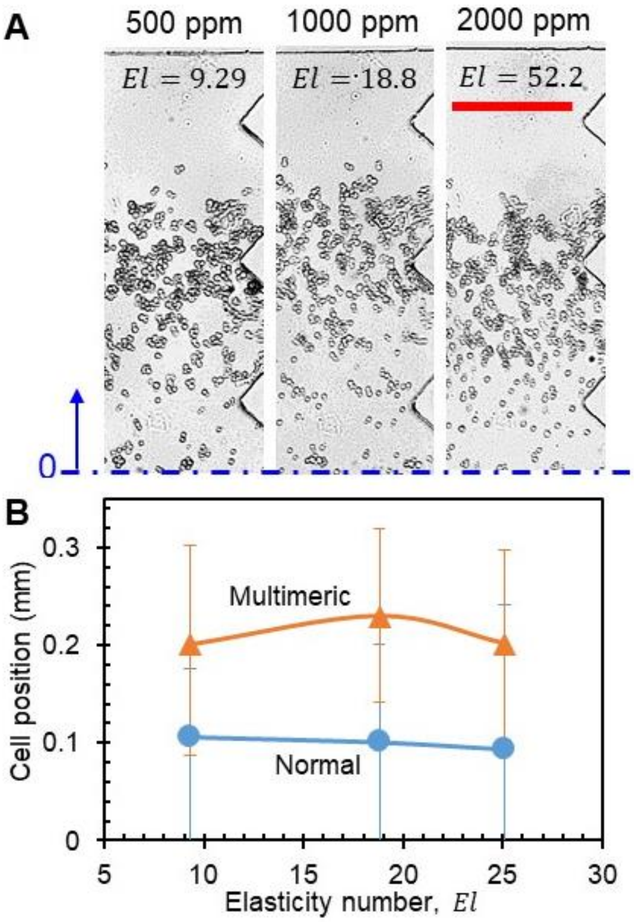

Fig. 4.6. Polymer concentration effect on the elasto-inertial separation of drug-treated *C. neoformans* cells in the flow of PBS-based PEO solutions in a 25 µm deep straight microchannel: (A) the top-view images of cells in the upper-half of the outlet expansion; (B) the average exiting positions (symbols with error bars) of the multimeric and normal cells at the channel outlet that were obtained from the images in (A) with respect to the channel centerline (see the arrow on the left-most image). The flow rate is fixed at 150 µL/h. The calculated values of the elasticity number are labeled on the images in (A). The scale bar in (A) represents 100 µm.

4.5.4 Effect of channel height

Fig. 4.7 shows the influence of channel height on the drug-treated yeast cell separation in PBS-based 1000 ppm PEO solution. The channel width is fixed at 50 µm. In a 15 µm high channel, the multimeric and normal cells each possess two similar equilibrium positions as viewed from both the cell images in Fig. 4.7 (A) and the cell exiting positions in Fig. 4.7 (B). The primary equilibrium position is about one-third of the local channel half-width away from the wall (as compared to the one-half in a 25 µm high channel; see Fig. 4.4), and slightly shifts inward with the increase of flow rate. The secondary equilibrium position is along the channel centerline, which is also observed for polystyrene particles in our previous studies[33,34]. In contrast, both types of yeast cells are directed toward the single equilibrium position along the channel centerline in a 40 µm high channel. Moreover, the elasto-inertial focusing gets improved at a higher flow rate for each type of cells (see the cell images in Fig. 4.7 (A)). Therefore, the multimeric and normal cells cannot be effectively separated in a 15 µm or a 40 µm high channel. This result is consistent with our recent studies on polystyrene particle separation by shape[33] or size[34].

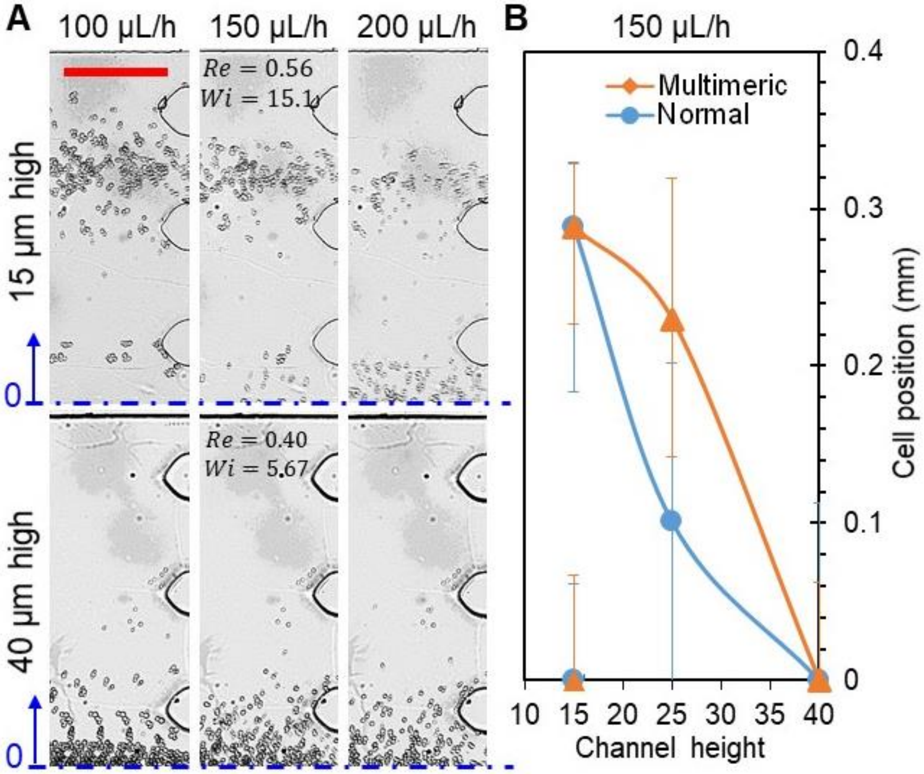

Fig. 4.7. Channel height effect on the elasto-inertial separation of drug-treated *C. neoformans* cells in the flow of PBS-based 1000 ppm PEO solutions: (A) the top-view images of cells in the upper-half of the outlet expansion in 15 µm (top row) and 40 µm (bottom row) high rectangular microchannels at different flow rates; (B) the average exiting positions (symbols with error bars) of the multimeric and normal cells at the channel outlet that were obtained from the images in (A) at the flow rate of 150 µL/h. The calculated values of the Reynolds and Weissenberg numbers for this flow rate are labeled on the images in (A). The scale bar in (A) represents 100 µm.

4.6 Conclusion

We have built upon our recent work[33,34] to demonstrate a continuous-flow sheath-free separation of drug-treated *C. neoformans* cells by morphology in the flow of biocompatible PBS-based PEO solutions through straight rectangular microchannels. The heterogeneous mixture of yeast cells with varying shapes and sizes are elasto-inertially focused toward morphology-dependent equilibrium positions. Consistent with our previous observations for polystyrene particles[33,34], the larger, abnormal-shaped multimeric cells are found to stay further away from the channel center than the smaller, regular-shaped normal cells. We have studied the flow rate effect on this separation, whose performance is evaluated in terms of three dimensionless metrics including efficiency, purity and enrichment ratio. We have also studied the effects of PEO concentration and channel height on the morphology-based yeast cell separation. The best separation performance is achieved in 1000 ppm PEO solution flow through an intermediate channel width/height ratio (two in the current work) at the flow rate of the order of 100 µL/h. This throughput fills in the gap between those of the sheathless dielectrophoretic (about one order of magnitude smaller)[29] and inertial (about one order of magnitude larger)[31,32] separations of particles and cells by shape.

Acknowledgements This work was supported in part by NIH under Grant 1R15 AI119801-01 (L.K.), and NSF under Grant CBET-1150670 (X.X.).

References

[1] Franzot, S.P., Mukherjee, J., Cherniak, R., Chen, L.C., Hamdan, J.S. and Casadevall, A., 1998. Microevolution of a Standard Strain of Cryptococcus neoformans Resulting in Differences in Virulence and Other Phenotypes. *Infection and Immunity*, **66**(1), pp.89-97.

[2] Xu, J., Onyewu, C., Yoell, H.J., Ali, R.Y., Vilgalys, R.J. and Mitchell, T.G., 2001. Dynamic and heterogeneous mutations to fluconazole resistance in Cryptococcus neoformans. *Antimicrobial Agents and Chemotherapy*, **45**(2), pp.420-427.

[3] Sionov, E., Lee, H., Chang, Y.C. and Kwon-Chung, K.J., 2010. Cryptococcus neoformans overcomes stress of azole drugs by formation of disomy in specific multiple chromosomes. *PLoS Pathogens*, **6**(4), p.e1000848.

[4] Sajeesh, P. and Sen, A.K., 2014. Particle separation and sorting in microfluidic devices: a review. *Microfluidics and Nanofluidics*, **17**(1), pp.1-52.

[5] Yan, S., Zhang, J., Yuan, D. and Li, W., 2017. Hybrid microfluidics combined with active and passive approaches for continuous cell separation. *Electrophoresis*, **38**(2), pp.238-249.

[6] Karimi, A., Yazdi, S. and Ardekani, A.M., 2013. Hydrodynamic mechanisms of cell and particle trapping in microfluidics. *Biomicrofluidics*, **7**(2), p.021501.

[7] Shields IV, C.W., Reyes, C.D. and López, G.P., 2015. Microfluidic cell sorting: a review of the advances in the separation of cells from debulking to rare cell isolation. *Lab on a Chip*, **15**(5), pp.1230-1249.

[8] Gossett, D.R., Weaver, W.M., Mach, A.J., Hur, S.C., Tse, H.T.K., Lee, W., Amini, H. and Di Carlo, D., 2010. Label-free cell separation and sorting in microfluidic systems. *Analytical and Bioanalytical Chemistry*, **397**(8), pp.3249-3267.

[9] Jadhao, V., Thomas, C.K. and de la Cruz, M.O., 2014. Electrostatics-driven shape transitions in soft shells. *Proceedings of the National Academy of Sciences*, **111**(35), pp.12673-12678.

[10] Champion, J.A. and Mitragotri, S., 2006. Role of target geometry in phagocytosis. *Proceedings of the National Academy of Sciences*, **103**(13), pp.4930-4934.

[11] Martin, S.G., 2009. Geometric control of the cell cycle. *Cell Cycle*, **8**(22), pp.3643-3647.

[12] Sugaya, S., Yamada, M. and Seki, M., 2011. Observation of nonspherical particle behaviors for continuous shape-based separation using hydrodynamic filtration. *Biomicrofluidics*, **5**(2), p.024103.

[13] Yamada, M. and Seki, M., 2005. Hydrodynamic filtration for on-chip particle concentration and classification utilizing microfluidics. *Lab on a Chip*, **5**(11), pp.1233-1239.

[14] Beech, J.P., Holm, S.H., Adolfsson, K. and Tegenfeldt, J.O., 2012. Sorting cells by size, shape and deformability. *Lab on a Chip*, **12**(6), pp.1048-1051.

[15] Huang, L.R., Cox, E.C., Austin, R.H. and Sturm, J.C., 2004. Continuous particle separation through deterministic lateral displacement. *Science*, **304**(5673), pp.987-990.

[16] Lu, X. and Xuan, X., 2015. Elasto-inertial pinched flow fractionation for continuous shape-based particle separation. *Analytical Chemistry*, **87**(22), pp.11523-11530.

[17] Lu, X. and Xuan, X., 2015. Continuous microfluidic particle separation via elasto-inertial pinched flow fractionation. *Analytical Chemistry*, **87**(12), pp.6389-6396.

[18] Liu, C., Xue, C., Chen, X., Shan, L., Tian, Y. and Hu, G., 2015. Size-based separation of particles and cells utilizing viscoelastic effects in straight microchannels. *Analytical Chemistry*, **87**(12), pp.6041-6048.

[19] Yuan, D., Tan, S.H., Sluyter, R., Zhao, Q., Yan, S., Nguyen, N.T., Guo, J., Zhang, J. and Li, W., 2017. On-chip microparticle and cell washing using coflow of viscoelastic fluid and newtonian fluid. *Analytical Chemistry*, **89**(17), pp.9574-9582.

[20] Tian, F., Zhang, W., Cai, L., Li, S., Hu, G., Cong, Y., Liu, C., Li, T. and Sun, J., 2017. Microfluidic co-flow of Newtonian and viscoelastic fluids for high-resolution separation of microparticles. *Lab on a Chip*, **17**(18), pp.3078-3085.

[21] Holzner, G., Stavrakis, S. and DeMello, A., 2017. Elasto-inertial focusing of mammalian cells and bacteria using low molecular, low viscosity PEO solutions. *Analytical Cchemistry*, **89**(21), pp.11653-11663.

[22] Zhou, Y. and Xuan, X., 2016. Diamagnetic particle separation by shape in ferrofluids. Applied Physics *Letters*, **109**(10), p.102405.

[23] Chen, Q., Li, D., Zielinski, J., Kozubowski, L., Lin, J., Wang, M. and Xuan, X., 2017. Yeast cell fractionation by morphology in dilute ferrofluids. *Biomicrofluidics*, **11**(6), p.064102.

[24] Zhou, R., Bai, F. and Wang, C., 2017. Magnetic separation of microparticles by shape. *Lab on a Chip*, **17**(3), pp.401-406.

[25] Zhou, R., Sobecki, C.A., Zhang, J., Zhang, Y. and Wang, C., 2017. Magnetic control of lateral migration of ellipsoidal microparticles in microscale flows. *Physical Review Applied*, **8**(2), p.024019.

[26] Valero, A., Braschler, T., Rauch, A., Demierre, N., Barral, Y. and Renaud, P., 2011. Tracking and synchronization of the yeast cell cycle using dielectrophoretic opacity. *Lab on a Chip*, **11**(10), pp.1754-1760.

[27] Urdaneta, M. and Smela, E., 2007. Multiple frequency dielectrophoresis. *Electrophoresis*, **28**(18), pp.3145-3155.

[28] Kose, A.R., Fischer, B., Mao, L. and Koser, H., 2009. Label-free cellular manipulation and sorting via biocompatible ferrofluids. *Proceedings of the National Academy of Sciences*, **106**(51), pp.21478-21483.

[29] DuBose, J., Lu, X., Patel, S., Qian, S., Woo Joo, S. and Xuan, X., 2014. Microfluidic electrical sorting of particles based on shape in a spiral microchannel. *Biomicrofluidics*, **8**(1), p.014101.

[30] Zhu, J., Tzeng, T.R.J. and Xuan, X., 2010. Continuous dielectrophoretic separation of particles in a spiral microchannel. *Electrophoresis*, **31**(8), pp.1382-1388.

[31] Masaeli, M., Sollier, E., Amini, H., Mao, W., Camacho, K., Doshi, N., Mitragotri, S., Alexeev, A. and Di Carlo, D., 2012. Continuous inertial focusing and separation of particles by shape. *Physical Review X*, **2**(3), p.031017.

[32] Li, M., Muñoz, H.E., Goda, K. and Di Carlo, D., 2017. Shape-based separation of microalga Euglena gracilis using inertial microfluidics. *Scientific Reports*, **7**(1), p.10802.

[33] Lu, X., Zhu, L., Hua, R.M. and Xuan, X., 2015. Continuous sheath-free separation of particles by shape in viscoelastic fluids. *Applied Physics Letters*, **107**(26), p.264102.

[34] Li, D., Lu, X. and Xuan, X., 2016. Viscoelastic separation of particles by size in straight rectangular microchannels: a parametric study for a refined understanding. *Analytical Chemistry*, **88**(24), pp.12303-12309.

[35] Perfect, J.R., Ketabchi, N., Cox, G.M., Ingram, C.W. and Beiser, C.L., 1993. Karyotyping of Cryptococcus neoformans as an epidemiological tool. *Journal of Clinical Microbiology*, **31**(12), pp.3305-3309.

[36] Iwase, M., Okada, S., Oguchi, T. and Toh-e, A., 2004. Forchlorfenuron, a phenylurea cytokinin, disturbs septin organization in Saccharomyces cerevisiae. *Genes & genetic systems*, **79**(4), pp.199-206.

[37] Bird, R.B., Armstrong, R.C. and Hassager, O., 1987. Dynamics of polymeric liquids. Vol. 1: Fluid mechanics. John Wiley and Sons.

[38] D'Avino, G., Greco, F. and Maffettone, P.L., 2017. Particle migration due to viscoelasticity of the suspending liquid and its relevance in microfluidic devices. *Annual Review of Fluid Mechanics*, **49**, pp.341-360.

[39] Lu, X., Liu, C., Hu, G. and Xuan, X., 2017. Particle manipulations in non-Newtonian microfluidics: A review. *Journal of Colloid and Interface Science,* **500**, pp.182-201.

[40] Di Carlo, D., 2009. Inertial microfluidics. *Lab on a Chip*, **9**(21), pp.3038-3046.

[41] Di Carlo, D., Edd, J.F., Humphry, K.J., Stone, H.A. and Toner, M., 2009. Particle segregation and dynamics in confined flows. *Physical Review Letters*, **102**(9), p.094503.

[42] Asmolov, E.S., 1999. The inertial lift on a spherical particle in a plane Poiseuille flow at large channel Reynolds number. *Journal of Fluid Mechanics*, **381**, pp.63-87.

CHAPTER FIVE

THE MOTION OF RIGID PARTICLES IN THE POISEUILLE FLOW OF SHEAR-THINNING FLUIDS THROUGH STRAIGHT RECTANGULAR MICROCHANNELS

5.1 Abstract

There has been in the past decade a significantly growing interest in the use of flow-induced lift forces for a passive control of particle motion in microchannels. This nonlinear microfluidic technique can be implemented in both Newtonian and non-Newtonian fluids. The motions of rigid particles in confined flows of viscoelastic fluids with and without shear-thinning effects have each been well studied in the literature. However, a comprehensive understanding of particle motion in inelastic shear-thinning fluids is still lacking. We present herein a systematic experimental study of the motion of rigid particles in the Poiseuille flow of pseudoplastic xanthan gum (XG) solutions through straight rectangular microchannels. We find that the number and location of particle equilibrium positions are both a strong function of channel dimension, particle size and XG concentration. We attempt to explain the experimental observations using the competition of inertial and elastic lift forces acting on particles. Our experimental results imply a potentially high throughput separation of rigid particles by size in XG solutions.

5.2 Introduction

Since the development of polydimethylsiloxane (PDMS)-based soft lithography technique[19], microfluidic devices have been widely used to focus [78], trap[27], concentrate[60], and separate[65] particles (from biological cells to synthetic beads, rigid particles to soft drops etc.) for many chemical, biomedical and environmental applications[32,61,69]. A variety of external force fields (e.g., acoustic[7], electric[38], magnetic[58] and optical[80] fields) has thus far been demonstrated to *actively* control the motion of particles in these devices. However, there has recently been a significantly growing interest in the use of flow-induced inherent lift and/or drag forces for a *passive* control of particle motion in microchannels[3,52]. This nonlinear microfluidic technique [71] has been implemented in both Newtonian[17,56,86] and non-Newtonian[9,53,85] fluids. It has the capability to achieve a very high throughput with the advantages of simplicity and effectiveness[29,48]. Moreover, it has the potential to integrate with an active particle manipulation technique [e.g., dielectrophoresis[37] or magneto-phoresis[6,12,36,87,88]] for enhanced sensitivity, specificity and flexibility[79].

The lift forces on particles in *passive* microfluidic techniques can be induced by three different effects: fluid inertia, fluid non-Newtonian rheology, and particle deformation[40]. The inertia of fluid causes rigid particles to move across the flow towards specific lateral positions in Newtonian fluids[25,68]. Such an inertial focusing is the foundation of the so-called inertial microfluidics[17] that has found wide applications[24,71,86] since its first demonstration in PDMS-based rectangular microchannels[16]. The non-Newtonian properties of fluid yield an elastic lift[33,34] because of the gradients in normal stress differences, which directs particles towards the low shear rate regions in the absence of fluid inertia[26,39]. The shape change causes deformable particles to move towards either the channel center or walls depending on the ratio of the dispersed-to-continuous fluid viscosity[21,57,72].

The motion of rigid particles in the flow of non-Newtonian fluids through microchannels has been increasingly studied [10,53,85] since the work of Leshansky et al. in 2007[42]. A range of viscoelastic polymer solutions [e.g., polyvinylpyrrolidone (PVP) (11,64,75,77), polyethylene oxide (PEO)[41,43,50,54,55,76,84], and polyacrylamide (PAA) [42,49]] and biological fluids [e.g., hyaluronic acid (HA)[1,48,59] and DNA solutions[31,35]] have been tested, where fluid elasticity and shear thinning are each found to play a significant role in the lateral particle migration. Specifically, the fluid elasticity effect causes particles to move to the region(s) of the lowest shear rate[67,73,82], which is, however, strongly influenced by the fluid inertial effect[46,73,81]. The fluid shear-thinning effect promotes the particle migration away from the channel centerline[8,13,14,28,51,66,70].

In a recent study, we performed a systematic experimental study of both the individual and the combined effects of fluid inertia, elasticity and shear thinning on the motion of rigid spherical particles in a straight rectangular microchannel[45]. We tested the particle motion in four types of non-Newtonian fluids with distinct rheological properties: strongly elastic PVP solution with a negligible shear-thinning effect[50], inelastic xanthan gum (XG) solution with a strong shear-thinning effect [30], moderately elastic PEO solution with a relatively weak shear-thinning effect[15], and strongly elastic PAA solution with a strong shear-thinning effect [62]. As noted above, the motions of rigid particles in confined flows of viscoelastic PVP, PEO and PAA solutions as well as viscoelastic DNA and HA solutions with varying parameters have each been investigated in the literature[52,53,84]. However, a comprehensive understanding of particle motion in inelastic shear-thinning [i.e., pseudoplastic[22,23]] fluids is still lacking. We therefore perform in this work a detailed parametric study of the effects of channel dimension, particle size and polymer concentration on the motion of rigid particles in the Poiseuille flow of XG solutions through straight rectangular microchannels. This study will improve our understanding of how fluid non-Newtonian rheology affects particle motion in microchannels.

5.3 Experiment

5.3.1 Particle suspensions

Three concentrations of XG solutions were used in our experiments: 500 ppm, 2000 ppm and 3750 ppm. They were each prepared by dissolving a certain amount of XG powders (Tokyo Chemical Industry) into deionized water (Fisher Scientific). Their rheological properties are listed in Table 5.1, which are extracted from the literature[30] due to the lack of measuring equipment in our lab. These XG solutions are all strongly shear thinning with the power-law index n decreasing at a higher XG concentration. Their viscosities, η, can be estimated using the Carreau-Yasuda model[83] based on the average fluid shear rate across the microchannel width, $\bar{\dot{\gamma}} = 2V/w$,

$$\frac{\eta-\eta_\infty}{\eta_0-\eta_\infty} = [1 + (\lambda_{CY}\bar{\dot{\gamma}})^a]^{(n-1)/a} \tag{5-1}$$

In the above, V is the average fluid velocity, w is the channel width, η_∞ is the infinite-shear-rate viscosity, η_0 is the zero-shear-rate viscosity, λ_{CY} is a time constant, and a is a fitting parameter. The values of these parameters for the three types of XG solutions are given in Table 5.1. Spherical fluorescent (green) polystyrene particles of 10 μm in diameter (Thermo Scientific) were re-suspended in each of the prepared solutions for the study of XG concentration effect. Also, spherical fluorescent particles of 5 μm (Thermo

Scientific) and 20 μm (Phosphorex) in diameter were re-suspended into 2000 ppm XG solution for the study of particle size effect.

Table 5.1. Rheological properties (refer to Eq. (5-1) for the definitions of symbols) of the prepared XG solutions at 20 °C. All values are extracted from Japper-Jaafar et al.[30]

XG concentration	n	η_0 (Pa•s)	η_∞ (Pa•s)	λ_{CY} (s)	a
500 ppm	0.58	1.97×10^{-2}	1.13×10^{-3}	3.88×10^{-1}	2.10
2000 ppm	0.34	3.68	2.24×10^{-3}	$2.15\times10^{+1}$	0.81
3750 ppm	0.19	$2.85\times10^{+2}$	4.60×10^{-3}	$4.14\times10^{+2}$	1.47

5.3.2 Experimental setup

Fig. 5.1 (a) shows a picture of the straight rectangular microchannel, which was fabricated with polydimethylsiloxane (PDMS) using a custom-modified soft lithography technique as described elsewhere[47]. The channel was measured 2 cm long with a fixed width of 68 (±2) μm. It was, however, made to have three different depths, i.e., 30 μm, 54 μm and 127 μm, for the study of channel aspect ratio effect on particle motion in XG solutions. At each end of the microchannel was there an expansion region with an array of patterned posts for the filtration of any debris. We used a right-angle prism (NT 32-526, Edmund Optics Inc.) to visualize the particle motion in the vertical plane of the microchannel (i.e., side view), which complemented the view in the horizontal plane (i.e., top view). The prism was pre-embedded into the PDMS slab and placed right before the outlet expansion with a 400 μm distance from the channel edge. The prepared particle suspension was driven through the microchannel using a syringe pump (KD Scientific). Particle motion was recorded through an inverted fluorescent microscope (Nikon Eclipse

TE2000U, Nikon Instrument) with a CCD camera (Nikon DS-Qi1Mc) at a rate of around 15 frame/s. Particle streak images were generated by stacking a sequence of snapshot images with the maximum intensity projection in Nikon imaging software (NIS-Elements AR 2.30). Particle intensity plots were obtained from reading the values of gray scale intensity of particle images in MATLAB®, which were then scaled (after the background intensity was subtracted) and plotted over the channel width or depth.

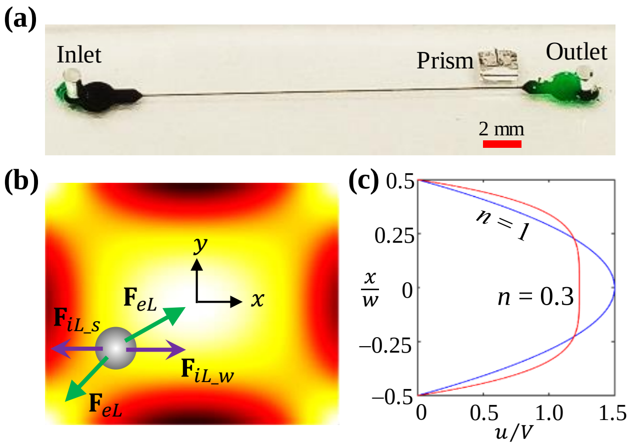

Fig. 5.1 (a) Picture of a straight rectangular microchannel with a right-angle prism embedded before the outlet expansion for viewing the particle motion from the side; (b) Schematic illustration of the inertial and elastic lift forces acting on a particle in the flow of XG solution through a straight rectangular microchannel, where the background color shows the contour of fluid shear rate, $\dot{\gamma}$ (the darker the larger magnitude), in the cross-section; (c) widthwise profile of the flow velocity, $u(x, y)$ (scaled by the average velocity, V), for Newtonian ($n = 1$) and shear-thinning ($n = 0.3$) fluids in a straight rectangular microchannel.

5.4 Theory

5.4.1 Force analysis

Fig. 5.1 (b) shows schematically the inertial and elastic lift forces acting on a neutrally buoyant spherical particle in the flow of XG solutions through a straight rectangular microchannel. The fluid inertia-driven lift, $\mathbf{F}_{iL}$, can be broken into two competing components: the wall-induced inertial lift, $\mathbf{F}_{iL\_w}$, pushes the particle away from any channel walls because of the pressure increase in the particle-wall gap; the shear gradient-induced inertial lift, $\mathbf{F}_{iL\_s}$, directs the particle towards the high shear-rate region, i.e., the center of each face (see the contour of fluid shear rate in Fig. 5.1 (b)), because of the curvature of fluid velocity profile[17,25,40]. The following formula has been often suggested to evaluate the total inertial lift[2],

$$\mathbf{F}_{iL} = \mathbf{F}_{iL\_w} + \mathbf{F}_{iL\_s} \sim \rho d^4 \dot{\gamma}^2 \tag{5-2}$$

where ρ is the fluid density, d is the particle diameter, and $\dot{\gamma}$ is the local fluid shear rate.

The fluid elasticity-driven lift, $\mathbf{F}_{eL}$, results from the non-uniform normal stress differences in non-Newtonian fluid flows[10,39]. As the magnitude of second normal stress difference, N_2, is usually much smaller than that of the first normal stress difference, N_1, in polymer solutions[5], $\mathbf{F}_{eL}$ can be viewed proportional to the variation of N_1 over the size of the particle[42], i.e.,

$$\mathbf{F}_{eL} \sim d^3 \nabla N_1 \tag{5-3}$$

Similar to other diluted solutions of high molecular weight polymers[4], N_1 of XG solutions, though small, has been demonstrated[20,74] to exhibit a power-law behavior, $N_1 = A\dot{\gamma}^m$, where A and m are both fluid-dependent constants with m typically in the range $1 < m \leq 2$ [4]. Hence, Eq. (5-3) can be rewritten as

$$\mathbf{F}_{eL} \sim d^3 A \nabla \dot{\gamma}^m \tag{5-4}$$

where $\mathbf{F}_{eL}$ points towards the low shear rate region, i.e., the center and four corners of the channel cross-section (see the shear rate contour in Fig. 5.1 (b)).

Due to their strong dependences of the local shear rate, $\dot{\gamma}$, the inertial and elastic lift forces are both affected by the fluid velocity profile. As viewed from the plot in Fig. 5.1 (c), the velocity profile of a shear-thinning fluid flow ($n = 0.3$ as an example) gets flat near the channel center, in contrast to the parabolic profile of a Newtonian fluid flow ($n = 1$). Therefore, the shear gradient-induced inertial lift, $\mathbf{F}_{iL\_s}$, differs near the channel center in the flow of XG solutions. Such a variation should work with the additional elastic lift, $\mathbf{F}_{eL}$, to shift the equilibrium particle positions in XG solutions as compared to those in Newtonian fluids, which has been demonstrated in our recent study[45]. Specifically, we observed that 10 µm particles migrate to both the channel center and corners (i.e., the lowest shear rate region, see the background color in Fig. 5.1 (b)) in an inertialess flow of 2000 ppm XG solution through a nearly square microchannel. Increasing the fluid inertia shifts particles away from both the center and corner equilibrium positions towards a mid-plane in between.

5.4.2 Dimensionless numbers

The inertial and elastic lift forces are both a strong function of the (channel) Reynolds number,

$$Re = \frac{\rho V D_h}{\eta(\bar{\dot{\gamma}})} = \frac{2\rho Q}{\eta(\dot{\gamma})(w+h)} \quad (5\text{-}5)$$

where D_h is the hydraulic diameter of the microchannel, $\eta(\bar{\dot{\gamma}})$ is the fluid viscosity estimated via Eq. (5-1) using the average fluid shear rate across the channel width, Q is the volumetric flow rate, and h is the channel height. The value of Re is used to study the flow rate effect, and that of the power-law index, n, in Eq. (5-1) is used to study the XG concentration effect. The particle size effect is studied using the confinement ratio,

$$\beta = d/D_h \quad (5\text{-}6)$$

and the channel dimension effect is studied using the aspect ratio,

$$AR = w/h \quad (5\text{-}7)$$

Another dimensionless number that is often used to characterize the inertial lift is the particle Reynolds number[17],

$$Re_p = \beta^2 Re \quad (5\text{-}8)$$

Note that $Re_p > 0.1$ has been suggested as one criterion for effective inertial focusing of particles in straight rectangular microchannels[3,56].

5.5 Results and discussion

5.5.1 Effect of channel depth

Fig. 5.2 illustrates the motions of 10 µm particles in the flow of 2000 ppm XG solution through straight rectangular microchannels of 30 µm ($AR = 2.27$), 54 µm ($AR = 1.26$) and 127 µm ($AR = 0.54$) depths, respectively, within the same range of flow rates. In a roughly square microchannel with $AR = 1.26$, particles are seen from the top- and side-view images in Fig. 5.2 (b) to travel near the channel center and corners when the flow rate is no higher than 1 mL/h (at which $Re = 0.78$). This migration is primarily a result of the elastic lift, $\mathbf{F}_{eL}$, which, in the absence of inertial focusing (because of $Re_p < 0.02$)[17], should direct particles towards the low shear rate regions over the channel cross-section (see the contour of fluid shear rate in the right-most schematic of Fig. 5.2 (b)). Increasing the flow rate leads to an enhanced inertial lift, which, as reported in our previous study[45], acts to push particles away from both the channel center (due to the shear gradient-induced inertial lift component, $\mathbf{F}_{iL\_s}$; see Fig. 5.1 (b)) and corners (due to the wall-induced inertial lift component, $\mathbf{F}_{iL\_w}$; see Fig. 5.1 (b)) towards a mid-plane in between. It also enhances the elastic lift though at a smaller rate as viewed from the dissimilar shear rate dependences of the two lift forces in Eq. (5-2) and Eq. (5-4), respectively. It is important to note that the velocity profile of shear-thinning fluids becomes closer to that of Newtonian fluids with the increase of flow rate as demonstrated in Fig. 5.3. Therefore, $\mathbf{F}_{iL\_s}$, though vanishingly small near the channel centerline at a small Re because of the locally zero shear rate (see also Fig. 5.1 (c)), grows with increasing Re. The elasto-inertial equilibrium positions at the flow rate of 10 mL/h are schematically shown in the cross-sectional view of Fig. 5.2 (b).

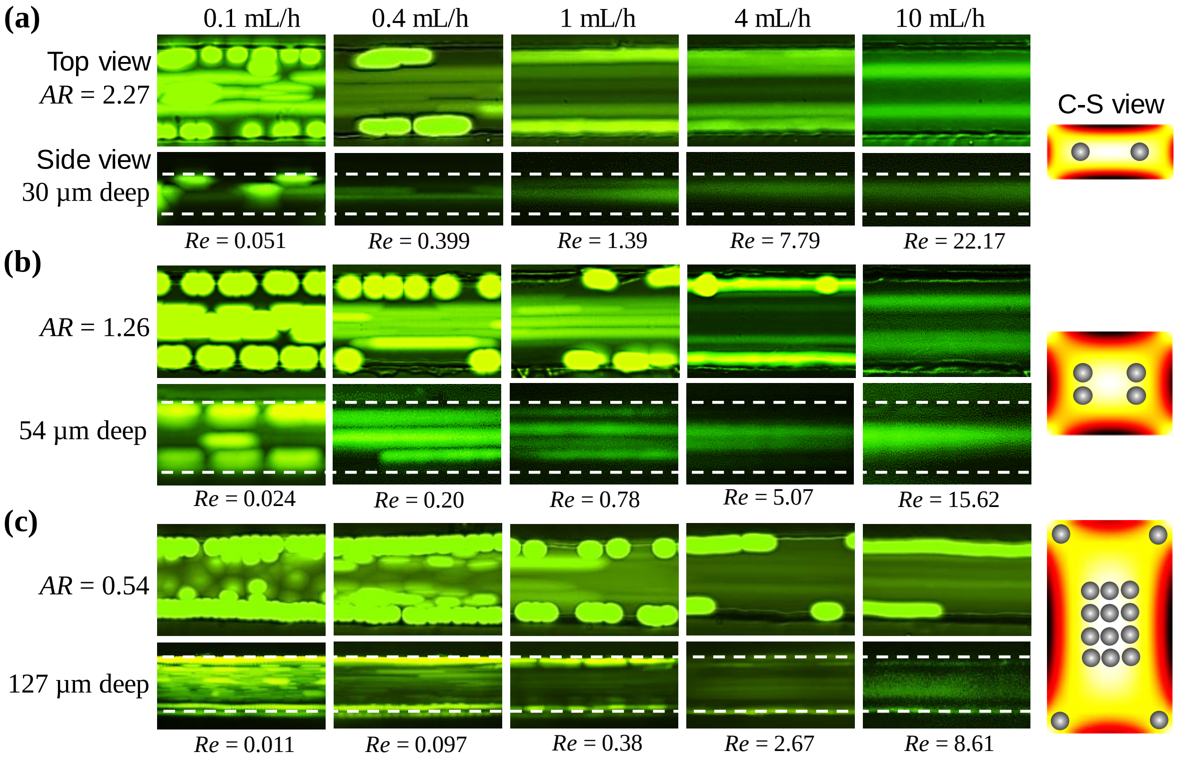

Fig. 5.2. Migration of 10 μm particles in the flow of 2000 ppm XG solution through straight rectangular microchannels of varying depths: (a) 30 μm deep (with an aspect ratio of $AR = 2.27$); (b) 54 μm deep ($AR = 1.26$); (c) 127 μm deep ($AR = 0.54$). The volumetric flow rate increases from 0.1 mL/h to 10 mL/h and the corresponding values of Re are highlighted below the images. The particle images in the upper and lower rows of (a, b, c) represent the top and side views, respectively, at the channel outlet. The schematics in the right-most column illustrate the equilibrium particle positions over the cross-section (C-S) of each microchannel (estimated from the top and side view images at 10 mL/h, drawn to scale), where the background color shows the contour of fluid shear rate (the darker the larger magnitude) in the XG solution.

In a shallower microchannel with a larger $AR = 2.27$ (Fig. 5.2 (a)), the inertial effect starts altering the elastic equilibrium positions near the channel center and corners at the flow rate of 1 mL/h (at which $Re = 1.39$) because of the increase in both Re and particle confinement ratio ($\beta = 0.24$) as compared to the roughly square microchannel (where $Re = 0.78$ and $\beta = 0.17$) in Fig. 5.2 (b). This phenomenon takes place even earlier (at 0.4 mL/h in Fig. 5.2 (a)) in the vertical plane of the microchannel, where the elastic and inertial lift forces both increase due to the greater shear rate and shear rate gradients therein. The equilibrium particle positions at higher flow rates turn out to be similar to those in the microchannel with $AR = 1.26$ in Fig. 5.2 (b), except that the elasto-inertial particle focusing in the former is visually better (particularly in the depth direction, see the images at 10 mL/h in Fig. 5.2 (a)) due to the greater particle confinement ratio therein. In the deepest microchannel with $AR = 0.54$, particles are not observed from the images in Fig. 5.2 (c) to move away from the channel center or corners in the entire range of flow rates under test. Moreover, those particles traveling around the channel center do not exhibit an apparent focusing trend like that in the two shallower microchannels (Fig. 5.2 (a) and Fig. 5.2 (b)). Three factors could possibly play a role in these observations. Firstly, the fluid inertia is the weakest in the deepest channel at the same flow rate, which reduces both the elastic and inertial lift forces. Secondly, the low shear rate region significantly expands as compared to the shallower microchannels, especially at the channel corners (see the contour of fluid shear rate in the right-most schematic of Fig. 5.2 (c)), which increases the elastic force towards the corners while decreasing that towards the channel center. Thirdly, the particle confinement ratio becomes the smallest ($\beta = 0.11$) among the three microchannels, which should also weaken both of the flow-induced lift forces.

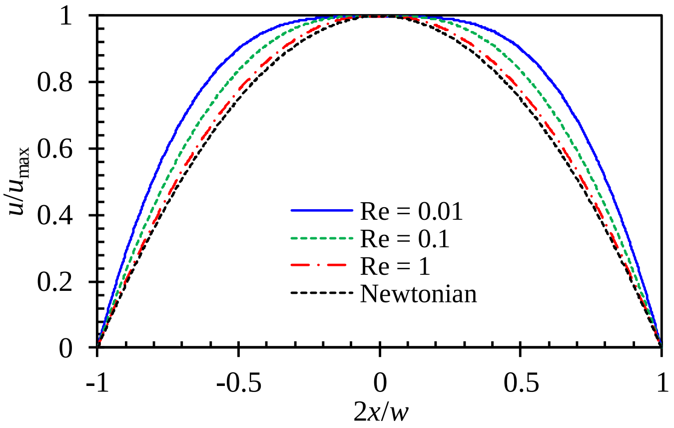

Fig. 5.3. Velocity (scaled by the centerline velocity, u_{max}) profiles for the flow of shear-thinning (with $n = 0.34$ in the Carreau-Yasuda model, Eq. (5-1), for 2000 ppm XG solution) and Newtonian fluids at varying values of Re. Note the velocity profile of Newtonian fluid flow is independent of Re.

The above trends for particle motion in XG solutions through microchannels of varying depths are quantitatively illustrated by the plots of particle intensity in Fig. 5.4. The intensity values were obtained directly from the particle images in Fig. 5.2, and further scaled to different levels for distinguishing the curves at different flow rates (specifically, 0.8, 0.5 and 0.2 for 0.1 mL/h, 1 mL/h and 10 mL/h, respectively). It is seen from the intensity curves in the horizontal plane (Fig. 5.4 (a)) that particles are overall pushed away from the walls when the channel depth decreases or the flow rate increases. Two primary particle positions, which should be (approximately) symmetric with respect to the channel center, are observed in each depth of microchannel. Their separation distance, however, appears to become smaller in a shallower channel. The intensity curves in the vertical plane (Fig. 5.4 (b)) demonstrate a similar trend to that in the horizontal plane. However, the number of equilibrium particle positions reduces to one at the channel center in the two shallower microchannels if the flow rate is sufficiently high.

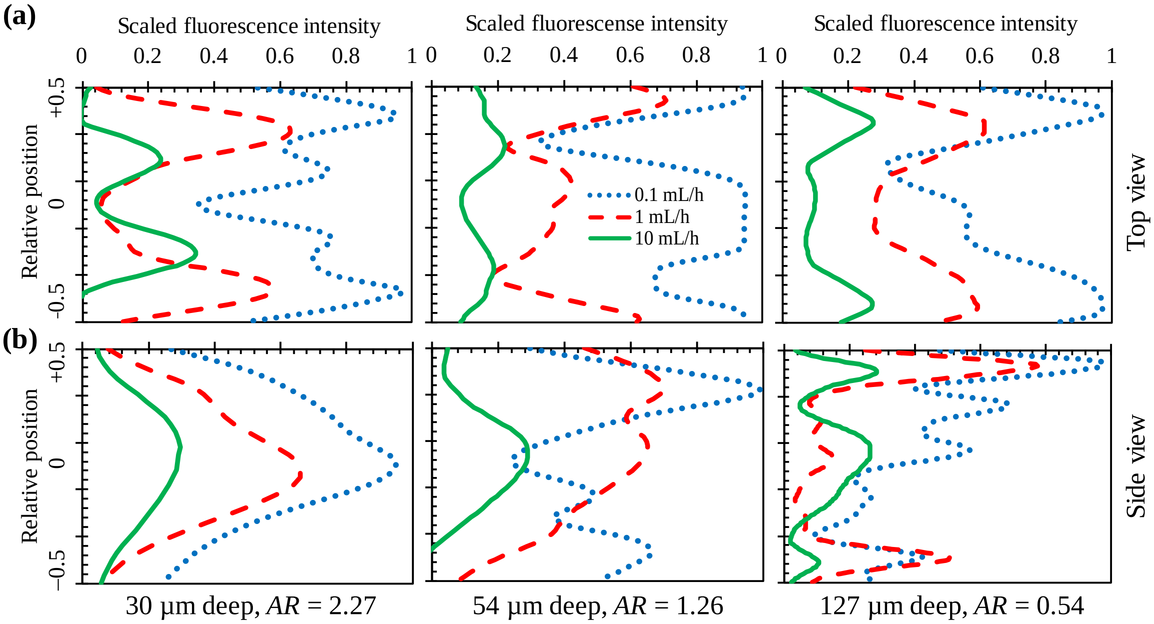

Fig. 5.4. Scaled intensity plots for 10 μm particles in the flow of 2000 ppm XG solution through microchannels of 30 μm, 54 μm and 127 μm depths at the flow rates of 0.1 mL/h, 1 mL/h and 10 mL/h, respectively: (a) in the horizontal plane of the channel; (b) in the vertical plane of the channel. The intensity values in (a) and (b) were obtained from the top- and side-view particle images, respectively, in Fig. 5.2.

5.5.2 Effect of particle size

Fig. 5.5 compares the motions of 5 μm, 10 μm and 20 μm particles in the flow of 2000 ppm XG solution through a 54 μm deep rectangular channel ($AR = 1.26$) in the same range of flow rates. When the flow rate is not higher than 1 mL/h (at which $Re = 0.78$ and hence inertial effects are still insignificant), both 5 μm (Fig. 5.5 (a)) and 20 μm (Fig. 5.5 (c)) particles behave similar to 10 μm ones (Fig. 5.5 (b)). They all travel near the channel center and corners in the top-view images at the channel outlet because of the primary action of the elastic lift. With the further increase of flow rate, inertial lift starts playing a role in the motion of each type of particles. However, as the elastic lift in Eq. (5-4) is a weaker function of particle size than the inertial lift in Eq. (5-2), their relative magnitude (i.e., elastic to inertial ratio) increases for smaller particles. Therefore, the elastic effect should remain dominant for 5 μm particles at increasing flow rates, which explains why their motion does not change strongly with flow rate in Fig. 5.5 (a). Moreover, similar to 10 μm particles in the 127 μm deep microchannel (Fig. 5.2 (c)), those 5 μm particles that travel around the channel center do not achieve a noticeable focusing because of the small confinement ratio, $\beta = 0.08$ (see the schematic in Fig. 5.5 (a), where the particles and channel are drawn to scale).

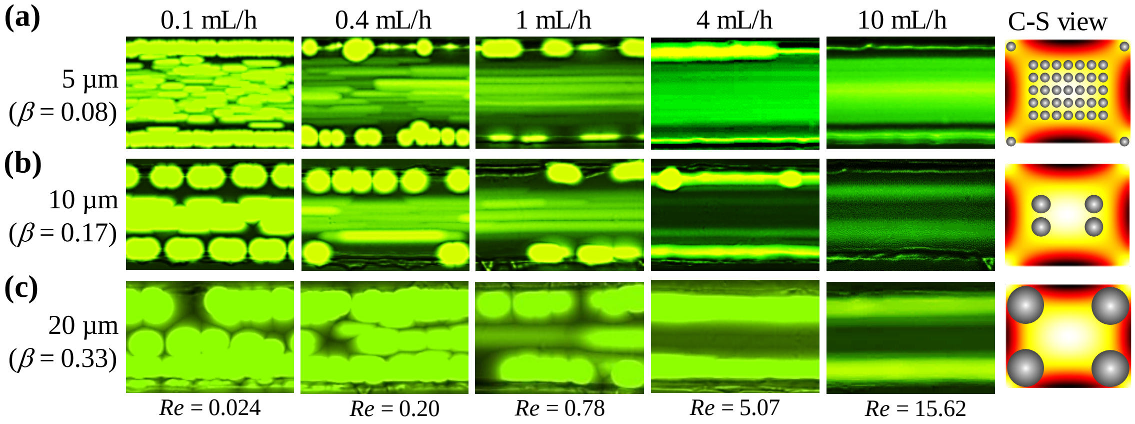

Fig. 5.5. Migration of 5 μm (with a confinement ratio of $\beta = 0.08$, a), 10 μm ($\beta = 0.17$, b) and 20 μm ($\beta = 0.33$, c) particles in the flow of 2000 ppm XG solution through a 54 μm deep straight rectangular microchannel under varying flow rates. The corresponding values of Re (independent of particle size) are highlighted below the particle images (top view) at the channel outlet. The schematics in the right-most column illustrate the equilibrium particle positions over the channel cross-section (C-S) (estimated from the images at 10 mL/h, drawn to scale), where the background color shows the contour of fluid shear rate (the darker the larger magnitude) in the XG solution.

In contrast, as the inertial effect increases faster than the elastic lift for larger particles, 20 μm particles are observed from the top-view images in Fig. 5.5 (c) to move away from the channel center at the flow rate of 4 mL/h and above. However, they are not directed towards a mid-plane in between the channel center and corners like 10 µm particles (Fig. 5.5 (b)). Instead, 20 µm particles sustain the near-corner equilibrium positions in the range of flow rates under test, which seems to resemble the near-wall (more specifically, near the center of each face) motion of large particles in confined inertial flows[17] because of the fairly large confinement ratio, $\beta = 0.33$ (see the schematic in Fig. 5.5 (c)). It is important to note from Fig. 5.5 (b,c) that we may separate 20 µm and 10 µm particles via the differential elasto-inertial focusing in 2000 ppm XG solution. The motions of the three types of particles in Fig. 5.5 are also quantitatively demonstrated using the scaled particle intensity plots in Fig. 5.6. With the decrease of particle size, the primary elasto-inertial equilibrium positions in the horizontal plane shift from two near the corners to one along the channel center. Moreover, particles of any sizes are overall pushed away from the channel walls when the flow rate increases, which is similar to that of 10 µm particles in microchannels of different depths (see Fig. 5.4) because of the increasing inertial effect.

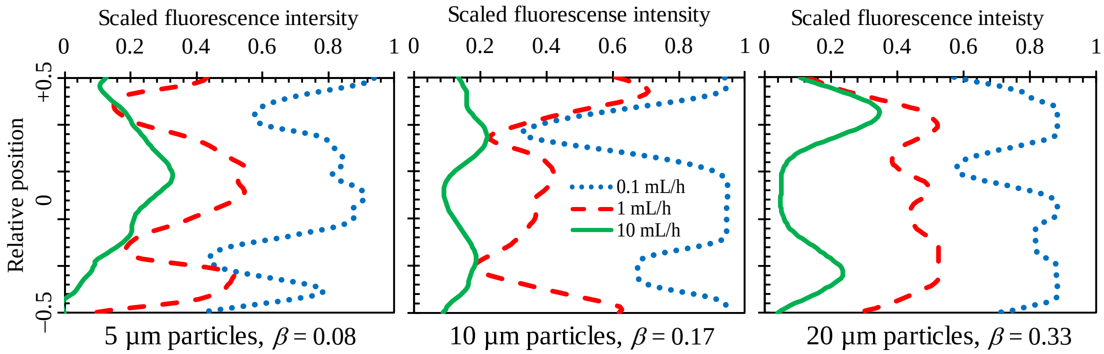

5 µm particles, $\beta = 0.08$ 10 µm particles, $\beta = 0.17$ 20 µm particles, $\beta = 0.33$

Fig. 5.6. Scaled intensity plots for 5 µm, 10 µm and 20 µm particles in the flow of 2000 ppm XG solution through a 54 µm deep microchannel at the flow rates of 0.1 mL/h, 1 mL/h and 10 mL/h, respectively. The intensity values were obtained from the particle images in Fig. 5.5.

5.5.3 Effect of XG concentration

Fig. 5.7 shows the motions of 10 µm particles in the flow of 500 ppm, 2000 ppm and 3750 ppm XG solutions, respectively, through a 54 µm deep microchannel ($AR = 1.26$) in the same range of flow rates. Increasing the XG concentration enhances the fluid shear-thinning effect, which is reflected by the decreasing power-law index from $n = 0.58$ to 0.34 and 0.19 (see Table 5.1). When the flow rate is less than 1 mL/h, the inertial effect is weak compared to the elastic effect such that particles travel near the channel center and corners in all three XG solutions. Increasing the flow rate enhances both the elastic and inertial lift forces, between which the latter increases at a greater rate because of its stronger dependence on fluid shear rate [see Eq. (5-2) vs. Eq. (5-4)]. This leads to the observed shifting of 10 µm particles towards an equilibrium mid-plane between the channel center and corners in 2000 ppm XG solution as noted above (see Fig. 5.7 (b)). Reducing the XG concentration to 500 ppm decreases the elastic lift while increasing the inertial lift at the same flow rate because of the decrease in fluid viscosity (see Table 5.1) and in turn the increase in Re. It also changes the shear rate distribution (see the right-most schematic of Fig. 5.7 (a)) and hence the flow-induced lift forces. The result is a significantly weakened two-stream focusing of particles near the channel center with a very small portion of them retained near the corners. In contrast, increasing the XG concentration to 3750 ppm enhances the elastic lift and decreases the inertial lift, yielding a single equilibrium particle position at the channel center (Fig. 5.7 (c)). Fig. 5.8 compares the particle intensity plots in the three XG solutions. With the increase of flow rate, particles are again observed to move away from the channel walls because of the enhanced inertial effect. Moreover, their equilibrium positions shift further towards the channel center when the XG concentration increases because of the enhanced elastic effect.

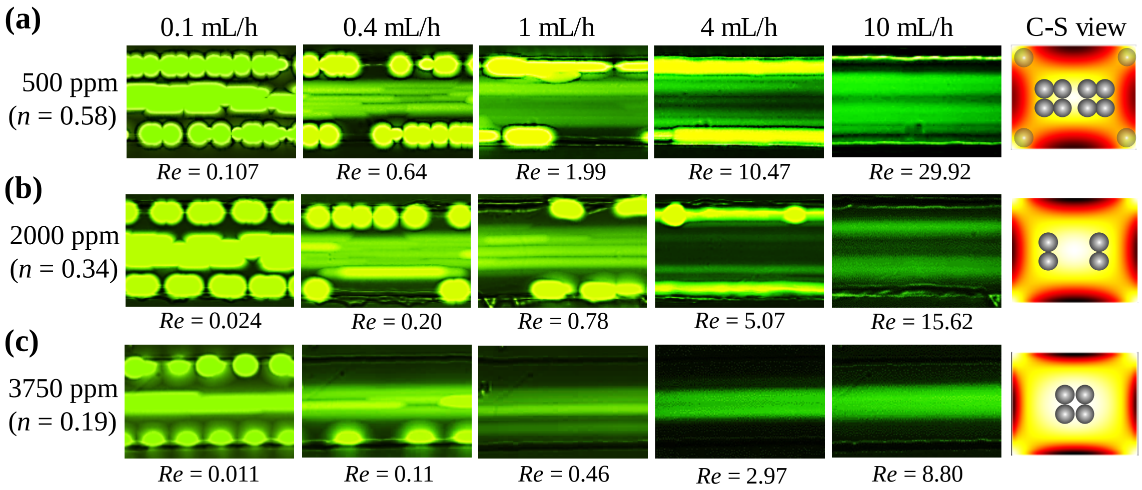

Fig. 5.7. Migration of 10 μm particles in the flow of 500 ppm (with a power-law index of $n = 0.58$, a), 2000 ppm ($n = 0.34$, b) and 3750 ppm ($n = 0.19$, c) XG solutions through a 54 μm deep straight rectangular microchannel under varying flow rates. The corresponding values of Re (strong function of XG concentration) are highlighted below the particle images (top view) at the channel outlet. The schematics in the right-most column illustrate the equilibrium particle positions over the channel cross-section (C-S) (estimated from the images at 10 mL/h, drawn to scale), where the background color shows the contour of fluid shear rate (the darker the larger magnitude) in the corresponding XG solution.

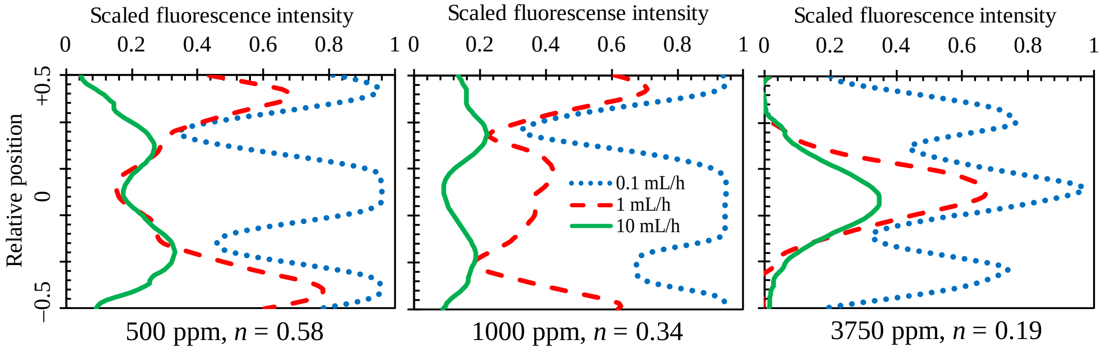

Fig. 5.8. Scaled intensity plots for 10 μm particles in the flow of 500 ppm, 2000 ppm and 3750 ppm XG solutions through a 54 μm deep microchannel at the flow rates of 0.1 mL/h,

1 mL/h and 10 mL/h, respectively. The intensity values were obtained from the particle images in Fig. 5.7.

5.6 Conclusions

We have conducted a systematic experimental study of the parametric effects on rigid particle motion in XG solutions through straight rectangular microchannels. We find that when the flow rate is low, particles travel out of the channel near both the corners and centerline in all cases because of the sole action of elastic lift. With the increase of flow rate, nearly all the near-corner particles move away from the channel walls because of the enhanced wall-induced inertial lift. The only exception is the largest 20 µm particles that stay near the corners in the entire range of flow rates under test because of the strong elastic lift and the large particle confinement ratio. Meanwhile, those near-centerline particles migrate outward because of the enhanced shear gradient-induced inertial lift unless the microchannel is too deep (127 µm depth in our test, which expands the low shear rate region and reduces the elastic and inertial lift forces), or the particle is too small (5 µm particles in our test, which experience an insufficient inertial lift), or the XG concentration is too high (3750 ppm in our test, which exhibits a strong elastic effect). Interestingly, these observed phenomena imply a potentially high throughout separation of rigid particles based on the difference in size in the flow of XG solutions through simple straight rectangular microchannels. We will study the feasibility of such a continuous sheath- and label-free particle separation in future work.

Acknowledgments This work was supported in part by NSF under Grant No. CBET-1704379.

References

[1] Asghari, M., Serhatlioglu, M., Ortaç, B., Solmaz, M.E. and Elbuken, C., 2017. Sheathless microflow cytometry using viscoelastic fluids. *Scientific Reports*, **7**(1), p.12342.

[2] Asmolov, E.S., 1999. The inertial lift on a spherical particle in a plane Poiseuille flow at large channel Reynolds number. *Journal of Fluid Mechanics*, **381**, pp.63-87.

[3] Amini, H., Lee, W. and Di Carlo, D., 2014. Inertial microfluidic physics. *Lab on a Chip*, **14**(15), pp.2739-2761.

[4] Barnes, H.A., Hutton, J.F. and Walters, K., 1989. An introduction to rheology. Elsevier.

[5] Bird, R.B., Armstrong, R.C. and Hassager, O., 1987. Dynamics of polymeric liquids. Vol. 1: Fluid mechanics. John Wiley and Sons.

[6] Chen, Q., Li, D., Lin, J., Wang, M. and Xuan, X., 2017. Simultaneous Separation and Washing of Nonmagnetic Particles in an Inertial Ferrofluid/Water Coflow. *Analytical Chemistr*y, **89**(12), pp.6915-6920.

[7] Connacher, W., Zhang, N., Huang, A., Mei, J., Zhang, S., Gopesh, T. and Friend, J., 2018. Micro/nano acoustofluidics: materials, phenomena, design, devices, and applications. *Lab on a Chip*, **18**(14), pp.1952-1996.

[8] D'Avino, G., Romeo, G., Villone, M.M., Greco, F., Netti, P.A. and Maffettone, P.L., 2012. Single line particle focusing induced by viscoelasticity of the suspending liquid: theory, experiments and simulations to design a micropipe flow-focuser. *Lab on a Chip*, **12**(9), pp.1638-1645.

[9] D’Avino, G. and Maffettone, P.L., 2015. Particle dynamics in viscoelastic liquids. *Journal of Non-Newtonian Fluid Mechanics*, **215**, pp.80-104.

[10] D'Avino, G., Greco, F. and Maffettone, P.L., 2017. Particle migration due to viscoelasticity of the suspending liquid and its relevance in microfluidic devices. *Annual Review of Fluid Mechanics*, **49**, pp.341-360.

[11] Del Giudice, F., Romeo, G., D'Avino, G., Greco, F., Netti, P.A. and Maffettone, P.L., 2013. Particle alignment in a viscoelastic liquid flowing in a square-shaped microchannel. *Lab on a Chip*, **13**(21), pp.4263-4271.

[12] Del Giudice, F., Madadi, H., Villone, M.M., D'Avino, G., Cusano, A.M., Vecchione, R., Ventre, M., Maffettone, P.L. and Netti, P.A., 2015. Magnetophoresis 'meets' viscoelasticity: deterministic separation of magnetic particles in a modular microfluidic device. *Lab on a Chip*, **15**(8), pp.1912-1922.

[13] Del Giudice, F., D'Avino, G., Greco, F., Netti, P.A. and Maffettone, P.L., 2015. Effect of fluid rheology on particle migration in a square-shaped microchannel. *Microfluidics and Nanofluidics*, **19**(1), pp.95-104.

[14] Del Giudice, F., Sathish, S., D'Avino, G. and Shen, A.Q., 2017. "From the edge to the center": viscoelastic migration of particles and cells in a strongly shear-thinning liquid flowing in a microchannel. *Analytical Chemistry*, **89**(24), pp.13146-13159.

[15] De Santo, I., D'Avino, G., Romeo, G., Greco, F., Netti, P.A. and Maffettone, P.L., 2014. Microfluidic lagrangian trap for brownian particles: Three-dimensional focusing down to the nanoscale. *Physical Review Applied*, **2**(6), p.064001.

[16] Di Carlo, D., Irimia, D., Tompkins, R.G. and Toner, M., 2007. Continuous inertial focusing, ordering, and separation of particles in microchannels. *Proceedings of the National Academy of Sciences*, **104**(48), pp.18892-18897.

[17] Di Carlo, D., 2009. Inertial microfluidics. *Lab on a Chip*, **9**(21), pp.3038-3046.

[18] Di Carlo, D., Edd, J.F., Humphry, K.J., Stone, H.A. and Toner, M., 2009. Particle segregation and dynamics in confined flows. *Physical review letters*, **102**(9), p.094503.

[19] Duffy, D.C., McDonald, J.C., Schueller, O.J. and Whitesides, G.M., 1998. Rapid prototyping of microfluidic systems in poly (dimethylsiloxane). *Analytical Chemistry*, **70**(23), pp.4974-4984.

[20] Escudier, M.P. and Smith, S., 1999. Turbulent flow of Newtonian and shear-thinning liquids through a sudden axisymmetric expansion. *Experiments in Fluids*, **27**(5), pp.427-434.

[21] Geislinger, T.M. and Franke, T., 2014. Hydrodynamic lift of vesicles and red blood cells in flow—from Fåhræus & Lindqvist to microfluidic cell sorting. *Advances in colloid and interface science*, **208**, pp.161-176.

[22] Gauthier, F., Goldsmith, H.L. and Mason, S.G., 1971. Particle motions in non-Newtonian media. *Rheologica Acta*, **10**(3), pp.344-364.

[23] Gauthier, F., Goldsmith, H.L. and Mason, S.G., 1971. Particle motions in non-Newtonian media. II. Poiseuille flow. *Transactions of the Society of Rheology*, **15**(2), pp.297-330.

[24] Gou, Y., Jia, Y., Wang, P. and Sun, C., 2018. Progress of inertial microfluidics in principle and application. *Sensors*, **18**(6), p.1762.

[25] Ho, B.P. and Leal, L.G., 1974. Inertial migration of rigid spheres in two-dimensional unidirectional flows. *Journal of Fluid Mechanics*, **65**(2), pp.365-400.

[26] Ho, B.P. and Leal, L.G., 1976. Migration of rigid spheres in a two-dimensional unidirectional shear flow of a second-order fluid. *Journal of Fluid Mechanics*, **76**(4), pp.783-799.

[27] Huang, L., Bian, S., Cheng, Y., Shi, G., Liu, P., Ye, X. and Wang, W., 2017. Microfluidics cell sample preparation for analysis: Advances in efficient cell enrichment and precise single cell capture. *Biomicrofluidics*, **11**(1), p.011501.

[28] Huang, P.Y. and Joseph, D.D., 2000. Effects of shear thinning on migration of neutrally buoyant particles in pressure driven flow of Newtonian and viscoelastic fluids. *Journal of non-newtonian fluid mechanics*, **90**(2-3), pp.159-185.

[29] Hur, S.C., Tse, H.T.K. and Di Carlo, D., 2010. Sheathless inertial cell ordering for extreme throughput flow cytometry. *Lab on a Chip*, **10**(3), pp.274-280.

[30] Japper-Jaafar, A., Escudier, M.P. and Poole, R.J., 2010. Laminar, transitional and turbulent annular flow of drag-reducing polymer solutions. *Journal of Non-Newtonian Fluid Mechanics*, **165**(19-20), pp.1357-1372.

[31] Kang, K., Lee, S.S., Hyun, K., Lee, S.J. and Kim, J.M., 2013. DNA-based highly tunable particle focuser. *Nature Communications*, **4**, p.2567.

[32] Karimi, A., Yazdi, S. and Ardekani, A.M., 2013. Hydrodynamic mechanisms of cell and particle trapping in microfluidics. *Biomicrofluidics*, **7**(2), p.021501.

[33] Karnis, A., Goldsmith, H.L. and Mason, S.G., 1963. Axial migration of particles in Poiseuille flow. *Nature*, **200**(4902), p.159.

[34] Karnis, A. and Mason, S.G., 1966. Particle motions in sheared suspensions. XIX. Viscoelastic media. *Transactions of the Society of Rheology*, **10**(2), pp.571-592.

[35] Kim, B. and Kim, J.M., 2016. Elasto-inertial particle focusing under the viscoelastic flow of DNA solution in a square channel. *Biomicrofluidics*, **10**(2), p.024111.

[36] Kim, M.J., Lee, D.J., Youn, J.R. and Song, Y.S., 2016. Two step label free particle separation in a microfluidic system using elasto-inertial focusing and magnetophoresis. *RSC Advances*, **6**(38), pp.32090-32097.

[37] Kung, Y.C., Huang, K.W., Chong, W. and Chiou, P.Y., 2016. Tunnel Dielectrophoresis for Tunable, Single-Stream Cell Focusing in Physiological Buffers in High-Speed Microfluidic Flows. *Small*, **12**(32), pp.4343-4348.

[38] Lapizco-Encinas, B.H., 2019. On the recent developments of insulator-based dielectrophoresis: A review. *Electrophoresis*, **40**(3), pp.358-375.

[39] Leal, L.G., 1979. The motion of small particles in non-Newtonian fluids. *Journal of Non-Newtonian Fluid Mechanics*, **5**, pp.33-78.

[40] Leal, L.G., 1980. Particle motions in a viscous fluid. *Annual Review of Fluid Mechanics*, **12**(1), pp.435-476.

[41] Lee, D.J., Brenner, H., Youn, J.R. and Song, Y.S., 2013. Multiplex particle focusing via hydrodynamic force in viscoelastic fluids. *Scientific Reports*, **3**, p.3258.

[42] Leshansky, A.M., Bransky, A., Korin, N. and Dinnar, U., 2007. Tunable nonlinear viscoelastic “focusing” in a microfluidic device. *Physical Review Letters*, **98**(23), p.234501.

[43] Li, D., Lu, X. and Xuan, X., 2016. Viscoelastic separation of particles by size in straight rectangular microchannels: a parametric study for a refined understanding. *Analytical chemistry*, **88**(24), pp.12303-12309.

[44] Li, D., Zielinski, J., Kozubowski, L. and Xuan, X., 2018. Continuous sheath-free separation of drug-treated human fungal pathogen Cryptococcus neoformans by morphology in biocompatible polymer solutions. *Electrophoresis*, **39**(18), pp.2362-2369.

[45] Li, D. and Xuan, X., 2018. Fluid rheological effects on particle migration in a straight rectangular microchannel. *Microfluidics and Nanofluidics*, **22**(4), p.49.

[46] Li, G., McKinley, G.H. and Ardekani, A.M., 2015. Dynamics of particle migration in channel flow of viscoelastic fluids. *Journal of Fluid Mechanics*, **785**, pp.486-505.

[47] Liang, L., Zhu, J. and Xuan, X., 2011. Three-dimensional diamagnetic particle deflection in ferrofluid microchannel flows. *Biomicrofluidics*, **5**(3), p.034110.

[48] Lim, E.J., Ober, T.J., Edd, J.F., Desai, S.P., Neal, D., Bong, K.W., Doyle, P.S., McKinley, G.H. and Toner, M., 2014. Inertio-elastic focusing of bioparticles in microchannels at high throughput. *Nature communications*, **5**, p.4120.

[49] Lim, H., Nam, J. and Shin, S., 2014. Lateral migration of particles suspended in viscoelastic fluids in a microchannel flow. *Microfluidics and Nanofluidics*, **17**(4), pp.683-692.

[50] Liu, C., Xue, C., Chen, X., Shan, L., Tian, Y. and Hu, G., 2015. Size-based separation of particles and cells utilizing viscoelastic effects in straight microchannels. *Analytical Chemistry*, **87**(12), pp.6041-6048.

[51] Liu, C., Ding, B., Xue, C., Tian, Y., Hu, G. and Sun, J., 2016. Sheathless focusing and separation of diverse nanoparticles in viscoelastic solutions with minimized shear thinning. *Analytical Chemistry*, **88**(24), pp.12547-12553.

[52] Liu, C. and Hu, G., 2017. High-throughput particle manipulation based on hydrodynamic effects in microchannels. *Micromachines*, **8**(3), p.73.

[53] Lu, X., Liu, C., Hu, G. and Xuan, X., 2017. Particle manipulations in non-Newtonian microfluidics: A review. *Journal of colloid and interface science*, **500**, pp.182-201.

[54] Lu, X. and Xuan, X., 2015. Continuous microfluidic particle separation via elasto-inertial pinched flow fractionation. *Analytical Chemistry*, **87**(12), pp.6389-6396.

[55] Lu, X., Zhu, L., Hua, R.M. and Xuan, X., 2015. Continuous sheath-free separation of particles by shape in viscoelastic fluids. *Applied Physics Letters*, **107**(26), p.264102.

[56] Martel, J.M. and Toner, M., 2014. Inertial focusing in microfluidics. *Annual Review of Biomedical Engineering*, **16**, pp.371-396.

[57] Mortazavi, S.A.E.E.D. and Tryggvason, G., 2000. A numerical study of the motion of drops in Poiseuille flow. Part 1. Lateral migration of one drop. *Journal of Fluid Mechanics*, **411**, pp.325-350.

[58] Munaz, A., Shiddiky, M.J. and Nguyen, N.T., 2018. Recent advances and current challenges in magnetophoresis based micro magnetofluidics. *Biomicrofluidics*, **12**(3), p.031501.

[59] Nam, J., Tan, J.K.S., Khoo, B.L., Namgung, B., Leo, H.L., Lim, C.T. and Kim, S., 2015. Hybrid capillary-inserted microfluidic device for sheathless particle focusing and separation in viscoelastic flow. *Biomicrofluidics*, **9**(6), p.064117.

[60] Nilsson, J., Evander, M., Hammarström, B. and Laurell, T., 2009. Review of cell and particle trapping in microfluidic systems. *Analytica Chimica Acta*, **649**(2), pp.141-157.

[61] Novo, P., Dell'Aica, M., Janasek, D. and Zahedi, R.P., 2016. High spatial and temporal resolution cell manipulation techniques in microchannels. *Analyst*, **141**(6), pp.1888-1905.

[62] Poole, R.J. and Escudier, M.P., 2004. Turbulent flow of viscoelastic liquids through an axisymmetric sudden expansion. *Journal of Non-Newtonian Fluid Mechanics*, **117**(1), pp.25-46.

[63] Rodd, L.E., Scott, T.P., Boger, D.V., Cooper-White, J.J. and McKinley, G.H., 2005. The inertio-elastic planar entry flow of low-viscosity elastic fluids in micro-fabricated geometries. *Journal of Non-Newtonian Fluid Mechanics*, **129**(1), pp.1-22.

[64] Romeo, G., D'Avino, G., Greco, F., Netti, P.A. and Maffettone, P.L., 2013. Viscoelastic flow-focusing in microchannels: scaling properties of the particle radial distributions. *Lab on a Chip*, **13**(14), pp.2802-2807.

[65] Sajeesh, P. and Sen, A.K., 2014. Particle separation and sorting in microfluidic devices: a review. *Microfluidics and Nanofluidics*, **17**(1), pp.1-52.

[66] Seo, K.W., Byeon, H.J., Huh, H.K. and Lee, S.J., 2014. Particle migration and single-line particle focusing in microscale pipe flow of viscoelastic fluids. *RSC Advances*, **4**(7), pp.3512-3520.

[67] Seo, K.W., Kang, Y.J. and Lee, S.J., 2014. Lateral migration and focusing of microspheres in a microchannel flow of viscoelastic fluids. *Physics of Fluids*, **26**(6), p.063301.

[68] Segre, G. and Silberberg, A., 1961. Radial particle displacements in Poiseuille flow of suspensions. *Nature*, **189**(4760), p.209.

[69] Roper, M.G., 2015. Cellular analysis using microfluidics. *Analytical chemistry*, **88**(1), pp.381-394.

[70] Song, H.Y., Lee, S.H., Salehiyan, R. and Hyun, K., 2016. Relationship between particle focusing and dimensionless numbers in elasto-inertial focusing. *Rheologica Acta*, **55**(11-12), pp.889-900.

[71] Stoecklein, D. and Di Carlo, D., 2018. Nonlinear microfluidics. *Analytical Chemistry*, **91**(1), pp.296-314.

[72] Takemura, F., Magnaudet, J. and Dimitrakopoulos, P., 2009. Migration and deformation of bubbles rising in a wall-bounded shear flow at finite Reynolds number. *Journal of Fluid Mechanics*, **634**, pp.463-486.

[73] Villone, M.M., D'avino, G., Hulsen, M.A., Greco, F. and Maffettone, P.L., 2013. Particle motion in square channel flow of a viscoelastic liquid: Migration vs. secondary flows. *Journal of Non-Newtonian Fluid Mechanics*, **195**, pp.1-8.

[74] Won, D. and Kim, C., 2004. Alignment and aggregation of spherical particles in viscoelastic fluid under shear flow. *Journal of non-newtonian fluid mechanics*, **117**(2-3), pp.141-146.

[75] Xiang, N., Dai, Q. and Ni, Z., 2016. Multi-train elasto-inertial particle focusing in straight microfluidic channels. *Applied Physics Letters*, **109**(13), p.134101.

[76] Xiang, N., Zhang, X., Dai, Q., Cheng, J., Chen, K. and Ni, Z., 2016. Fundamentals of elasto-inertial particle focusing in curved microfluidic channels. *Lab on a Chip*, **16**(14), pp.2626-2635.

[77] Xiang, N., Ni, Z. and Yi, H., 2018. Concentration-controlled particle focusing in spiral elasto-inertial microfluidic devices. *Electrophoresis*, **39**(2), pp.417-424.

[78] Xuan, X., Zhu, J. and Church, C., 2010. Particle focusing in microfluidic devices. *Microfluidics and Nanofluidics*, **9**(1), pp.1-16.

[79] Yan, S., Zhang, J., Yuan, D. and Li, W., 2017. Hybrid microfluidics combined with active and passive approaches for continuous cell separation. *Electrophoresis*, **38**(2), pp.238-249.

[80] Yang, H. and Gijs, M.A., 2018. Micro-optics for microfluidic analytical applications. *Chemical Society Reviews*, **47**(4), pp.1391-1458.

[81] Yang, S., Kim, J.Y., Lee, S.J., Lee, S.S. and Kim, J.M., 2011. Sheathless elasto-inertial particle focusing and continuous separation in a straight rectangular microchannel. *Lab on a Chip*, **11**(2), pp.266-273.

[82] Yang, S., Lee, S.S., Ahn, S.W., Kang, K., Shim, W., Lee, G., Hyun, K. and Kim, J.M., 2012. Deformability-selective particle entrainment and separation in a rectangular microchannel using medium viscoelasticity. *Soft Matter*, **8**(18), pp.5011-5019.

[83] Yasuda, K.Y., Armstrong, R.C. and Cohen, R.E., 1981. Shear flow properties of concentrated solutions of linear and star branched polystyrenes. *Rheologica Acta*, **20**(2), pp.163-178.

[84] Yuan, D., Zhang, J., Yan, S., Pan, C., Alici, G., Nguyen, N.T. and Li, W.H., 2015. Dean-flow-coupled elasto-inertial three-dimensional particle focusing under viscoelastic flow in a straight channel with asymmetrical expansion–contraction cavity arrays. *Biomicrofluidics*, **9**(4), p.044108.

[85] Yuan, D., Zhao, Q., Yan, S., Tang, S.Y., Alici, G., Zhang, J. and Li, W., 2018. Recent progress of particle migration in viscoelastic fluids. *Lab on a Chip*, **18**(4), pp.551-567.

[86] Zhang, J., Yan, S., Yuan, D., Alici, G., Nguyen, N.T., Warkiani, M.E. and Li, W., 2016. Fundamentals and applications of inertial microfluidics: A review. *Lab on a Chip*, **16**(1), pp.10-34.

[87] Zhang, J., Yan, S., Yuan, D., Zhao, Q., Tan, S.H., Nguyen, N.T. and Li, W., 2016. A novel viscoelastic-based ferrofluid for continuous sheathless microfluidic separation of nonmagnetic microparticles. *Lab on a Chip*, **16**(20), pp.3947-3956.

[88] Zhou, Y., Song, L., Yu, L. and Xuan, X., 2017. Inertially focused diamagnetic particle separation in ferrofluids. *Microfluidics and Nanofluidics*, **21**(1), p.14.

CHAPTER SIX

PARTICLE SEPARATION IN INELSTIC NON-NEWTONIAN FLUIDS

6.1 Abstract

Label-free separation of particles by an intrinsic property can be implemented in microfluidic devices through either an externally imposed field or an inherent flow-induced force. Among the latter type of *passive* techniques, elastic or elasto-inertial lift-based particle separation in non-Newtonian fluids has received a rapidly growing interest in the past decade. However, current demonstrations of particle separation in non-Newtonian fluids have all taken place in viscoelastic polymer or biological solutions. We demonstrate herein for the first time a continuous sheathless separation of polystyrene particles in the flow of inelastic xanthan gum (XG) solution through a simple straight rectangular microchannel. This separation offers a higher throughput and works in a wider range of flow rates than those reported in viscoelastic solutions. We propose to explain the observed particle migrations in XG solutions using the competition of a strong wall-directed (due to the strong shear thinning effect) and a small center-directed (due to the weak elasticity effect) elastic lift component.

6.2 Introduction

Separating particles (e.g., biological cells and synthetic beads) by either an extrinsic label (e.g., fluorescence or magnetic tag) or an intrinsic property (e.g., size, shape or deformability etc.) is important to many biological, chemical, and environmental applications.[1-3] Label-free particle separation has been demonstrated in continuous-flow microfluidic devices through a variety of field-driven techniques, which may be classified as either *active* or *passive* depending on the nature of the involving force.[4-6] *Active* particle separation uses an externally imposed field (e.g., acoustic,[7] electric,[8] magnetic[9] or optical[10]) to generate a force acting on the suspended particles in a fluid flow. This type of techniques is often capable of separating particles at a high resolution with a high specificity but at the cost of limited throughput.[11,12] In contrast, *passive* particle separation exploits the inherent flow-induced hydrodynamic force (e.g., lift or drag) to manipulate particles towards property-dependent equilibrium positions.[13,14] Among this type of techniques, there has been a rapidly growing interest in the use of inertial (in the flow Newtonian fluids)[15-17] and/or elastic (in the flow of non-Newtonian fluids)[18-20] lift for high-throughput label-free separation of particles. Such a nonlinear microfluidic approach is envisioned to have a great potential for the development of future point-of-care devices.[21]

Current demonstrations of particle separation in non-Newtonian fluids have all taken place in polymer solutions or biological fluids that exhibit both viscous and elastic behaviors.[19,20] Among the various polymer solutions, polyethylene oxide (PEO) solution is the most often used that has a medium elasticity with a relatively weak shear thinning effect.[22] PEO-based particle separation can be implemented both with and without a sheath-flow focusing. In the former situation, the mixture of particles is suspended into a PEO solution. Then, if the particle-free sheath fluid is Newtonian (e.g., water), only the larger particles in the mixture are able to migrate across the interface between the two fluids. The smaller particles are still retained inside the PEO solution[23,24] because of the particle size-dependent viscoelastic lift.[25] In contrast, if the sheath fluid uses the same PEO solution as the particle suspension, particles can migrate into it and be deflected towards both size[26,27] and shape[28] dependent lateral positions. Alternatively, the mixture of particles may also be suspended into a Newtonian fluid that is pinched by a particle-free PEO core flow from the middle.[29] This set-up forms two sharp interfaces among the co-flowing fluids that allow for the penetration of the large particles only into the PEO solution.[30,31] PEO-based particle separation has also been implemented without a sheath-flow focusing, where larger particles can be elasto-inertially focused leaving smaller particles dispersed in straight square microchannels.[32,33] In straight rectangular microchannels with a high aspect (width/height) ratio[34-37] or curved microchannels,[38-41] particles are focused towards size and/or shape dependent equilibrium positions.

Two other viscoelastic polymer solutions have also been used for *passive* particle separations. Polyvinylpyrrolidone (PVP) solution is strongly elastic with a negligible shear thinning effect.[32] Its elasticity causes rigid particles to migrate towards either the centerline or the corners, whichever is nearer, in a straight square microchannel when the fluid inertia is negligible.[42] However, the deformability-induced wall lift force[43] can overcome the elastic lift and push soft particles away from the channel corners, leading to a deformability-based particle separation.[42] Under a combined action of elastic and inertial focusing, particles are aligned along the centerline of the cylindrical main-branch in the flow of PVP solution through a two-stage bifurcating microchannel. They are then elasto-inertially displaced away from the sidewall of each rectangular side-branch at a particle-size dependent rate.[44] There is one other report of particle separation using polyacrylamide

(PAA) solution that is strongly viscoelastic and strongly shear thinning exhibiting the second normal stress difference.[45] Small particles that are suspended in an off-center focused PAA solution are carried towards the channel walls by the second normal stress difference-induced secondary flow[46] while large particles remain inside the focused PAA solution.

In addition, a couple of viscoelastic biological fluids have been demonstrated for the *passive* separation of particles. One of them is the hyaluronic acid (HA) solution that has strong viscoelasticity and shear thinning.[47] It can be used to replace the PVP solution, as noted above,[44] for sheathless particle focusing and separation in the cylindrical main-branch and rectangular side-branches, respectively, of a bifurcating microchannel. As the viscosity of the HA solution is two orders of magnitude smaller than that of the PVP solution, the pumping pressure and as well the shear stress on bioparticles can be substantially reduced.[48] The HA solution has also been used for high throughput malaria parasite separation in a revised bifurcating microchannel, where the first-stage cylindrical capillary is replaced by a slit-like rectangular microchannel so that the whole channel can be fabricated in one layer.[49] Moreover, the combined fluid elasticity and shear thinning effects of HA solution enable a sheath-free separation of particles by size in both a straight square[50] and a straight rectangular microchannel with a large width to height ratio.[51] The other biological fluid is DNA solution that is strongly viscoelastic because of the long relaxation time of DNA molecules. An extremely dilute DNA solution (5 ppm, at which the shear thinning effect is negligible) has been demonstrated to significantly improve the sheath-flow separation of multiple types of particles by size in a straight square microchannel.[52]

In a recent study, the authors of this work observed in a straight rectangular microchannel the lateral migration of rigid spherical particles in the flow of xanthan gum (XG) solution that is strongly shear thinning with little elasticity.[53] The particle equilibrium positions in the XG solution are different from those in both a Newtonian fluid and any of the viscoelastic polymer[53] or biological solutions as noted above. Moreover, their locations are found to be a strong function of particle size,[54] which implies a potentially high throughput separation of particles in the flow of XG solutions through a straight rectangular microchannel. The aim of this work is to demonstrate the feasibility of such a continuous-flow sheathless label-free separation in inelastic non-Newtonian fluids using both a binary and a ternary mixture of polystyrene particles. A comprehensive experimental study is also performed for the effects of multiple parameters, including the flow rate, XG concentration and channel depth, on the binary particle separation.

6.3 Experiment

XG solutions were prepared by dissolving XG powders (Tokyo Chemical Industry) into deionized water (Fisher Scientific) at 1000 ppm, 2000 ppm and 3000 ppm, respectively. Their viscosities, η, were measured using a cone-plate rheometer (Anton Paar, MCR 302) in a wide range of shear rates at 23 °C (Fig. 6.1), which are found comparable to the reported data in Japper-Jaafar et al.[56] We used the Carreau-Yasuda model[55] to fit with the measured viscosity values in Fig. 6.1,

$$\frac{\eta-\eta_\infty}{\eta_0-\eta_\infty} = [1 + (\lambda_{CY}\bar{\dot{\gamma}})^a]^{(n-1)/a} \tag{6-1}$$

where η_∞ is the infinite-shear-rate viscosity, η_0 is the zero-shear-rate viscosity, λ_{CY} is a time constant, $\bar{\dot{\gamma}} = 2V/w$ is the average fluid shear rate across the microchannel width, w, with V being the average fluid velocity, a is a fitting parameter, and n is the power-law index. Table 6.1 presents the fitting values of the parameters in Eq. (6-1) for the three prepared XG solutions, which are all strongly shear thinning with the power-law index, n, decreasing at a higher concentration. Three types of spherical polystyrene particles were used in the experiment: 5 µm red fluorescent particles (Magsphere), 10 µm green fluorescent particles (Thermo Scientific) and 15 µm plain particlkes (Sigma-Aldrich). The latter two particles were mixed and re-suspended in XG solutions (to a final concentration of $10^6 - 10^7$ particles per milliliter each) for most of the tests. They were also mixed and re-suspended into water for a control experiment. All three particles were mixed and re-suspended in 2000 ppm XG solution for a demonstration of ternary particle separation.

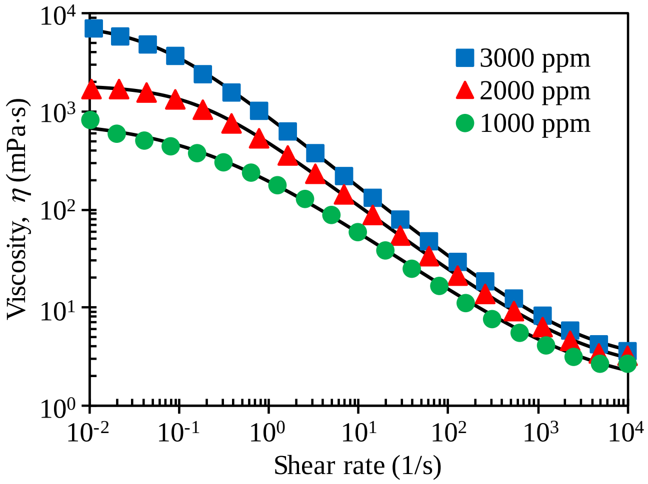

Fig. 6.1. Experimentally measured (symbols) and theoretically fitted (lines, via the Carreau-Yasuda model[55]) viscosity data of the prepared XG solutions.

Table 6.1. Summary of the parameters in the Carreau-Yasuda model[55] (refer to Eq. (6-1)) for the definitions of symbols) for fitting with the experimentally measured viscosity data (Figure 6.1) of the prepared XG solutions.

XG concentration	n	η_0 (Pa•s)	η_∞ (Pa•s)	λ_{CY} (s)	a
1000 ppm	0.36	0.82	1.55×10^{-3}	5.62	0.57
2000 ppm	0.32	1.87	2.10×10^{-3}	6.62	1.02
3000 ppm	0.28	8.00	2.64×10^{-3}	20.00	0.94

Microchannels were fabricated with polydimethylsiloxane (PDMS) using the standard soft lithography technique as described elsewhere.[57] They were each measured 65 µm wide and 2 cm long while the depth was varied from 20 µm to 30 µm and 54 µm for the study of channel aspect ratio effect. At each end of the microchannels there was an expansion of 900 µm wide for enhanced particle separation and visualization (Fig. 6.2 (a)). A syringe pump (KD Scientific) was used to drive particle solutions through microchannels with the volume flow rate spanning from 0.1 mL/h to 6.0 mL/h. The motion of particles was recorded through an inverted fluorescent microscope (Nikon Eclipse TE2000U, Nikon Instruments) with a CCD camera (Nikon DS-Qi1Mc). Fluorescent and bright field illuminations were used simultaneously in order to visualize both fluorescent (appearing bright or fluorescent if a color filter was in use) and plain (appearing dark) particles. Superimposed particle images were obtained using Nikon image software (NIS-Elements) by stacking video frames with the maximum and minimum intensity projections for fluorescent and plain particles, respectively. Composite images were obtained by laying the superimposed image of plain particles over that of fluorescent ones after removing the background of the former. The probability distribution function (PDF) of each type of particles at the outlet expansion was analyzed using ImageJ software (National Institute of Health) and plotted in Microsoft Excel®.

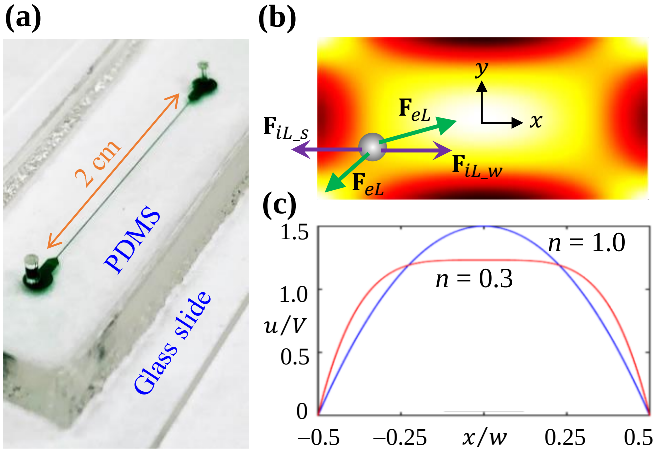

Figu. 6.2. (a) Isometric view of the fabricated microchannel in PDMS. (b) Schematic illustration of the elastic ($\mathbf{F}_{eL}$) and inertial ($\mathbf{F}_{iL}$) lift forces acting on a particle in the flow of inelastic shear-thinning fluids through a straight rectangular microchannel with an aspect ratio, $AR = 2.2$, where the background color shows the contour of fluid shear rate, $\dot{\gamma}$ (the darker the larger magnitude), at $n = 0.3$. (c) Widthwise profile of the flow velocity (scaled by the average fluid velocity, V) for Newtonian and shear-thinning fluids.

6.4 Theory

Rigid particles experience both elastic and inertial lift forces in confined flows of non-Newtonian fluids.[58,59] The elastic lift, $\mathbf{F}_{eL}$, results from the non-uniform normal stress differences in the channel cross-section,[60] and is often assumed proportional to the variation of the first normal stress difference, N_1, over the size of the particle in polymer solutions,[61]

$$\mathbf{F}_{eL} \sim d^3 \nabla N_1 \tag{6-2}$$

where d is the particle diameter. Like other diluted solutions of high molecular weight polymers,[62] N_1 of XG solutions, though small, also exhibits a power-law behavior,[63,64] $N_1 = A\dot{\gamma}^m$, where A and m are both fluid-dependent constants. Thus, Eq. (6-2) is rewritten as

$$\mathbf{F}_{eL} \sim d^3 A \nabla \dot{\gamma}^m \tag{6-3}$$

As schematically illustrated in Fig. 6.1 (b), $\mathbf{F}_{eL}$ directs particles towards the low shear rate region, i.e., the center and four corners of the channel cross-section. The inertial lift, $\mathbf{F}_{iL}$, results from the fluid inertia and can be conveniently broken down into two components (Fig. 6.2 (b)), where the wall-induced inertial lift, $\mathbf{F}_{iL\_w}$, pushes particles away from any channel walls while the shear gradient-induced inertial lift, $\mathbf{F}_{iL\_s}$, directs particles towards the center of each face of the microchannel.[65] The total inertial lift scales as,[66]

$$\mathbf{F}_{iL} = \mathbf{F}_{iL\_w} + \mathbf{F}_{iL\_s} \sim \rho d^4 \dot{\gamma}^2 / D_h^2 \tag{6-4}$$

where ρ is the fluid density, and D_h is the hydraulic diameter of the microchannel.

As they are each a strong function of the local shear rate, $\dot{\gamma}$, the elastic and inertial lift forces are both affected by the fluid velocity profile that varies significantly with the power-law index (Fig. 6.2 (c)). Therefore, the equilibrium particle positions in the flow of inelastic shear-thinning XG solutions through straight rectangular microchannels are expected to be different from those in viscoelastic solutions. The flow rate (or in turn the shear rate) effect on particle separation is studied in terms of the (channel) Reynolds number,

$$Re = \frac{\rho V D_h}{\eta} = \frac{2\rho Q}{\eta(\bar{\dot{\gamma}})(w+h)} \tag{6-5}$$

where $\eta(\bar{\dot{\gamma}})$ is the fluid viscosity estimated via Eq. (6-1) using the average fluid shear rate, $\bar{\dot{\gamma}}$, across the channel width, Q is the volumetric flow rate, and h is the channel depth. The shear thinning effect on particle separation is studied in terms of the power-law index, n, which is directly related to the XG concentration. The particle size effect is studied in terms of the confinement ratio,

$$\beta = d/D_h \tag{6-6}$$

and the channel depth effect is studied in terms of the aspect ratio,

$$AR = w/h \tag{6-7}$$

6.5 Results and discussion

6.5.1 Binary particle separation

Fig. 6.3 demonstrates a continuous separation of 10 µm (fluorescent) and 15 µm (plain) particles in the flow of 2000 ppm XG solution through a 65 µm wide and 30 µm deep straight rectangular microchannel (i.e., aspect ratio, $AR = 2.2$). The flow rate is 2.0 mL/h with a calculated $Re = 3.7$. Both types of particles travel into the microchannel randomly and uniformly as viewed from the snapshot image at the channel inlet. They, however, travel out of the channel along different flow paths, where 15 µm particles tightly line each sidewall leaving almost all 10 µm particles in the bulk of the channel expansion with no apparent equilibrium positions. Such a size-based sheathless particle separation does not take place in a Newtonian fluid (see Fig. B-1 of Appendix B) or a viscoelastic non-shear-thinning PVP solution, where the large and small particles both migrate towards the centerline of a straight rectangular microchannel with a high AR.[36] This separation is different from that in the flow of viscoelastic and weakly shear-thinning PEO solution, where the larger particles migrate towards two off-center equilibrium positions while the smaller ones stay between them in either a single stream along the centerline [34] or dual near-center streams.[35,36] It is also different from that in the flow of strongly shear-thinning and strongly viscoelastic HA solution, where in a straight square microchannel the larger particles migrate towards the channel centerline and the smaller ones migrate towards the vicinity of the walls.[50] In a straight rectangular microchannel with $AR = 2.0$, however, the particles' behaviors in HA solutions[51] become similar to those in PEO solutions.[35,36]

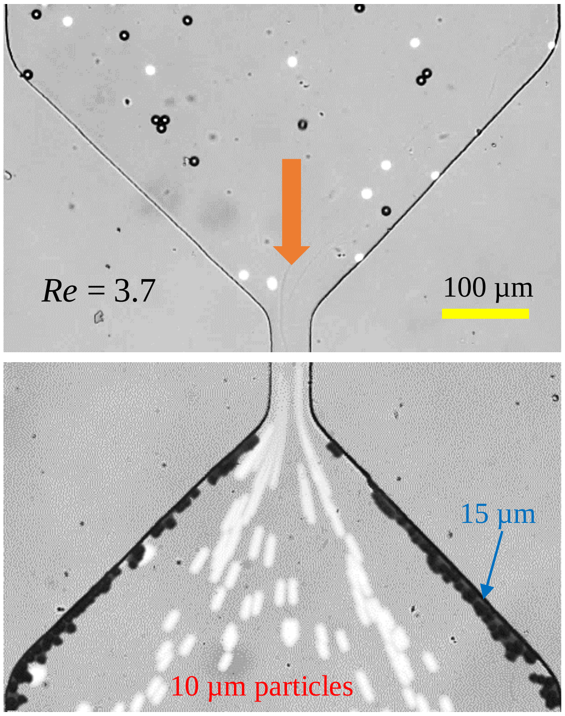

Fig. 6.3. Continuous sheath-free separation of 10 μm fluorescent (bright) and 15 μm plain (black) particles in 2000 ppm XG solution through a 65 μm wide and 30 μm deep microchannel at a flow rate of 2.0 mL/h (upper panel: snapshot image at the channel inlet; lower panel: composite image at the channel outlet). The block arrow indicates the flow direction.

6.5.2 Effect of flow rate

Fig. 6.4 (a) shows the composite images of 10 μm and 15 μm particles in 2000 ppm XG solution at the outlet expansion of a 30 μm deep microchannel under varying flow rates (see the original superimposed images of each type of particles in Fig. B-2 of Appendix B). Under the flow rate of 0.1 mL/h, the impact of inertial focusing is negligible because of the very small value of $Re = 0.05$. The consequence of elastic focusing alone is to direct particles towards the center and corners of the channel cross-section (Fig. 5.2 (b)), the migration of which is, however, found sensitive to particle size in our experiment. Specifically, the majority of 15 μm particles travel adjacent to the channel walls leaving very few scattered in the bulk. In contrast, most of 10 μm particles are focused into a tight stream along the channel centerline while the remainder stays close to the channel walls. Increasing the flow rate to 0.4 mL/h ($Re = 0.4$) completely depletes 15 μm particles from the bulk of the microchannel, and meanwhile broadens the stream of 10 μm particles around the channel centerline. Further increasing the flow rate causes a displacement of 10 μm particles from the middle of the central stream to its edges. This movement eventually leads to a split of the central stream into two sub-streams at 4.0 mL/h ($Re = 8.5$), whose positions each shift further towards the walls when the flow rate is increased to 6.0 mL/h. As they remain retained near the channel walls (or more specifically, within the channel corners as illustrated in Fig. 5.2 (b)) in the whole range of flow rates in Fig. 5.4 (a), 15 μm particles can be continuously separated from 10 μm particles in a wide range of flow rates.

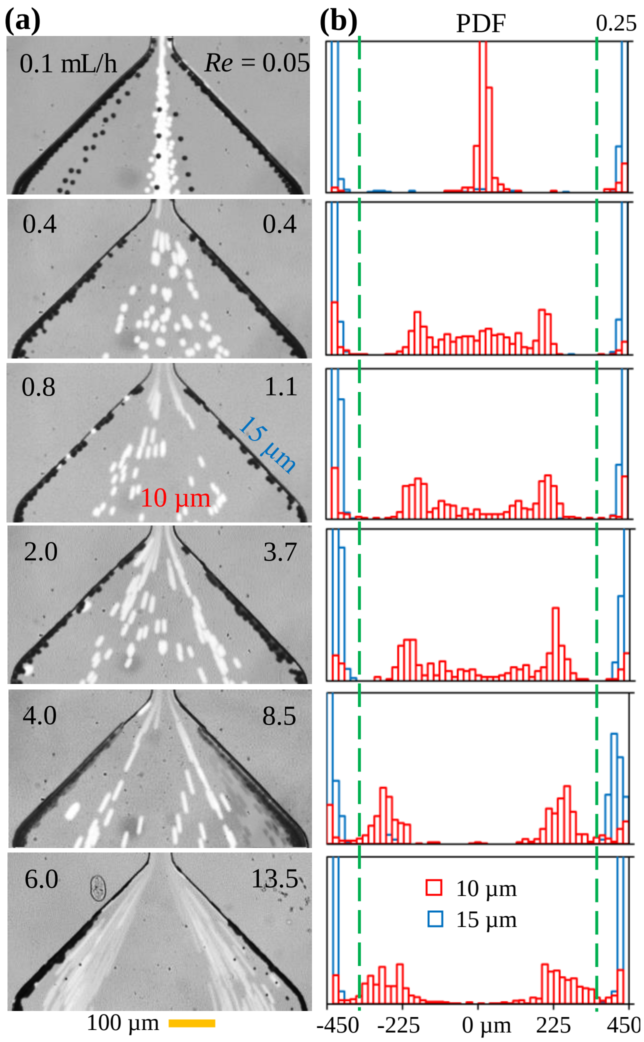

Fig. 6.4. Flow rate effect on the separation of 10 µm (bright) and 15 µm (dark) particles in 2000 ppm XG solution in a 65 µm wide and 30 µm deep rectangular microchannel: composite images (left) and particle PDF plots (right). The values of the experimentally imposed flow rate and the calculated *Re* are both labeled on the images (left). The two dashed lines on the PDF plots (right), which are each 100 µm away from the channel walls at the 900 µm-wide expansion region, divide the outlet expansion of the microchannel into the inner (for 10 µm particles) and outer (for 15 µm particles) zones for estimating the separation efficiency and purity of the two types of particles.

We also did a control experiment in DI water in the same microchannel, and found that 10 µm and 15 µm particles are both focused towards the channel center through at different extents (see Figure B-1 in Appendix B). This inertial focusing of particles is consistent with previous studies in straight rectangular microchannels with a high aspect ratio.[36,67] We therefore judge that the elastic lift, $\mathbf{F}_{eL}$, in 2000 ppm XG solution should dominate the inertial lift, $\mathbf{F}_{iL}$, in the range of flow rates under test. Otherwise, either type of particles should exhibit an inward shift with the increase of flow rate. Referring to our earlier work on particle separation in PEO solutions,[36] we propose to break down $\mathbf{F}_{eL}$ in XG solutions into two similar competing components: $\mathbf{F}_{eL\rightarrow c}$ directs particles towards the channel centerline and is small because of the weak elasticity of XG solutions; $\mathbf{F}_{eL\rightarrow w}$ directs particles towards the channel walls and is large because of the strong shear-thinning of XG solutions.[68-70] The particle behaviors in Fig. 6.4 (a) indicates that $\mathbf{F}_{eL\rightarrow w}$ is a stronger positive function of both particle size and fluid flow rate than $\mathbf{F}_{eL\rightarrow c}$, which appears consistent with the scaling of these two elastic lift components in PEO solutions in our earlier work.[36]

Fig. 6.4 (b) shows the PDF plots of 10 μm and 15 μm particles for a quantitative comparison of their exiting positions at the channel outlet under varying flow rates, which were obtained directly from analyzing the particle images in Fig. 6.4 (a). Note that the vertical axis in every plot has been limited to no more than 0.25 such that the PDF of 10 μm particles can be visually identified in the whole range of flow rates. The highest PDF value of 15 μm particles is actually greater than 0.3 in all plots. There is a clear separation between the two types of particles throughout the range of flow rates despite of a small overlapping near the channel walls. We employ two metrics to evaluate this separation performance, which are the separation efficiency and purity as defined below,[36]

$$efficiency = \frac{number\ of\ targeted\ particles\ inside\ a\ specific\ zone}{total\ number\ of\ targeted\ particles} \qquad (6\text{-}8)$$

$$purity = \frac{number\ of\ targeted\ particles\ inside\ a\ specific\ zone}{total\ number\ of\ particles\ inside\ the\ same\ specific\ zone} \qquad (6\text{-}9)$$

In the calculation, the 900 µm-wide outlet expansion was split into the inner zone for 10 µm particles and the outer zone for 15 µm particles. The two division lines, as marked on the PDF plots in Fig. 6.4 (b), are each 100 µm away from the nearby channel walls.

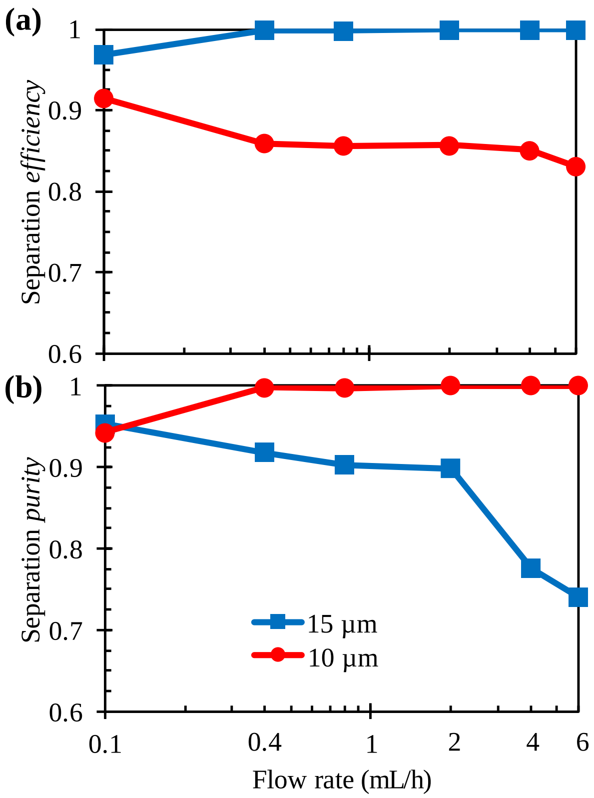

Fig. 6.5. Plots of the separation efficiency (a) and purity (b) for 10 µm and 15 µm particles in the flow of 2000 ppm XG solution through a 65 µm wide and 30 µm deep rectangular microchannel (determined from the PDF plots in Fig. 6.4 (b)).

Fig. 6.5 shows the obtained plots of the two separation metrics for each type of particles. The separation efficiency of 15 µm particles in the outer zone is 100% except at the lowest flow rate of 0.1 mL/h (which is also 97%). In contrast, the separation efficiency of 10 µm particles in the inner zone is 92% at 0.1 mL/h and remains at roughly 85% from 0.4 to 6.0 mL/h. On the contrary, the separation purity of 10 µm particles in the inner zone is 100% except at 0.1 mL/h because all 15 µm particles stay within the outer zone. The separation purity of 15 µm particles gradually reduces from 95% at 0.1 mL/h to 90% at 2.0 mL/h. It, however, drops rapidly to 78% at 4.0 mL/h because of the split of the central 10 µm particle stream into two near-wall sub-streams and further drops to 74% at 6.0 mL/h. It is, however, important to note the separation purity of 15 µm particles may be significantly biased by its relative total number to that of 10 µm particles. It is therefore safe to say that the two types of particles can be effectively separated in the flow rate spanning from 0.1 mL/h to at least 4.0 mL/h. This range spans nearly two orders of magnitude (precisely, 1.6 orders of magnitude) and is wider than those reported in viscoelastic solutions.[35,36,50]

6.5.3 Effect of XG concentration

Fig. 6.6 shows the effect of XG concentration on the separation of 10 µm and 15 µm particles in a 30 µm deep microchannel under three selected flow rates: 0.1, 0.8 and 4.0 mL/h (see the particle images in a full range of flow rates in Figures B-3 and B-4 of Appendix B). In 1000 ppm XG solution, nearly all 15 µm particles line the channel walls at the outlet expansion as seen from both the top-view images (Fig. 6.6 (a)). Moreover, an apparently greater number of 10 µm particles than that in 2000 ppm XG solution (Fig. 6.4) appear adjacent the channel walls. These phenomena seem to suggest that the wall-directed elastic lift component, $\mathbf{F}_{eL\rightarrow w}$, has a weaker dependence on the XG concentration than the center-directed one, $\mathbf{F}_{eL\rightarrow c}$, and hence decreases to a lesser extent in a lower-concentration XG solution. This judge is further supported by the observation in 3000 ppm XG solutions, where 15 μm particles find an additional equilibrium position along the channel centerline (other than those near the walls, see Fig. 6.4) at 0.1 mL/h because of the greater increase in $\mathbf{F}_{eL\rightarrow c}$ than $\mathbf{F}_{eL\rightarrow w}$ in a higher-concentration XG solution. This 15 μm particle central stream spreads and disappears with the increase of flow rate as a result of the quicker increase of $\mathbf{F}_{eL\rightarrow w}$. The central stream of 10 μm particles also spreads when the flow rate increases, similar to the observation in Fig. 6.4. Moreover, it splits into two near-wall sub-streams, for which the flow rate increases rapidly with the increase of XG concentration due to the stronger impact of $\mathbf{F}_{eL\rightarrow c}$. Specifically, the occurrence of dual near-wall particle streams takes place at 0.6 mL/h in 1000 ppm XG solution as compared to 4.0 mL/h in 2000 ppm XG solution (Fig. 6.4). No division of the 10 μm particle central stream was observed in 3000 ppm XG solution for flow rates up to 6.0 ml/h. Overall, the separation of 10 μm and 15 μm particles gets worse when the XG concentration either increases or decreases from 2000 ppm.

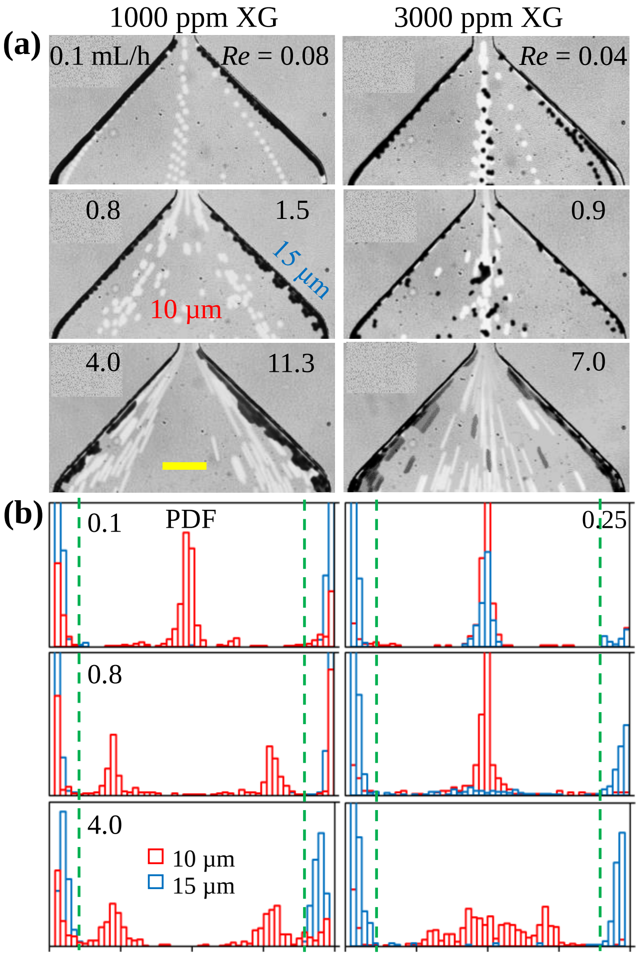

Fig. 6.6. Effect of XG concentration (left column, 1000 ppm; right column, 3000 ppm) on the separation of 10 µm (bright) and 15 µm (dark) particles in a straight 65 µm wide and 30 µm deep rectangular microchannel under selected flow rates: (a) Composite images at the channel outlet with the values of flow rate and *Re* being both labeled; (b) Corresponding particle PDF plots where the two dashed lines (as defined in Fig. 6.4 (b)) divide the outlet expansion into the inner and outer zones for 10 µm and 15 µm particles, respectively. The scale bar in (a) represents 100 µm.

6.5.4 Effect of channel depth

Fig. 6.7 shows the composite images of 10 µm and 15 µm particles in 2000 ppm XG solution at the outlet expansion of 20 µm ($AR = 3.3$) and 54 µm ($AR = 1.2$) deep channels, respectively. Three flow rates, 0.1, 0.8 and 4.0 mL/h, are selected for the illustration. In the shallower 20 µm deep channel, both types of particles line up along the walls at the flow rate of 0.1 mL/h (Fig. 6.7 (a)). These equilibrium positions do not vary for 15 µm particles for flow rates of up to 6.0 mL/h (see the particle images in a full range of flow rates in Fig. B-5 of Appendix B). In contrast, the exiting positions of 10 µm particles expand inward while still remaining adjacent to the channel walls in the whole range of flow rates under test. These phenomena may be attributed to two concurrent actions. One is the more quickly reduced elastic lift component, $\mathbf{F}_{eL\rightarrow c}$, than $\mathbf{F}_{eL\rightarrow w}$ in a shallower microchannel, which causes the equilibrium particle position along the channel center to disappear. And the other is the enhanced inertial lift, $\mathbf{F}_{iL}$, which, though still weaker than $\mathbf{F}_{eL\rightarrow w}$ of 15 µm particles, may become comparable to that of 10 µm particles and hence shift them away from the channel walls when the flow rate increases. On the contrary, the elastic lift component, $\mathbf{F}_{eL\rightarrow c}$, increases faster than $\mathbf{F}_{eL\rightarrow w}$ in a deeper microchannel, leading to the formation of equilibrium positions at both the centerline and walls for both 10 µm and 15 µm particles in the 54 µm deep channel (Fig. 6.7 (b)). Moreover, similar to the observation in 3000 ppm XG solution (Fig. 6.6 (b)), the central stream of each type of particles broadens when the flow rate increases. However, only that of 15 µm particles is observed to first split into triple sub-streams at 0.8 mL/h and then dual near-wall sub-streams at 4.0 mL/h (see the particle images in a full range of flow rates in Fig. B-6 of Appendix B). Therefore, no good separation is achieved in the 20 µm or 54 µm deep channels.

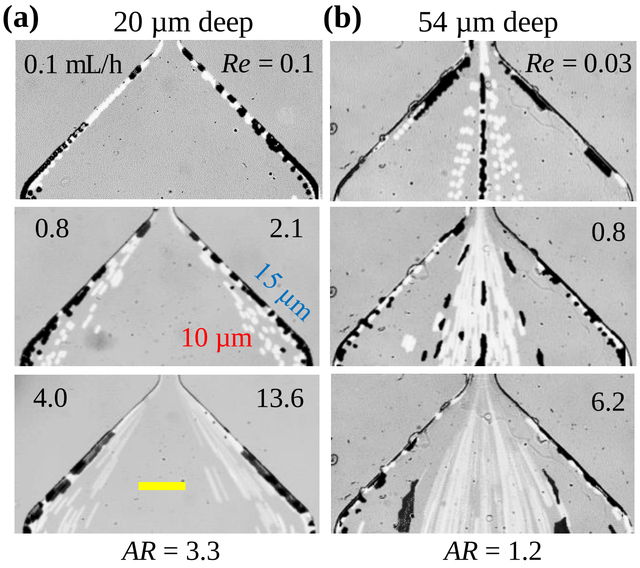

Fig. 6.7. Effect of channel depth (and hence the aspect ratio, AR) on the separation of 10 µm (bright) and 15 µm (dark) particles in 2000 ppm XG solution through a straight 65 µm wide rectangular microchannel under selected flow rates: (a) 20 µm deep with $AR = 3.3$; (b) 54 µm deep with $AR = 1.2$. The scale bar represents 100 µm.

6.5.5 Ternary particle separation

Fig. 6.8 demonstrates a separation of 5 µm, 10 µm and 15 µm particles in 2000 ppm XG solution through a 30 µm deep channel at the flow rate of 4.0 mL/h (see the particle images in a full range of flow rates in Fig. B-7 of Appendix B). The stronger dependence of $\mathbf{F}_{eL\rightarrow w}$ on particle size than $\mathbf{F}_{eL\rightarrow c}$, causes an inward shift of the equilibrium positions of particles when they get smaller. This explains why 5 µm particles form a relatively wide band around the channel centerline leaving a small portion of them near the walls (Fig. 6.8 (b)). Moreover, consistent with the binary separation of 10 µm and 15 µm particles at 4.0 mL/h in Fig. 6.3, the majority of 10 µm particles stay at the two near-wall equilibrium positions while 15 µm particles still line the channel walls (Fig. 6.8 (a)). To evaluate the performance of this ternary separation from the particle PDF plot in Fig. 6.8 (c), we divide the outlet expansion into the inner, middle and outer zones for estimating the separation purity and efficiency of 5 µm, 10 µm and 15 µm particles, respectively. The two division lines between the middle and outer zones are still the same as those in Fig. 6.4 for the binary particle separation. Those between the middle and inner zones are each set to 150 µm off the channel centerline. The calculated separation metrics for the three types of particles are presented in Table 6.2. The separation efficiency has the lowest value of 73% for 10 µm particles in the middle zone. The separation purity has the lowest value of 68% for 15 µm particles in the outer zone because of the occurrence of both 5 µm and 10 µm particles near the channel walls. It is, however, important to note again that the separation purity of the two larger particles may be significantly biased by their relative total numbers to that of 5 µm particles.

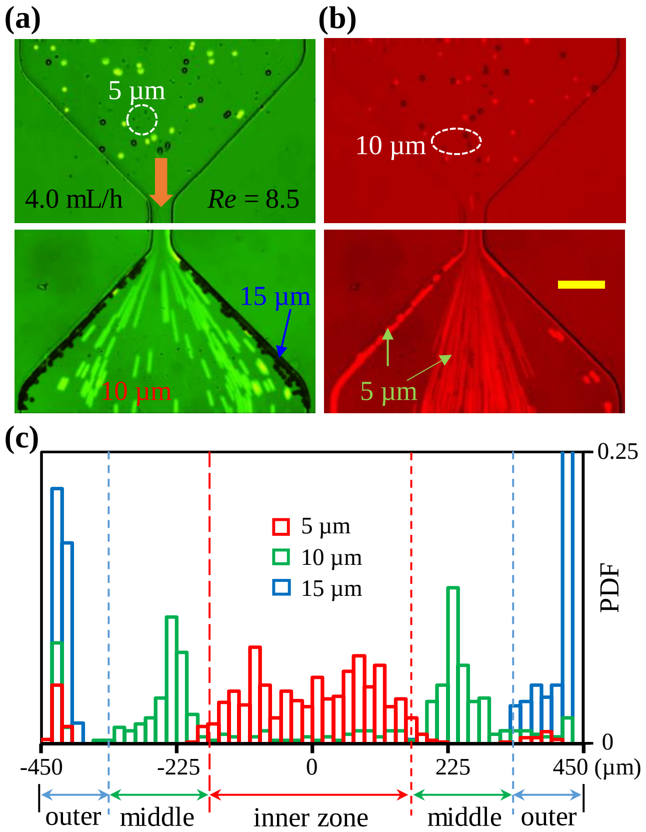

Fig. 6.8. Separation of 5 μm (red fluorescent), 10 μm (green fluorescent) and 15 μm (plain) spherical particles in 2000 ppm XG solution through a straight 65 μm wide and 30 μm deep rectangular microchannel at a flow rate of 4.0 mL/h: (a) snapshot image of all three types of particles at the channel inlet and composite image of 10 μm/15 μm particles at the channel outlet (both with a green filter); (b) snapshot image of all three types of particles at the channel inlet and superimposed image of 5 μm particles at the channel outlet (both with a red filter); (c) particle PDF plot where the dashed lines divide the outlet expansion into the inner, middle and outer zones for estimating the separation efficiency and purity of 5 μm, 10 μm and 15 μm particles, respectively. The scale bar on the image in (b) represents 100 μm.

Table 6.2. Estimated efficiency and purity of the ternary particle separation in Fig. 6.7

particles	number counts	collecting zone	efficiency (%)	purity (%)
5 μm	761	inner zone	80	94
10 μm	359	middle zone	73	75
15 μm	279	outer zone	99	68

6.6 Conclusions

We have demonstrated for the first time that rigid spherical particles can be continuously separated by size in the flow of inelastic XG solutions through straight rectangular microchannels. This sheath- and label-free particle separation results from the differential elastic focusing in XG solutions, where the larger particles line the channel walls while the smaller ones travel in the bulk of the microchannel. These particle migrations are different from those reported in viscoelastic solutions because of the unique non-Newtonian rheology of XG solutions, i.e., strongly shear thinning with little elasticity. We have also performed a comprehensive parametric study of the effects of flow rate, XG concentration, and channel depth on particle separation in XG solutions. Moreover, we have proposed to break down the elastic lift into a weak center-directed component because of to the weak elasticity of XG solutions and a strong wall-directed component because of the strong shear thinning of XG solutions. The competition of these two elastic lift components, which is similar to that in our earlier work on particle separation in PEO solutions,[36] explains qualitatively the observed shifting of particle focusing positions in the parametric study. We wish this work along with our recent one[54] would stimulate theoretical or numerical studies on particle motion in the flow of inelastic non-Newtonian fluids through microchannels.

Acknowledgements This work was supported in part by Clemson University through a SEED grant (XX).

References

[1] Gossett, D.R., Weaver, W.M., Mach, A.J., Hur, S.C., Tse, H.T.K., Lee, W., Amini, H. and Di Carlo, D., 2010. Label-free cell separation and sorting in microfluidic systems. *Analytical and Bioanalytical Chemistry*, **397**(8), pp.3249-3267.

[2] Shields IV, C.W., Reyes, C.D. and López, G.P., 2015. Microfluidic cell sorting: a review of the advances in the separation of cells from debulking to rare cell isolation. *Lab on a Chip*, **15**(5), pp.1230-1249.

[3] Sibbitts, J., Sellens, K.A., Jia, S., Klasner, S.A. and Culbertson, C.T., 2017. Cellular analysis using microfluidics. *Analytical Chemistry*, **90**(1), pp.65-85.

[4] Karimi, A., Yazdi, S. and Ardekani, A.M., 2013. Hydrodynamic mechanisms of cell and particle trapping in microfluidics. *Biomicrofluidics*, **7**(2), p.021501.

[5] Sajeesh, P. and Sen, A.K., 2014. Particle separation and sorting in microfluidic devices: a review. *Microfluidics and Nanofluidics*, **17**(1), pp.1-52.

[6] Tang, W., Jiang, D., Li, Z., Zhu, L., Shi, J., Yang, J. and Xiang, N., 2019. Recent advances in microfluidic cell sorting techniques based on both physical and biochemical principles. *Electrophoresis*, **40**(6), pp.930-954.

[7] Laurell, T., Petersson, F. and Nilsson, A., 2007. Chip integrated strategies for acoustic separation and manipulation of cells and particles. *Chemical Society Reviews*, **36**(3), pp.492-506.

[8] Lapizco-Encinas, B.H., 2019. On the recent developments of insulator-based dielectrophoresis: A review. *Electrophoresis*, **40**(3), pp.358-375.

[9] Hejazian, M., Li, W. and Nguyen, N.T., 2015. Lab on a chip for continuous-flow magnetic cell separation. *Lab on a Chip*, **15**(4), pp.959-970.

[10] Kim, S.B., Yoon, S.Y., Sung, H.J. and Kim, S.S., 2008. Cross-type optical particle separation in a microchannel. *Analytical Chemistry*, **80**(7), pp.2628-2630.

[11] Tsutsui, H. and Ho, C.M., 2009. Cell separation by non-inertial force fields in microfluidic systems. *Mechanics Research Communications*, **36**(1), pp.92-103.

[12] Yan, S., Zhang, J., Yuan, D. and Li, W., 2017. Hybrid microfluidics combined with active and passive approaches for continuous cell separation. *Electrophoresis*, **38**(2), pp.238-249.

[13] Di Carlo, D., 2009. Inertial microfluidics. *Lab on a Chip*, **9**(21), pp.3038-3046.

[14] Liu, C. and Hu, G., 2017. High-throughput particle manipulation based on hydrodynamic effects in microchannels. *Micromachines*, **8**(3), p.73.

[15] Martel, J.M. and Toner, M., 2014. Inertial focusing in microfluidics. *Annual review of biomedical engineering*, **16**, pp.371-396.

[16] Amini, H., Lee, W. and Di Carlo, D., 2014. Inertial microfluidic physics. *Lab on a Chip*, **14**(15), pp.2739-2761.

[17] Zhang, J., Yan, S., Yuan, D., Alici, G., Nguyen, N.T., Warkiani, M.E. and Li, W., 2016. Fundamentals and applications of inertial microfluidics: A review. *Lab on a Chip*, **16**(1), pp.10-34.

[18] D'Avino, G., Greco, F. and Maffettone, P.L., 2017. Particle migration due to viscoelasticity of the suspending liquid and its relevance in microfluidic devices. *Annual Review of Fluid Mechanics*, **49**, pp.341-360.

[19] Lu, X., Liu, C., Hu, G. and Xuan, X., 2017. Particle manipulations in non-Newtonian microfluidics: A review. *Journal of Colloid and Interface Science,* **500**, pp.182-201.

[20] Yuan, D., Zhao, Q., Yan, S., Tang, S.Y., Alici, G., Zhang, J. and Li, W., 2018. Recent progress of particle migration in viscoelastic fluids. *Lab on a Chip*, **18**(4), pp.551-567.

[21] Stoecklein, D. and Di Carlo, D., 2018. Nonlinear microfluidics. *Analytical Chemistry*, **91**(1), pp.296-314.

[22] Rodd, L.E., Scott, T.P., Boger, D.V., Cooper-White, J.J. and McKinley, G.H., 2005. The inertio-elastic planar entry flow of low-viscosity elastic fluids in micro-fabricated geometries. *Journal of Non-Newtonian Fluid Mechanics*, **129**(1), pp.1-22.

[23] Ha, B., Park, J., Destgeer, G., Jung, J.H. and Sung, H.J., 2016. Transfer of microparticles across laminar streams from non-Newtonian to Newtonian fluid. *Analytical Chemistry*, **88**(8), pp.4205-4210.

[24] Yuan, D., Tan, S.H., Sluyter, R., Zhao, Q., Yan, S., Nguyen, N.T., Guo, J., Zhang, J. and Li, W., 2017. On-chip microparticle and cell washing using coflow of viscoelastic fluid and newtonian fluid. *Analytical Chemistry*, **89**(17), pp.9574-9582.

[25] Yuan, D., Zhang, J., Yan, S., Peng, G., Zhao, Q., Alici, G., Du, H. and Li, W., 2016. Investigation of particle lateral migration in sample-sheath flow of viscoelastic fluid and Newtonian fluid. *Electrophoresis*, **37**(15-16), pp.2147-2155.

[26] Nam, J., Lim, H., Kim, D., Jung, H. and Shin, S., 2012. Continuous separation of microparticles in a microfluidic channel via the elasto-inertial effect of non-Newtonian fluid. *Lab on a Chip*, **12**(7), pp.1347-1354.

[27] Lu, X. and Xuan, X., 2015. Continuous microfluidic particle separation via elasto-inertial pinched flow fractionation. *Analytical Chemistry*, **87**(12), pp.6389-6396.

[28] Lu, X. and Xuan, X., 2015. Elasto-inertial pinched flow fractionation for continuous shape-based particle separation. *Analytical Chemistry*, **87**(22), pp.11523-11530.

[29] Tian, F., Zhang, W., Cai, L., Li, S., Hu, G., Cong, Y., Liu, C., Li, T. and Sun, J., 2017. Microfluidic co-flow of Newtonian and viscoelastic fluids for high-resolution separation of microparticles. *Lab on a Chip*, **17**(18), pp.3078-3085.

[30] Liu, C., Guo, J., Tian, F., Yang, N., Yan, F., Ding, Y., Wei, J., Hu, G., Nie, G. and Sun, J., 2017. Field-free isolation of exosomes from extracellular vesicles by microfluidic viscoelastic flows. *ACS nano*, **11**(7), pp.6968-6976.

[31] Tian, F., Cai, L., Chang, J., Li, S., Liu, C., Li, T. and Sun, J., 2018. Label-free isolation of rare tumor cells from untreated whole blood by interfacial viscoelastic microfluidics. *Lab on a Chip*, **18**(22), pp.3436-3445.

[32] Yang, S., Kim, J.Y., Lee, S.J., Lee, S.S. and Kim, J.M., 2011. Sheathless elasto-inertial particle focusing and continuous separation in a straight rectangular microchannel. *Lab on a Chip*, **11**(2), pp.266-273.

[33] Ahn, S.W., Lee, S.S., Lee, S.J. and Kim, J.M., 2015. Microfluidic particle separator utilizing sheathless elasto-inertial focusing. *Chemical Engineering Science*, **126**, pp.237-243.

[34] Liu, C., Xue, C., Chen, X., Shan, L., Tian, Y. and Hu, G., 2015. Size-based separation of particles and cells utilizing viscoelastic effects in straight microchannels. *Analytical Chemistry*, **87**(12), pp.6041-6048.

[35] Lu, X., Zhu, L., Hua, R.M. and Xuan, X., 2015. Continuous sheath-free separation of particles by shape in viscoelastic fluids. *Applied Physics Letters*, **107**(26), p.264102.

[36] Li, D., Lu, X. and Xuan, X., 2016. Viscoelastic separation of particles by size in straight rectangular microchannels: a parametric study for a refined understanding. *Analytical Chemistry*, **88**(24), pp.12303-12309.

[37] Li, D., Zielinski, J., Kozubowski, L. and Xuan, X., 2018. Continuous sheath-free separation of drug-treated human fungal pathogen Cryptococcus neoformans by morphology in biocompatible polymer solutions. *Electrophoresis*, **39**(18), pp.2362-2369.

[38] Lee, D.J., Brenner, H., Youn, J.R. and Song, Y.S., 2013. Multiplex particle focusing via hydrodynamic force in viscoelastic fluids. *Scientific Reports*, **3**, p.3258.

[39] Liu, C., Ding, B., Xue, C., Tian, Y., Hu, G. and Sun, J., 2016. Sheathless focusing and separation of diverse nanoparticles in viscoelastic solutions with minimized shear thinning. *Analytical Chemistry*, **88**(24), pp.12547-12553.

[40] Yuan, D., Zhang, J., Sluyter, R., Zhao, Q., Yan, S., Alici, G. and Li, W., 2016. Continuous plasma extraction under viscoelastic fluid in a straight channel with asymmetrical expansion–contraction cavity arrays. *Lab on a Chip*, **16**(20), pp.3919-3928.

[41] Yuan, D., Tan, S.H., Zhao, Q., Yan, S., Sluyter, R., Nguyen, N.T., Zhang, J. and Li, W., 2017. Sheathless Dean-flow-coupled elasto-inertial particle focusing and separation in viscoelastic fluid. *RSC Advances*, **7**(6), pp.3461-3469.

[42] Yang, S., Lee, S.S., Ahn, S.W., Kang, K., Shim, W., Lee, G., Hyun, K. and Kim, J.M., 2012. Deformability-selective particle entrainment and separation in a rectangular microchannel using medium viscoelasticity. *Soft Matter*, **8**(18), pp.5011-5019.

[43] Leal, L.G., 1980. Particle motions in a viscous fluid. *Annual Review of Fluid Mechanics*, **12**(1), pp.435-476.

[44] Nam, J., Namgung, B., Lim, C.T., Bae, J.E., Leo, H.L., Cho, K.S. and Kim, S., 2015. Microfluidic device for sheathless particle focusing and separation using a viscoelastic fluid. *Journal of Chromatography A*, **1406**, pp.244-250.

[45] Lim, H., Nam, J. and Shin, S., 2014. Lateral migration of particles suspended in viscoelastic fluids in a microchannel flow. *Microfluidics and Nanofluidics*, **17**(4), pp.683-692.

[46] Villone, M.M., D'avino, G., Hulsen, M.A., Greco, F. and Maffettone, P.L., 2013. Particle motion in square channel flow of a viscoelastic liquid: Migration vs. secondary flows. *Journal of Non-Newtonian Fluid Mechanics*, **195**, pp.1-8.

[47] Haward, S.J., Jaishankar, A., Oliveira, M.S.N., Alves, M.A. and McKinley, G.H., 2013. Extensional flow of hyaluronic acid solutions in an optimized microfluidic cross-slot device. *Biomicrofluidics*, **7**(4), p.044108.

[48] Nam, J., Tan, J.K.S., Khoo, B.L., Namgung, B., Leo, H.L., Lim, C.T. and Kim, S., 2015. Hybrid capillary-inserted microfluidic device for sheathless particle focusing and separation in viscoelastic flow. *Biomicrofluidics*, **9**(6), p.064117.

[49] Nam, J., Shin, Y., Tan, J.K.S., Lim, Y.B., Lim, C.T. and Kim, S., 2016. High-throughput malaria parasite separation using a viscoelastic fluid for ultrasensitive PCR detection. *Lab on a Chip*, **16**(11), pp.2086-2092.

[50] Del Giudice, F., Sathish, S., D'Avino, G. and Shen, A.Q., 2017. "From the edge to the center": viscoelastic migration of particles and cells in a strongly shear-thinning liquid flowing in a microchannel. *Analytical Chemistry*, **89**(24), pp.13146-13159.

[51] Nam, J., Jang, W.S. and Lim, C.S., 2019. Viscoelastic Separation and Concentration of Fungi from Blood for Highly Sensitive Molecular Diagnostics. *Scientific Reports*, **9**(1), p.3067.

[52] Kang, K., Lee, S.S., Hyun, K., Lee, S.J. and Kim, J.M., 2013. DNA-based highly tunable particle focuser. *Nature Communications*, **4**, p.2567.

[53] Li, D. and Xuan, X., 2018. Fluid rheological effects on particle migration in a straight rectangular microchannel. *Microfluidics and Nanofluidics*, **22**(4), p.49.

[54] Li, D. and Xuan, X., 2019. The motion of rigid particles in the Poiseuille flow of pseudoplastic fluids through straight rectangular microchannels. *Microfluidics and Nanofluidics*, **23**(4), p.54.

[55] Yasuda, K.Y., Armstrong, R.C. and Cohen, R.E., 1981. Shear flow properties of concentrated solutions of linear and star branched polystyrenes. *Rheologica Acta*, **20**(2), pp.163-178.

[56] Japper-Jaafar, A., Escudier, M.P. and Poole, R.J., 2010. Laminar, transitional and turbulent annular flow of drag-reducing polymer solutions. *Journal of Non-Newtonian Fluid Mechanics*, **165**(19-20), pp.1357-1372.

[57] Li, D., Lu, X., Song, Y., Wang, J., Li, D. and Xuan, X., 2016. Sheathless electrokinetic particle separation in a bifurcating microchannel. *Biomicrofluidics*, **10**(5), p.054104.

[58] Leal, L.G., 1979. The motion of small particles in non-Newtonian fluids. *Journal of Non-Newtonian Fluid Mechanics*, **5**, pp.33-78.

[59] D'Avino, G. and Maffettone, P.L., 2015. Particle dynamics in viscoelastic liquids. *Journal of Non-Newtonian Fluid Mechanics*, **215**, pp.80-104.

[60] Bird, R.B., Armstrong, R.C. and Hassager, O., 1987. Dynamics of polymeric liquids. Vol. 1: Fluid mechanics. John Wiley and Sons

[61] Leshansky, A.M., Bransky, A., Korin, N. and Dinnar, U., 2007. Tunable nonlinear viscoelastic “focusing” in a microfluidic device. *Physical Review Letters*, **98**(23), p.234501.

[62] Barnes, H.A., Hutton, J.F. and Walters, K., 1989. An introduction to rheology. Elsevier.

[63] Escudier, M.P. and Smith, S., 1999. Turbulent flow of Newtonian and shear-thinning liquids through a sudden axisymmetric expansion. *Experiments in Fluids*, **27**(5), pp.427-434.

[64] Won, D. and Kim, C., 2004. Alignment and aggregation of spherical particles in viscoelastic fluid under shear flow. *Journal of Non-Newtonian Fluid Mechanics* , **117**(2-3), pp.141-146.

[65] Ho, B.P. and Leal, L.G., 1974. Inertial migration of rigid spheres in two-dimensional unidirectional flows. *Journal of Fluid Mechanics*, **65**(2), pp.365-400.

[66] Asmolov, E.S., 1999. The inertial lift on a spherical particle in a plane Poiseuille flow at large channel Reynolds number. *Journal of Fluid Mechanics*, **381**, pp.63-87.

[67] Liu, C., Hu, G., Jiang, X. and Sun, J., 2015. Inertial focusing of spherical particles in rectangular microchannels over a wide range of Reynolds numbers. *Lab on a Chip*, **15**(4), pp.1168-1177.

[68] Huang, P.Y., Feng, J., Hu, H.H. and Joseph, D.D., 1997. Direct simulation of the motion of solid particles in Couette and Poiseuille flows of viscoelastic fluids. *Journal of Fluid Mechanics*, **343**, pp.73-94.

[69] Huang, P.Y. and Joseph, D.D., 2000. Effects of shear thinning on migration of neutrally buoyant particles in pressure driven flow of Newtonian and viscoelastic fluids. *Journal of Non-Newtonian Fluid Mechanics*, **90**(2-3), pp.159-185.

[70] Li, G., McKinley, G.H. and Ardekani, A.M., 2015. Dynamics of particle migration in channel flow of viscoelastic fluids. *Journal of Fluid Mechanics*, **785**, pp.486-505.

CHAPTER SEVEN

CONCLUSIONS AND FUTURE WORK

7.1 Conclusions

This dissertation has extensively studied the non-Newtonian fluid rheology effect on particle migration and proposed two types of fluid to implement sheath-free particle separation in a straight rectangular channel. First of all, we conducted a series of experiments to study the particle lateral motion in specially chosen five fluids and revealed that the fluid elasticity will direct particle to the center of the rectangular channel while sole shear thinning will direct particle to both center and four corners of the channel. Once those two rheological properties combined with inertia, the final particle equilibrium position is determined by the relative significance of the three rheological effects. Then we choose two non-Newtonian fluids, PEO and XG, from the rheology studies as both of them can focus particle to dual off-center streams under certain experimental conditions. Next, we successfully implemented a continuously sheathless separation of both size-based polystyrene particle and morphology-based yeast cells in a simple straight channel using PEO solution. Since the dual particle/cell trains in both cases will appear at Re smaller than 1 where the fluid inertia is still weak, we proposed that the elastic force should be decomposed into two components: center-directed and wall-directed elastic force. The rest part of the dissertation focuses on the inelastic pseudoplastic fluid, XG solution. We implemented a systematic study on the particle behavior in XG solution through a straight rectangular channel and found that the particle equilibrium position is a strong function of flow rate, channel depth, solvent concentration and particle size. Finally, we realized a size-based binary and ternary particle separation in an AR = 2 straight channel using XG solution. The range of flow rate, which can render high separation purity and efficiency, proves to be much wider than pervious microfluidic separator using elasto-inertial force. The detailed conclusion and major contribution for each chapter list below.

In chapter 2, we have conducted a systematic experimental study of the 10 μm polystyrene particle motion in the flow of five different fluids with varying rheological properties through a straight rectangular microchannel with AR = 1.22. In a Newtonian fluid, the particles will migrate to four equilibrium positions that locate near the center of each sidewalls due to the flow induced inertial effect. In contrast, particle will migrate towards the channel centerline in an elastic Boger fluid due to the fluid elasticity effect alone, and towards both the centerline and corners in a pseudoplastic fluid due to the fluid shear thinning effect alone. With the help of these individual fluid rheological effects, we tried to understand the particle motion in fluid with compound rheology. We find that particles migrate to two off-center equilibrium positions in the central plane parallel to the longer side of the channel under the combined shear thinning and inertia. Further adding the elasticity effect will also alter the particle equilibrium position, which depends strongly on the relative significance of the three rheological effects.

In chapter 3, we have achieved continuous-flow sheath-free separations of binary 5 μm/10 μm and ternary 3 μm/5 μm/10 μm particle mixture in 1000 ppm PEO solution through a simple straight rectangular microchannel. A comprehensive experimental study of the effects of flow rate, solvent viscosity, polymer concentration, polymer type, and channel aspect ratio on the binary particle separation is also conducted in terms of four dimensionless numbers. To explain the observed shifting of particle focusing position under negligible inertia, we have proposed to break down the elastic lift into a center-directed component due to fluid elasticity effect and a wall-directed component due to the fluid elasticity and shear-thinning effects.

In chapter 4, we use the separation strategy presented in the last chapter to demonstrate a continuously sheathless separation of drug-treated *C. neoformans* by morphology in the biocompatible PBS-based PEO solution. The heterogeneous mixture of yeast cells with varying shapes and sizes are elasto-inertially focused towards morphology-dependent equilibrium positions within the straight rectangular channel. The larger, abnormal-shaped multimeric cells are found to stay further away from the channel center than the smaller, normal-shaped cells. We have studied the effect of flow rate, PEO concentration, and channel height on the morphology-based yeast cell separation. Three dimensionless metrics including efficiency, purity and enrichment ratio are used to evaluate the separation performance. The best separation performance is achieved in 1000 ppm PEO solution flow through an AR = 2 microchannel at flow rate of the order of 100 μL/h. This throughput fills the gap between those of sheath-free dielectrophoretic and inertial separations of particles and cells by shape.

In chapter 5, we have conducted a systematic experimental study of the parametric effect on rigid particle motion in XG solution flowing through the straight rectangular microchannels. We find that if the inertia is weak, particles will travel out of the channel near both the corners and centerline in all cases because of the sole action of elastic lift. With the increase of flow rate, nearly all particles near the corners will deprive from the channel wall because of the enhanced wall-induced inertial lift. The only exception is the largest 20 μm particles that stay close to the corners in the entire range of tested flow rate because of the strong elastic lift and the large particle confinement ratio. Meanwhile, those particles located at centerline will migrate outward because of the enhanced shear gradient-induced inertial lift unless the microchannel is too deep, or the particle is too small, or the XG concentration is too high. These observed particle behaviors imply a potentially high throughout size-based separation of rigid particle in XG solution using simple straight rectangular channel.

In chapter 6, we have demonstrated for the first time that rigid spherical particles can be continuously separated by size in the flow of inelastic XG solutions through straight rectangular microchannels. This sheath- and label-free particle separation is achieved by the differential elastic focusing in XG solution. We found that large particles align near the channel walls while smaller ones travel in the bulk of the microchannel. A comprehensive parametric study of the flow rate, XG concentration, and channel depth effect on the particle separation performance is also conducted. Following the proposed elastic lift analysis in Chapter 3, we qualitatively explain the observed shifting of particle focusing position by the weak center-directed elastic lift due to the small elasticity and the strong wall-directed elastic lift due to the prominent shear thinning of XG solution.

7.2 Future work

For the experimental part, we hope to extend the present separation strategy to submicron particle in the future study as certain cells (e.g., platelet) are around this scale.

We will also investigate the particle motion in non-Newtonian fluid through channel with other geometry, such as straight channel with cavity, which can induce extra drag to manipulate particles. Moreover, as introducing in Chapter 1, very few types of non-Newtonian fluid are used in microfluidic devices. We will explore the capability of other rarely used polymer and bio-fluids on the particle manipulation in microchannel. For the numerical part, intensive studies are required to understand the experimental observations. We will utilize multiple standard viscoelastic models (Oldroyd-B, Giesekus, and Phan-Thien-Tanner), which can simulate fluids with different rheology, to analyze the elastic and inertial lift acting on the particle and to verify its equilibrium position distribution within the straight rectangular channel.

APPENDICES

Appendix A

SUPPORTING INFORMATION FOR VISCOELASTIC PARTICLE SEPARATION BY SIZE IN STRAIGHT RECTANGULAR MICROCHANNELS: A PARAMETRIC STUDY FOR A REFINED UNDERSTANDING

1. Determination of the rheology properties of polymer solutions in Table 3.1 of the main text

The zero-shear dynamic viscosities, η_0, of 500 ppm and 1000 ppm PEO solutions were obtained directly from the paper of Rodd et al.[1] while that of 2000 ppm was calculated via the viscosity blending equation.[2] The intrinsic viscosity, $[\eta]$, of PEO solutions was calculated from the Mark-Houwink-Sakurada equation,[3] $[\eta] = 0.072M_w^{0.65} = 897$ ml/g. Then, the overlap concentration, $c^* = 0.77/[\eta] = 858$ ppm, was determined from Graessley's modified equation.[4] Therefore, the prepared PEO solutions are either in the dilute (under 500 ppm) or semi-dilute (beyond 500 ppm) regime, which exhibit weak to mild shear-thinning effects.[5-7] As suggested by Tirtaatmadja et al.,[3] The effective relaxation time, λ_e, of PEO solutions was estimated from the following empirical formula,

$$\lambda_e = 18\lambda_{Zimm}(c/c^*)^{0.65} \tag{A-1}$$

where λ_{Zimm} is the relaxation time predicted according to Zimm theory,[8]

$$\lambda_{Zimm} = F\frac{[\eta]M_w\eta_s}{N_A k_B T} \tag{A-2}$$

In the above $F = 0.463$ is the pre-factor estimated from the Remann Zeta function using a solvent quality exponent 0.55,[1] η_s = 1.0 mPa·s is the solvent (i.e., water) viscosity,

N_A is the Avogadro's constant, k_B is the Boltzmann's constant, and T is the absolute temperature, which gives $\lambda_{Zimm} = 0.34$ s.

The zero-shear viscosities, η_0, of the two PEO/glycerol solutions were obtained from Rodd et al.[9] We acknowledge that the real values for our solutions may be higher than those reported because of the higher PEO concentration (1000 ppm vs. 750 ppm) in our solutions. The intrinsic viscosities, $[\eta]$, and the Zimm relaxation times, λ_{Zimm}, of the two PEO/glycerol solutions were also obtained from Rodd et al.,[9] with which the overlap concentrations were first calculated to be $c^* = 0.77/[\eta] = 833$ and 1009 ppm, respectively. Then, the effective relaxation times were calculated from eq S-1. The rheology properties of 8 wt. % PVP solution were obtained from Yang et al.,[5] and those of 50 ppm PAA were from Campo-Deaño et al.[10] and Galindo-Rosales et al.[11]

2. Binary particle separation in different PEO solutions

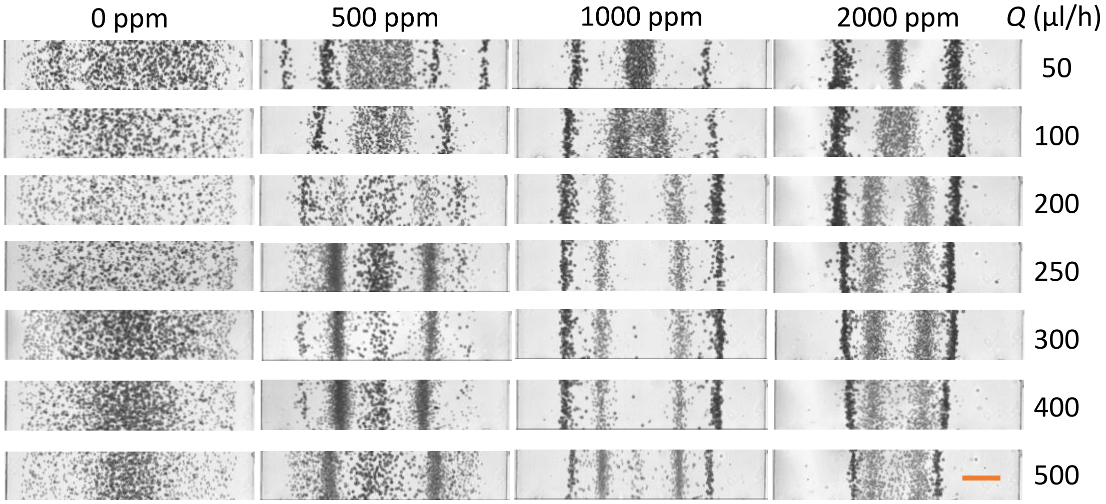

Fig. A-1: Elasto-inertial separation of 5 μm and 10 μm particles in PEO solutions of various concentrations through a straight 50 μm-wide and 25 μm-high rectangular microchannel at various flow rates. The scale bar represents 100 μm.

3. Binary particle separation in different 1000 ppm PEO/glycerol solutions

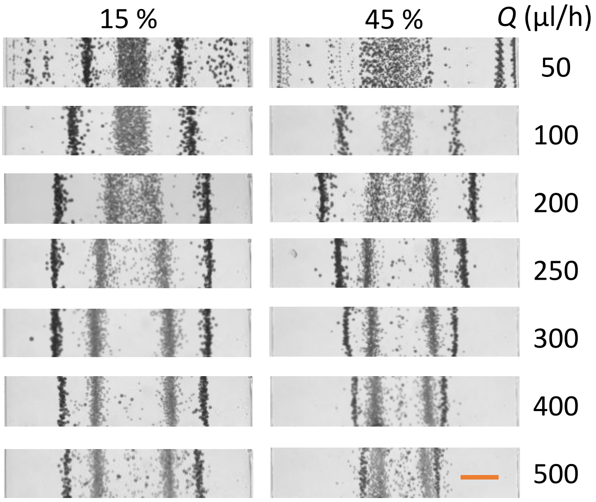

Fig. A-2: Elasto-inertial separation of 5 μm and 10 μm particles in 1000 ppm PEO/glycerol (wt. %) solutions through a straight 50 μm-wide and 25 μm-high rectangular microchannel at various flow rates. The scale bar represents 100 μm.

4. Binary particle separation in different polymer solutions

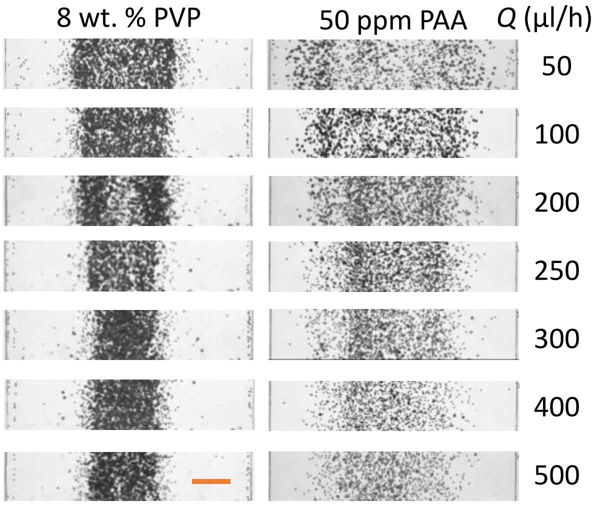

Fig. A-3: Elasto-inertial separation of 5 μm and 10 μm particles in different polymer solutions through a straight 50 μm-wide and 25 μm-high rectangular microchannel at various flow rates. The scale bar represents 100 μm.

5. Binary particle separation in channels of different aspect ratios

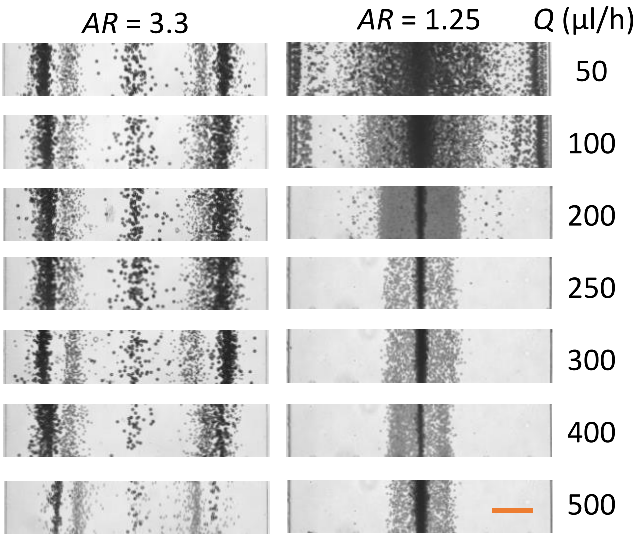

Fig. A-4: Elasto-inertial separation of 5 µm and 10 µm particles in 1000 ppm PEO solution through straight 50 µm-wide rectangular microchannels with different depths at various flow rates: (left) 15 µm deep with *AR* = 3.3 and (right) 40 µm deep with *AR* = 1.25. The scale bar represents 100 µm.

6. Ternary particle separation

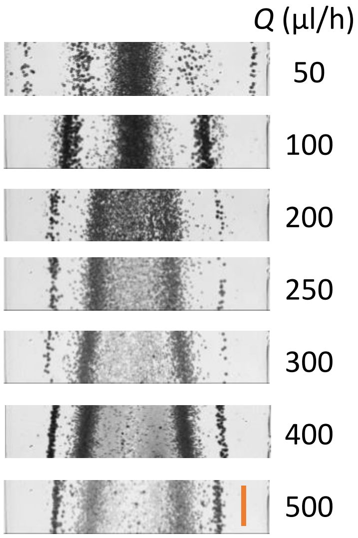

Fig. A-5: Elasto-inertial separation of 3 µm, 5 µm and 10 µm particles in 1000 ppm PEO solution through a straight 50 µm-wide and 25 µm-high rectangular microchannels at various flow rates. The scale bar represents 100 µm.

References

[1] Rodd, L.E., Scott, T.P., Boger, D.V., Cooper-White, J.J. and McKinley, G.H., 2005. The inertio-elastic planar entry flow of low-viscosity elastic fluids in micro-fabricated geometries. *Journal of Non-Newtonian Fluid Mechanics*, **129**(1), pp.1-22.

[2] Maples, R.E., 1993. Petroleum Refinery Process Economy, Pennwell.

[3] Tirtaatmadja, V., McKinley, G.H. and Cooper-White, J.J., 2006. Drop formation and breakup of low viscosity elastic fluids: Effects of molecular weight and concentration. *Physics of Fluids*, **18**(4), p.043101.

[4] Graessley, W.W., 1980. Polymer chain dimensions and the dependence of viscoelastic properties on concentration, molecular weight and solvent power. *Polymer*, **21**(3), pp.258-262.

[5] Yang, S., Kim, J.Y., Lee, S.J., Lee, S.S. and Kim, J.M., 2011. Sheathless elasto-inertial particle focusing and continuous separation in a straight rectangular microchannel. *Lab on a Chip*, **11**(2), pp.266-273.

[6] Nam, J., Lim, H., Kim, D., Jung, H. and Shin, S., 2012. Continuous separation of microparticles in a microfluidic channel via the elasto-inertial effect of non-Newtonian fluid. *Lab on a Chip*, **12**(7), pp.1347-1354.

[7] Rodd, L.E., Lee, D., Ahn, K.H. and Cooper-White, J.J., 2010. The importance of downstream events in microfluidic viscoelastic entry flows: Consequences of increasing the constriction length. *Journal of Non-Newtonian Fluid Mechanics*, **165**(19-20), pp.1189-1203.

[8] Rubinstein, M. and Colby, R.H., 2003. *Polymer physics* (Vol. 23). Oxford university press.

[9] Rodd, L.E., Cooper-White, J.J., Boger, D.V. and McKinley, G.H., 2007. Role of the elasticity number in the entry flow of dilute polymer solutions in micro-fabricated contraction geometries. *Journal of Non-Newtonian Fluid Mechanics*, **143**(2-3), pp.170-191.

[10] Campo-Deaño, L., Galindo-Rosales, F.J., Pinho, F.T., Alves, M.A. and Oliveira, M.S., 2011. Flow of low viscosity Boger fluids through a microfluidic hyperbolic contraction. *Journal of Non-Newtonian Fluid Mechanics*, **166**(21-22), pp.1286-1296.

[11] Galindo-Rosales, F.J., Campo-Deaño, L., Pinho, F.T., Van Bokhorst, E., Hamersma, P.J., Oliveira, M.S. and Alves, M.A., 2012. Microfluidic systems for the analysis of

viscoelastic fluid flow phenomena in porous media. *Microfluidics and Nanofluidics*, **12**(1-4), pp.485-498.

Appendix B

SUPPORTING INFROMATION FOR PARTICLE SEPARATION IN INELSTIC NON-NEWTONIAN FLUIDS

1. Binary particle separation in Newtonian solution

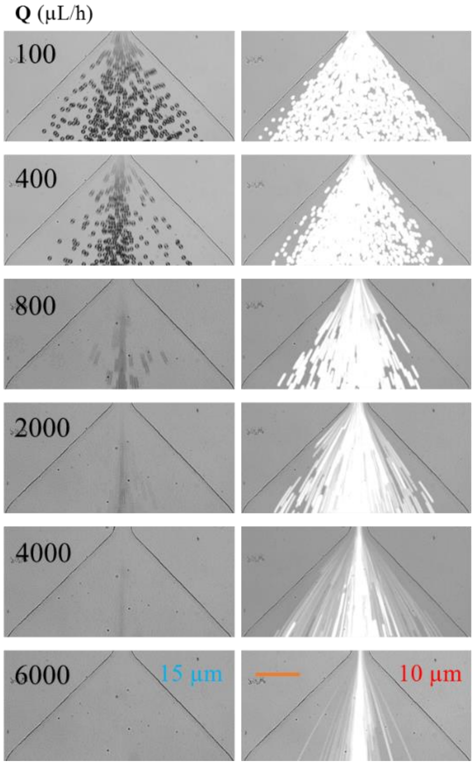

Fig. B-1. Particle behavior of 10 µm and 15 µm particles in Newtonian fluid through a straight 65 µm-wide and 30 µm-high rectangular microchannel at various flow rates. The scale bar represents 100 µm.

2. Binary particle separation in 2000 ppm XG

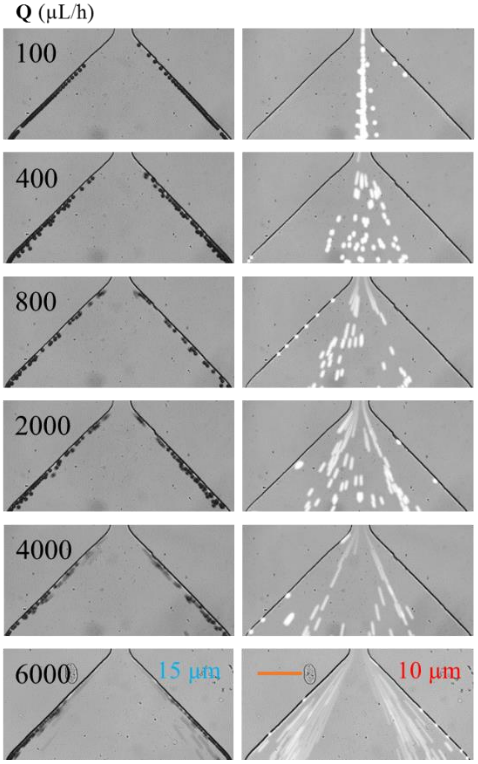

Fig. B-2. Particle separation of 10 μm and 15 μm particles in 2000 ppm XG through a straight 65 μm-wide and 30 μm-high rectangular microchannel at various flow rates. The scale bar represents 100 μm.

3. Binary particle separation in 1000 ppm XG

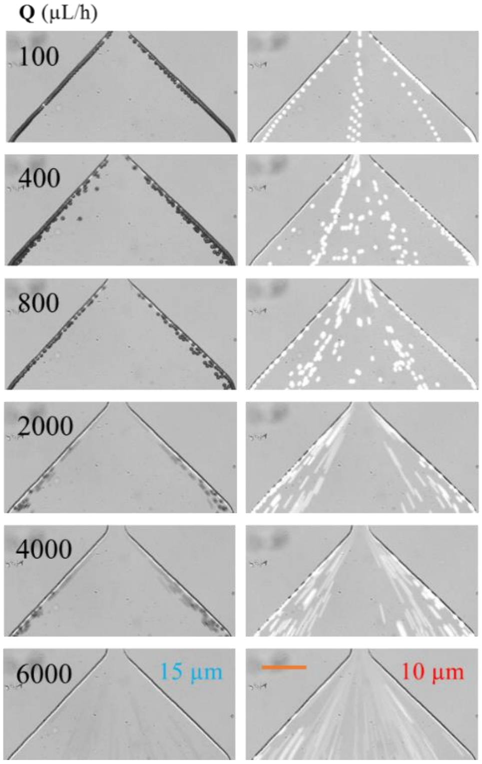

Fig. B-3. Particle separation of 10 µm and 15 µm particles in 1000 ppm XG through a straight 65 µm-wide and 30 µm-high rectangular microchannel at various flow rates. The scale bar represents 100 µm.

4. Binary particle separation in 3000 ppm XG

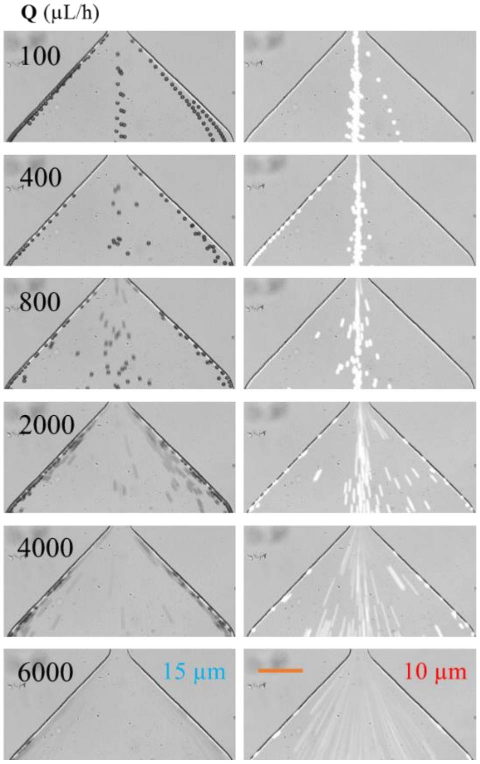

Fig. B-4. Particle separation of 10 μm and 15 μm particles in 3000 ppm XG through a straight 65 μm-wide and 30 μm-high rectangular microchannel at various flow rates. The scale bar represents 100 μm.

5. Binary particle separation in 20 µm-high microchannel

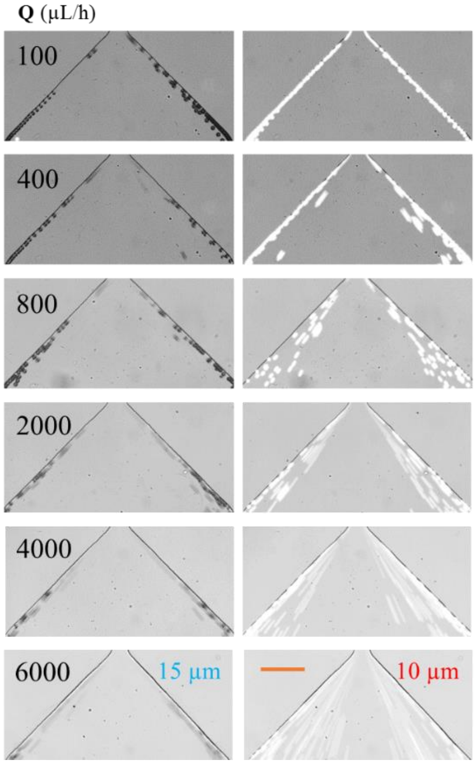

Fig. B-5. Particle separation of 10 µm and 15 µm particles in 2000 ppm XG through a straight 65 µm-wide and 20 µm-high rectangular microchannel at various flow rates. The scale bar represents 100 µm.

6. Binary particle separation in 54 µm-high microchannel

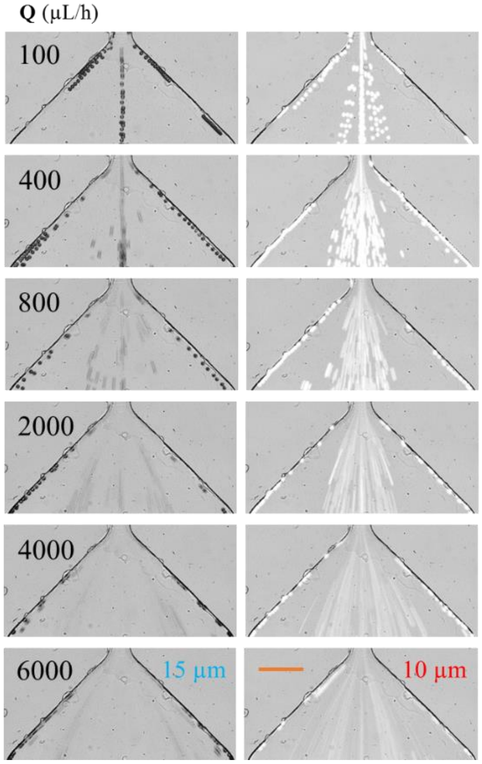

Fig. B-6. Particle separation of 10 µm and 15 µm particles in 2000 ppm XG through a straight 65 µm-wide and 54 µm-high rectangular microchannel at various flow rates. The scale bar represents 100 µm.

7. Ternary particle separation in 2000 ppm XG

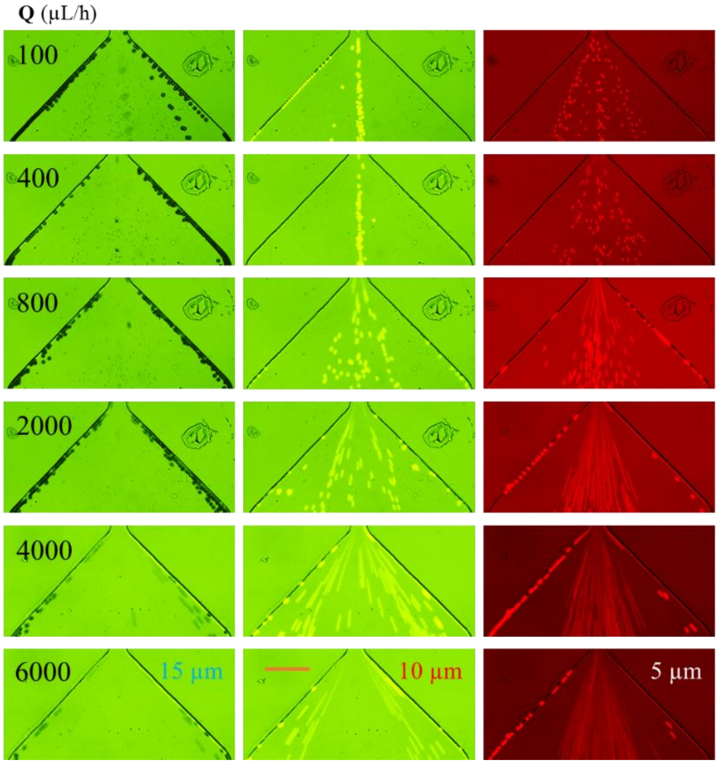

Fig. B-7. Particle separation of 5 μm, 10 μm, and 15 μm particles in 2000 ppm XG through a straight 65 μm-wide and 30 μm-high rectangular microchannel at various flow rates. The scale bar represents 100 μm.